



**UNIVERSITÀ DEGLI STUDI DI TRIESTE**

---

XXIII CICLO DEL DOTTORATO DI RICERCA IN  
SCIENZE E TECNOLOGIE CHIMICHE E FARMACEUTICHE

**THE ROLE OF INVERSE NONIONIC MICROEMULSION  
IN THE SYNTHESIS OF SiO<sub>2</sub> NANOPARTICLES**

Settore scientifico-disciplinare: CHIMICA FISICA (CHIM 02)

Dottoranda

**NINA SAVKO**

Responsabile Dottorato di Ricerca

Prof. **ENZO ALESSIO**

---

Relatore

Dott. **FIORETTA ASARO**

**Anno Accademico 2009/2010**

# INDEX

<b>1 Introduction</b>	<b>1</b>
1.1 Nanotechnology	1
1.1.1 SiO <sub>2</sub> Nanoparticles	3
1.2 The Sol-Gel Process	5
1.2.1 Introduction	5
1.2.2 Formation Steps	7
1.2.3 Stöber Synthesis	13
1.2.4 Fluoride as Catalyst	14
1.3 Microemulsions	15
1.3.1 Surfactants	15
1.3.2 Types of Microemulsion	19
1.3.3 Inverse Microemulsions as Reaction Media for the Synthesis of SiO <sub>2</sub> Nanoparticles	21
1.4 Pulsed-field Gradient Stimulated Echo NMR	28
1.4.1 Introduction	28
1.4.2 Pulsed Field Gradient NMR	29
1.4.3 Eddy Currents	32
1.4.4 Temperature Gradients and Convection Compensation	34
1.4.5 Diffusion Ordered Spectroscopy (DOSY)	34
1.5 Aims	36
<b>2 Experimental</b>	<b>38</b>
2.1 Materials	38
2.2 Preparation of Samples	38
2.2.1 Microemulsions	38
2.2.2 Reaction Media	39
2.2.3 Classical HCl-Catalyzed Sol-Gel	40
2.2.4 Isolation of Nanoparticles	40

2.3 NMR Measurements	41
2.3.1 $^1\text{H}$ , $^{13}\text{C}$ and $^{29}\text{Si}$ NMR Measurements	41
2.3.2 PGSTE Measurements	41
2.4 FT-IR Measurements	42
2.5 UV-Vis Measurements	43
2.6 Photoluminescence and Raman Measurements	43
<b>3 Results and Discussion</b>	<b>44</b>
3.1 Basic Medium	44
3.1.1 NMR Characterization of Microemulsions	44
3.1.2 NMR Characterization of Reaction Medium	52
3.1.3 Hydrolysis	59
3.1.4 Characterization of the Product	62
3.2 Acidic Medium	65
3.2.1 NMR Characterization of Microemulsions	66
3.2.2 NMR Characterization of Reaction Media	77
3.2.3 Hydrolysis	81
3.2.4 Condensation	85
3.2.4 Characterization of the Products	89
3.3 Comparison of Base and Acid-Catalyzed Syntheses	95
3.4 $\text{Cu}^{2+}$ and $\text{Co}^{2+}$ Doped $\text{SiO}_2$ Nanoparticles	97
3.4.1 NMR Characterization of Microemulsions	98
3.4.2 NMR Characterization of Reaction Media	100
3.4.3 Hydrolysis	101
3.4.4 UV-Vis Spectra	103
3.4.5 Characterization of the Products	107
<b>4 Conclusions</b>	<b>114</b>
<b>5 Bibliography</b>	<b>116</b>

# 1 INTRODUCTION

## 1.1 Nanotechnology

The manipulation of matter on the atomic or molecular scale is an old vision of scientist Richard Feynman who in his talk “There’s plenty of room at the bottom” at the annual meeting of the American Physical Society at Caltech on December 29, 1959 first used the concepts nowadays used in nanoscience and in a way marked the beginning of the era of the research on a small scale [1]. The basic idea was to change the relative magnitude of physical phenomena such as gravity, surface tension, van der Waals forces, etc. decreasing the importance of the former and increasing the importance of the latter two.

The discovery of the molecular beam epitaxy by Alfred Cho and John Arthur at Bell Labs in 1968 enabled the controlled deposition of single atomic layer and the invention of the scanning tunneling microscope in 1981 by Gerd Karl Binnig and Heinrich Rohrer at IBM's laboratories enabled scientists to image the position of individual atoms on surfaces. These were key technological milestones for the advance of nanoscience and nanotechnology into a robust and well-accepted scientific field. The old vision has become true and new opportunities have been recognized in all branches of technology from optical systems, electronics, automotive industries, to environmental engineering and medicine where intelligent materials, faster electronics, biosensors, nanomotors are just a few examples of the achievements. Although nanotechnology is still in its infancy, these first practical applications clearly demonstrate its enormous potential.

The term “nano” derives from the Greek word for “dwarf”, “nanos”. This etymology makes it clear that tiny dimensions are involved. On the metric scale  $1 \text{ nm} = 10^{-9} \text{ m}$  and it is obvious that we deal with dimensions not visible to the naked eye, beyond the normal limits of our observation. For comparison, it is the length of about ten hydrogen atoms.

There are two main approaches for nanofabrication, the “bottom-up” and “top-down”. In the former materials and devices are built from molecular

components which self-assemble chemically by principles of molecular recognition to form larger structures. In the latter approach structures with long-range order are constructed without control at atomic level. The integration of the two techniques is expected to eventually provide the best combination for the nanoparticle synthesis.

Nanoparticles, besides their small size, have other characteristics which dominate their physicochemical properties and single them out from bulk materials. These are classified in two important groups [2]:

(i) Surface-dependent particle properties are those that become dominant owing to the high surface-to-volume ratio. This means that a given quantity of nanoparticles because of the vast surface will be much more reactive than the same quantity of larger particles.

(ii) Size-dependent quantum effects are phenomena deriving when the electronic structure of nanoparticles is influenced directly by their size. These are due to the transition from an atom or molecule with defined energy levels to the dispersed bands of collective ensembles of atoms and finally of the bulk material. In general, the phenomena occur for the particles with diameter minor of 20 nm.

The methods for nanoparticles synthesis can be divided into three groups [3]:

(1) grinding methods (wet and dry grinding, reactive grinding, etc.)

(2) gas-phase methods (chemical vapor deposition (CVD), laser ablation deposition (LAD), sputtering techniques, etc.)

(3) liquid-phase syntheses (forced hydrolysis, hydrothermal synthesis, sol-gel process, microemulsion method, etc.)

When grinding route is employed contamination by material abraded from the grinding body must be expected. Particles with diameter greater than 50 nm are hardly obtainable and the agglomeration is appreciable. On the other hand the route is extremely important for technical processes as large quantities of substance are obtainable at low cost. Gas-phase methods yield crystalline nanoparticles with mostly non-covered surfaces but the formation of aggregates difficult to separate into primary particles occurs due to the high synthesis temperatures. In liquid-phase syntheses particle size and agglomeration can be prevented effectively by steric or electrostatic stabilization of the surface immediately after nucleation. As steric stabilizers bulky organic molecules such as

surfactants or polymers are typically used as they provide a protective shield coordinating particles strongly enough to prevent agglomeration and controlling their shape but are also easily removed from the surface. Electrostatic stabilization is achieved by adsorption of ions on the particle surface inducing a surface charge and hence repulsion from other particles [4]. These are standard methods in colloid chemistry and many of its concepts provided scientific basis for the study of nanoparticles.

Nanoparticles now find a variety of industrial applications, for modifying and upgrading a wide range of substrates and materials; in heterogeneous catalysis, ranging from classical synthesis chemistry to photocatalysis; the use of luminescent, plasmonic, and magnetic nanoparticles in molecular biology and medical diagnosis and therapy; in electronics, ranging from flexible electronic circuit elements, light-emitting diodes, visual display units to dye-sensitized solar cells and magnetic data-storage media.

This high degree of interdisciplinarity is a characteristic feature of nanotechnology and contributes to the fascination of the field but in many cases, the complexity of the synthesis and the cost of the materials still present obstacles to the use of nanoparticles.

### 1.1.1 SiO<sub>2</sub> Nanoparticles

Silica nanoparticles are stable, biologically inert, biocompatible and the Si-OH moieties on the surface make them functionalizable using simple silane chemistry. Therefore they find a palette of innovative applications, e.g. as diagnostic means, whether loaded with suited fluorophores [5-7], or in drug [8,9] and even gene [9,10] delivery, in high-tech industries, for computers and optoelectronic devices [11-14], in forensic investigations for fingerprint detection [15], etc. The silica nanoparticles are predominantly synthesized in basic medium but a significant number of drug molecules which may be delivered by means of encapsulation in silica nanoparticles have proved to be stable only under acidic conditions. Also, the particles containing lanthanides, known for their fluorescence

in silica films, and therefore applicable as agents in cell imaging, can be synthesized only under acidic conditions as in basic medium precipitate as oxides.

When in 1942 Harry Kloefer invented the process of hydrolysis at high temperature to produce the silicic acid, he had no idea that this was the first chapter of an extraordinary successful story that continues today. The pyrogenic silica was first commercialized in 1943 with the name AEROSIL<sup>®</sup> by company Degussa after obtaining the patent and by now it is produced in great number of variants and sold in countries all over the world. Since then the product has been continuously optimized so today AEROSIL<sup>®</sup> is a silica powder produced in the form of aggregated particles with diameter between 60-80 nm.

Nowadays there are different approaches for the fabrication of silica nanomaterials including the sol-gel method [16], biomimicking growth [17], ultrasonic synthesis [18], thermal oxidation [19], and chemical vapor deposition [20]. The morphology of the nanostructure is often governed by the method of preparation.

Sol-gel chemistry has revolutionized ceramic production by enabling ambient temperature, solution-based synthesis of metal oxides with porosity which can be tailored. The reaction starting from a silicon alkoxide involves two different processes:

- (i) the alkoxide hydrolysis, and
- (ii) the polymerization, that is polycondensation of the hydrolysis products.

The polymer obtained via base catalysis, with respect to that produced from acid catalysis, is characterized by a much higher degree of crosslinking, as revealed by light scattering [21] and solid-state <sup>29</sup>SiNMR [22]. In referring to an acidic environment in the synthesis of silica, an environment with a pH lower than the isoelectric point of silica (pH= 2) is intended [23]. In the acid-catalyzed synthesis, protonated species are involved in both steps, and the rate-determining step is the latter. In contrast, the rate-determining step is the former in the base-catalyzed synthesis. Another striking difference, demonstrated by the extensive research carried out for homogeneous solutions, is that in an acidic medium the polymeric silica grows through the coupling of clusters, whereas in the presence of strong bases, the polymer grows through the addition of monomers, derived from the products of alkoxide hydrolysis and the concurrent depolymerization reaction [23].

The sol–gel chemistry increases the range of applications of SiO<sub>2</sub> nanoparticles by permitting to dope them with a large number of organic and inorganic molecules. The metal doped silica systems are important for optical applications [24] and if the metal ions are finely dispersed on SiO<sub>2</sub> surface very efficient catalysators can be obtained [25]. The rare earth or transition metal ions doped nanoparticles are perspective as the new generation of light sources [26].

## 1.2 The Sol-Gel Process

### 1.2.1 Introduction

Sol-gel processing refers to the hydrolysis and condensation of alkoxide-based precursors such as Si(OMe)<sub>4</sub> (tetramethyl orthosilicate, or TMOS) or Si(OEt)<sub>4</sub> (tetraethyl orthosilicate, or TEOS).

The earliest examples of silica gels, apart from those that exist in nature, date to the work of Ebelmen in 1846 [27] but sol-gel processing did not earn wide attention until Geffcken and Berger devised a method of preparing oxide films from sol-gel precursors in the late 1930's, which proved useful in the manufacturing of stained glass [28].

The lack of popularity of traditional routes may be explained by use of high processing temperatures, incompatible with the encapsulation of organic molecules, as well as by the relative difficulty in manipulating the internal microstructure of ceramics with respect to polymers. Both of these limitations can be overcome with sol-gel technology, which can be described as an inorganic, ambient temperature, polymerization technique where the product has higher purity and homogeneity compared with traditional glass melting or ceramic powder methods. The goal of sol-gel processing is to control the surfaces and interfaces of materials during the earliest stages of production.



*Sol* is, by definition, a type of colloid in which solid particles are suspended in a continuous liquid phase. *Colloid* is a homogeneous mixture in which the dispersed particles with diameters of 1-100 nm do not settle out. *Gel* is an interconnected solid network of polymeric chains in a liquid matrix with pores of submicrometer dimensions. The system is in thermodynamic equilibrium and the liquid does not flow out spontaneously. Moreover, the nature of the liquid and its quantity are responsible for the denomination of the gel. If the liquid is mostly composed of water, and the aqueous phase is in the greatest proportion, the gel is called *hydrogel*. If the liquid is an alcohol, the gel is *alcogel*. If most of the liquid is removed as a gas phase under hypercritical conditions the gel obtained is *aerogel*, but if it is removed near ambient pressure by thermal evaporation the gel is called *xerogel* [3].

Reversible transformations of a gel that occur inside the liquid matrix are swelling and shrinkage while other properties are irreversible and involve aging, drying and syneresis.

The gels can be classified in four categories, as proposed by Flory [29]:

- (1) lamellar structures;
- (2) covalent polymeric networks;
- (3) polymer networks formed by local crystallization;
- (4) porous network of macroscopic particles of various shapes.

The ceramists do not prefer this classification as some gels can enter few classes and the nature of bonding and of the units forming the network is not always well defined. They prefer to classify them simply in two categories:

- (1) polymeric gels, and
- (2) colloidal gels.

## 1.2.2 Formation Steps

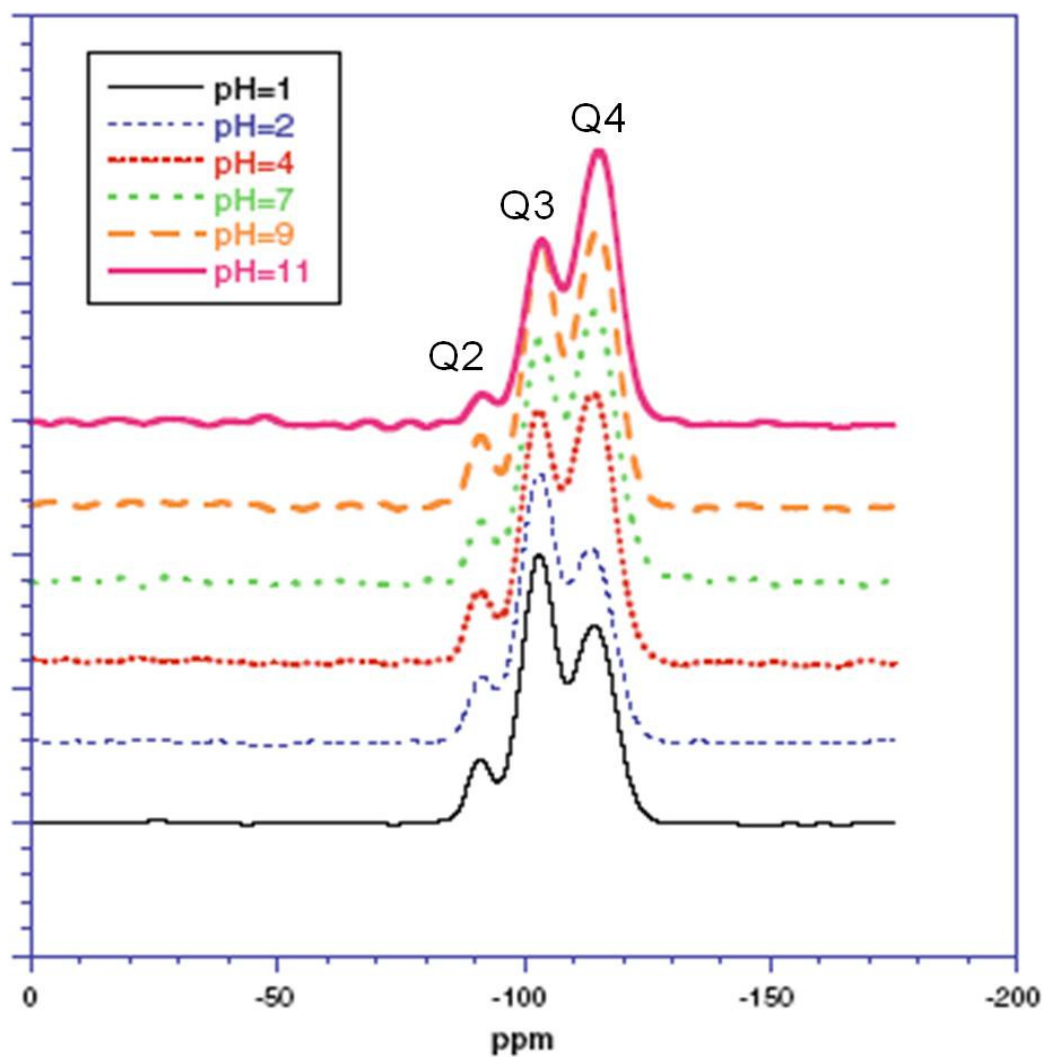
The starting point for the formation of a gel is the hydrolysis of alkoxide precursor, followed by condensation (polymerization) and formation of a sol. This colloidal solution is then aged and the evaporation of the solvent and water may occur slowly, leading to a bulk gel, or rapidly, by deposition methods, such as spin or dip-coating. The product obtained may be further dried or sintered (densified) with simultaneous elimination of porosity and residual OH groups.

Sol-gel chemistry can be catalyzed by either acids or bases and the final product is highly influenced by the pH of the reaction medium. The products obtained at certain pH are following:

- pH < 2                      microporous gel
- pH = 2-7                    mesoporous gel
- pH >> 7                    gel with monodisperse silica particles

<sup>29</sup>Si NMR spectra in the solid state, reported in Figure 1.1 [22], revealed the difference in reaction intermediates at different pH. The ratio Q4/Q3 is much higher for the products synthesized at pH = 11 from those at pH = 1, where Q4 indicates Si atom bearing 4 Si-O bonds, Q3 Si atom bearing 3 and Q2 Si atom bearing only 2 Si-O bonds.

A boundary between acidic and basic medium appears at pH = 2 since the point of zero charge (PZC), where the surface charge is zero, and the isoelectric point (IEP), where the electrical mobility of the silica particles is zero, are both in the range of pH 1-3. Near IEP where there is no electrostatic particle repulsion, the growth and aggregation process occur together and may be indistinguishable. At pH > 7 all the condensed species are more likely to be ionized and therefore mutually repulsive so the growth occurs primarily by the addition of monomers to more highly condensed particles rather than by aggregation.



**Figure 1.1**  $^{29}\text{Si}$  MAS-NMR of gels synthesized at different pH; Qn indicates the number of Si-O bonds [22].

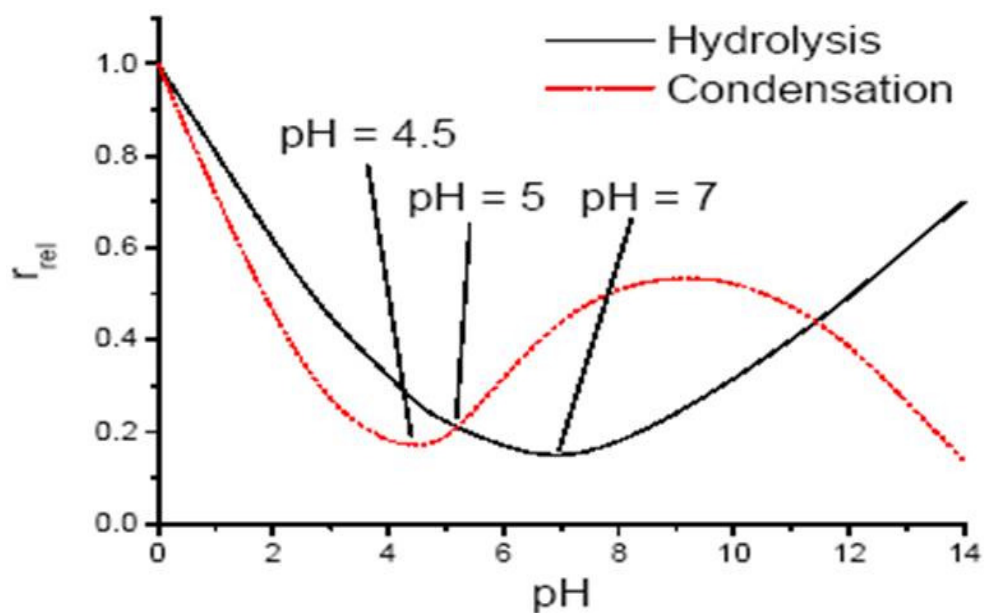
The solution with  $\text{pH} < 2$  in the following will be referred to as acidic medium whereas the one with  $\text{pH} \gg 7$ , that is Stöber synthesis, will be discussed among basic solutions as the most studied and interesting one.

### *Hydrolysis and Condensation*

The dependence of the relative rates of hydrolysis and condensation on pH is illustrated in Figure 1.2. It can be seen that under acidic conditions, the relative rate of the hydrolysis reaction exceeds that of the condensation. At  $\text{pH} = 5$  the two

reactions have the same relative rates and upon further increase of pH, i.e. under basic conditions, the rate of condensation exceeds that of hydrolysis.

One of the highly important parameters that influences the velocity of hydrolysis is the water-to-silicon alkoxide molar ratio,  $h$ . The higher the ratio, the faster is hydrolysis as there is more water available per mol of alkoxide precursor. The rate of hydrolysis is of the first order with respect to TEOS concentration.

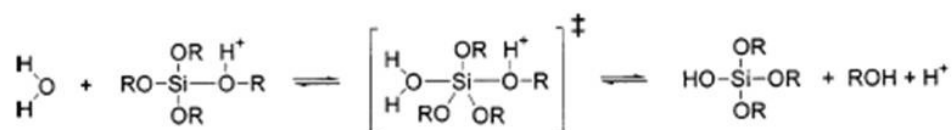


**Figure 1.2** Dependence of the relative rates of hydrolysis and condensation reactions on the pH [23].

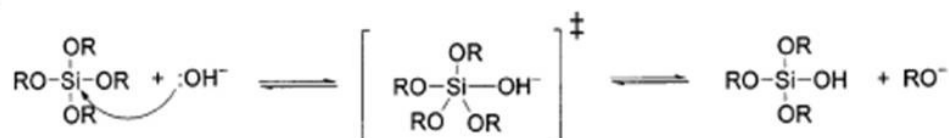
The hydrolysis and condensation reactions progress in acidic and basic medium is reported in Scheme 1.1.

## 1 Hydrolysis

A) acidic conditions

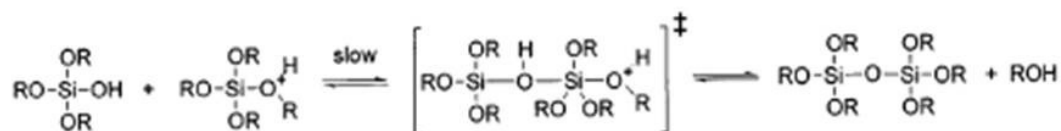
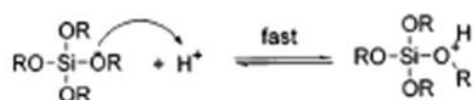


B) basic conditions

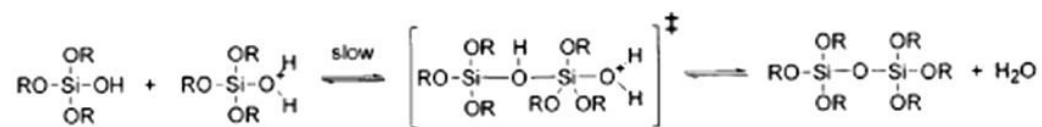
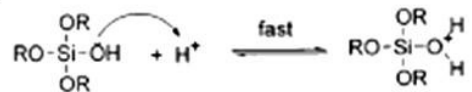


## 2 Condensation

A) acidic conditions



or



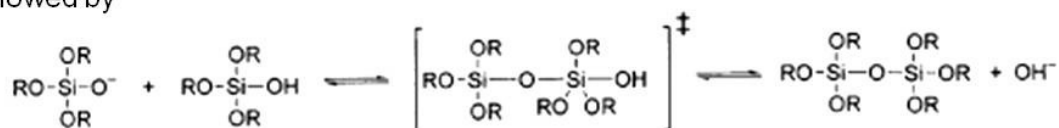
B) basic conditions



or



followed by



**Scheme 1.1** Hydrolysis (1) and condensation (2) of silicon alkoxide under acidic (A) and basic (B) conditions.

### *Gelation*

In this step a low viscosity liquid, sol, bonds into a three-dimensional network with a much higher viscosity. The characteristic of the network are greatly influenced by the size of particles and degree of cross-linking prior to gelation. The sol transforms into gel by collision and growth of the particles which gradually become more and more interconnected and at some point can support stress elastically, this is defined the gelation point.

### *Aging*

A range of processes, including formation of further cross-links, happen at this point. Structural changes of gel, such as decrease of porosity and increase of thickness, take place in order to increase the strength of the gel as it needs to resist during drying.

### *Drying*

At this point liquid (water, alcohol or other volatile components) is removed from the interconnected network, first as syneresis (the expulsion of liquid as the gel shrinks) then as evaporation with associated development of the capillary stress which can lead to cracking of the gel. Therefore, the drying process needs to be controlled carefully or by addition of surfactant, by elimination of very small pores, by use of supercritical fluids (e.g. CO<sub>2</sub>), etc.

### *Stabilization*

This involves the removal of surface silanols and hydrogen bonded pore water to have chemically stable ultraporous solid.

### *Densification*

It is the only step of the sol-gel process that involves high temperatures. Thermal treatment leads to collapse of the open structure by elimination of the pores and formation of a dense ceramic. Temperature depends on the dimensions and connectivity of the pores and on the surface area.

The final size of silica particles depends on the nature and the initial concentration of electrolyte (acid or base), the type of silicon alkoxide, nature of the solvent used and reactant temperature. Nature of the solvent (ethanol,

methanol, dioxane,) and nature of the acid (strong, weak, inorganic and organic) also play an important role but they have been called the “secondary effects”. At higher temperature larger particles are produced due to greater silica solubility [3]. The type of silicon alkoxide is also important because the longer and the bulkier the alkoxide group, the slower is the rate of hydrolysis. Besides these steric effects, there is also difference in stability. Even though TMOS is less bulky and therefore hydrolyzed faster than TEOS, it is instable to air so in its presence the synthesis must be carried out under nitrogen or argon what makes it more complex.

The hydrolysis is faster in acidic solution and directly proportional to the concentration of  $\text{H}_3\text{O}^+$  but condensation is slower and this is the reason for the formation of linear polymers whereas in basic medium hydrolysis, directly proportional to the concentration of  $\text{OH}^-$ , is slower and condensation is faster which favors large, bulky and ramified structures. Typical sequence of condensation is monomer, dimer, linear trimer, cyclic trimer, cyclic tetramer, etc. until higher order of stricter is generated to form colloidal particles. The sequence requires both the depolymerization (ring opening) and presence of monomers (including those produced by depolymerization). However at low pH depolymerization rate is very low, therefore the condensation is irreversible so the siloxane bonds cannot be hydrolyzed once they are formed and rearranged into particles. In acidic medium the polymer growth takes place through coupling of clusters, therefore the result is the more linear, open structure. In the presence of strong bases the polymer grows through addition of monomers, which are originated, beside by the reaction of the alkoxide hydrolysis, by the concurrent depolymerization reaction so the final product is branched polymer with high degree of cross-linking [23,30].

### 1.2.3 Stöber Synthesis

Stöber et al. [31] found out that using ammonia as a catalyst for the TEOS hydrolysis can control both the morphology and size of the powders, yielding the so-called Stöber spherical silica powder. The Stöber synthesis is carried out in extremely basic conditions and it is the ammonia-catalyzed reaction of silicon alkoxide with water, in low-molecular-weight alcohols. Monodisperse, spherical silica nanoparticles with the size in the range from 5 to 2000 nm can be produced [32,33]. The final size and shape are governed by the initial concentration of water and ammonia, the type of silicon alkoxide (methyl, ethyl, pentyl, esters, etc.), alcohol employed (methyl, ethyl, butyl, pentyl) and reactant temperature [3].

Two models have been proposed in order to explain the chemical and/or physical growth mechanisms of silica, i.e. monomer addition [34,35] and controlled aggregation [36,37]. Both models divide the formation of silica into two events: nucleation and growth. The monomer addition model suggests an initial burst of nucleation where the growth occurs through the addition of hydrolyzed monomers to the particle surface. On the other hand, the controlled aggregation model proposes that nucleation occurs continuously throughout the reaction where the primary particles or nuclei aggregate with one another or larger aggregates to eventually produce a narrow size distribution. Some authors think that both mechanisms are responsible for the growth saying that controlled aggregation occurs for much of the reaction and it is followed by monomer addition to the colloid surface, making it smoother [38,39]. Both groups of researchers agree on the fact that there is an induction period where no particles are formed while afterwards low-density nuclei are observed.

The reaction is nucleophilic substitution ( $SN_2$ ) which involves the displacement of the ethoxy group of TEOS by  $OH^-$  through a pentacoordinate transition state and it has first-order kinetic dependence on the concentration of both TEOS and  $OH^-$ .  $^{29}Si$  NMR spectroscopy gave a great contribution to these findings and the possibility to study various reaction intermediates,  $Q_i^j$ , as each has a specific chemical shift with respect to the silicon alkoxide. The notation  $Q_i^j$ , where Q stands for the quadrafunctional Si atom, the subscript  $i$  for the number of siloxane bridges attached to Si, and superscript  $j$  for the number of silanol bonds



on Si, was first introduced by Brinker and Scherer [23] and since then the notation has been regularly used [40].

#### 1.2.4 Fluoride as Catalyst

The polymerization rate of a sol-gel system can be increased by addition of a catalyst and fluoride is the most commonly used for this purpose. The addition of  $F^-$  affects the hydrolysis of TEOS [41] and, more relevantly, is known to reduce the gelation time of silica and therefore frequently employed to enhance the condensation step [23]. It was proposed that the first step in the hydrolysis is a fast reversible formation of an intermediate where the  $F^-$  temporarily increases the coordination of silicon from four to five or six. This intermediate stretches and weakens the surrounding Si-OR bonds. The subsequent step is the nucleophilic attack of water on the hypervalent silicon and it is the rate determining. It leads to nucleophilic substitution by proton transfer and elimination of ROH. The substitution of  $F^-$  with  $OH^-$  reduces the electron density on Si because  $F^-$  is more electron-withdrawing than OH. The Si becomes more responsive to nucleophilic attack implying an enhancement of the condensation reactions [42].

HF is less effective in an acidic environment due to the low acidity of HF ( $pK_a = 3.20$ ) [43]. The dissociation of the HF is more hampered in an alcohol-rich environment. The polymerization rate is proportional to the concentration of both  $H^+$  and  $F^-$  [30] but in an acidic environment the concentration of anion is largely determined by the concentration of the acid in the system. A maximum in gelation time is found in systems containing low concentration of HF ( $1 \cdot 10^{-3}$  mol per mol TEOS). The HF is completely dissociated in basic environment and therefore highly affects the condensation reaction [44].

Subsequently the polymerization proceeds via the formation of higher branched polymers because the monomer concentration decreases more rapidly from the very beginning of the process. These indicate that the dimers and trimers do not play a significant role as intermediate species in the polymerization process catalyzed by fluoride ions.

Besides the expansion of the coordination state of silicon, which is the mechanism accepted by most of authors, other possible mechanisms were discussed:

- (i) the formation of hydrophobic bonding by replacement of the Si-OH bond with Si-F bond;
- (ii) changes in hydrogen bonding;
- (iii) changes in electrostatic interactions;
- (iv) changes in the solubility of silica [23].

## 1.3 Microemulsions

### 1.3.1 Surfactants

Molecules that have a hydrophilic and a hydrophobic moiety are defined amphiphilic. Because this dual nature can self-assemble into ordered structures in bulk solutions and have the ability to accumulate at water-air interface thus decreasing the surface tension compared to that of pure water. They also reduce the interfacial tension between organic solvent and water by adsorbing at the liquid-liquid interface. That is why they are also named surfactants which derives from the **surface active agent**.

In aqueous solutions the tendency of the hydrophobic region to avoid contact with water is the basis of the association of molecules in micelles which are formed spontaneously when the concentration of surfactant exceeds a certain value named *cmc* (critical micelle concentration). Their formation results from an enthalpic contribution, due to interactions between the hydrophobic tails, and an entropic contribution arising from the difference in the organization of water molecules in the presence of free surfactant molecules and in the presence of micelles.

Surfactants are divided into ionic and nonionic, depending on the hydrophilic head. Ionic surfactants are divided into subgroups, cationic and anionic, on the basis of the charge of the head group. When there are both charges present in the head group, the surfactant is named zwitterionic. Amphoteric surfactants change their nature from cationic, zwitterionic to anionic with increasing pH.

Nonionic surfactants are not charged. Their hydrophilic head is usually a short polyethyleneoxide chain or more rarely a polyhydroxyl chain. At difference with ionic surfactants, nonionic are not sensitive to hard water and are usually compatible with other types of surfactants and therefore their production and usage are increasing.

The behavior of the surfactants is influenced by the hydrophilic-lipophilic properties, geometrical shape of the molecule and by curvature of the surfactant film.

### *HLB*

The hydrophilic-lipophilic balance (HLB) is an empirical number and it was defined in 1949 by William Griffin [45] as the ratio of hydrophilic and lipophilic moiety in the molecule and in general it applies for nonionic surfactants only. It is a value ranging between 0 and 20 and it defines the affinity of the surfactant partitioning between oil and water. HLB numbers can be calculated according to Equation (1.1):

$$HLB = 20 \frac{M_h}{M} \quad (1.1)$$

where  $M_h$  is the mass of the hydrophilic moiety and  $M$  is the molecular mass. The HLB for ethoxylated surfactants can be calculated multiplying by 20 the weight of polyethyleneoxide fraction in the molecule [46].

The surfactants with  $HLB > 10$  have an affinity for water and those with  $HLB < 10$  for oil and therefore the former are used for the formation of o/w microemulsions and the latter for the w/o microemulsions.

### *Packing Parameter*

A prediction of the structure of an aggregate can be done considering the molecular geometry of the surfactant, which is described by the packing parameter  $N$ :

$$N = \frac{V}{al} \quad (1.2)$$

where  $V$  is the molecular volume,  $l$  is the length of the extended hydrophobic chain and  $a$  is the effective area of the hydrophilic head resulting from the balance between the attraction of the hydrophobic chains and the repulsion between the heads taking into account hydration. The classification of self-assemblies in water, based on this parameter, is reported in Table 1.1 [47].


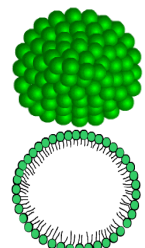

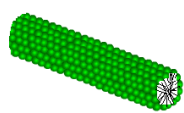



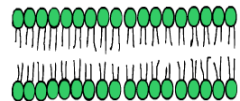

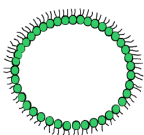
The actual area of the hydrophilic head and consequently the packing parameter changes with concentration and thus vary the curvature of the aggregate. The transition from one type of aggregate to another may occur together with phase changes.

### *Spontaneous Curvature of the Surfactant Film*

A spontaneous curvature is that adopted by a surfactant film in the absence of constraints. This means that a surfactant film bends spontaneously towards the medium where the surfactant molecule is more soluble (Bancroft rule). That is because it possesses bending elasticity which is governed by the properties of head and tail.

In the ternary systems, surfactant/oil/water, if the polar head is bulkier than the hydrophobic tail the film will curve towards water, that is oil-in-water structures will be favored and this is, by convention, defined as positive mean curvature. On the other hand, a negative mean curvature favors water-in-oil structures and they form when the head is less bulky than tail. If the head and tail have more or less the same form, the surfactant has the shape of a cylinder so the zero mean curvature is obtained. This also occurs when to the surfactant with bulky head is added a cosurfactant with bulky tail, or vice versa. Cosurfactants are lower alkanols such as butanol, pentanol, hexanol and others [47].

**Table 1.1** Surfactant packing parameters and geometry of self-assemblies in water.

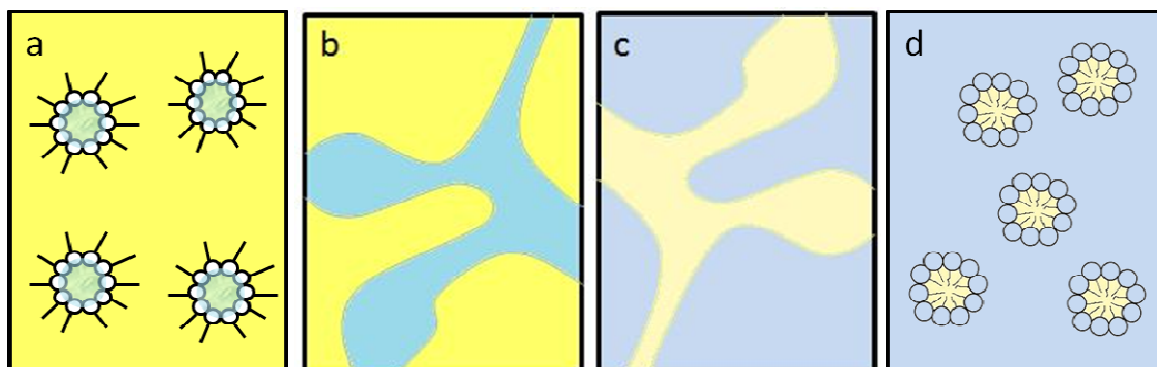
Packing parameter	Surfactant molecule	Geometry of aggregate
$N < \frac{1}{3}$		spherical micelles:  transversal view of a micelle
$\frac{1}{3} < N < \frac{1}{2}$		cylindrical micelles: 
$\frac{1}{2} < N < 1$		vesicles and/or flexible bilayers:  transversal view of a vesicle
$N \approx 1$		lamellas and/or planar bilayers:  transversal view of a bilayer
$N > 1$		inverse micelles:  transversal view of an inverse micelle

### 1.3.2 Types of Microemulsion

A mixture of two immiscible fluids plus a surfactant, which lowers the interfacial tension between the two, may result in the formation of emulsion or microemulsion. The main difference between emulsions and microemulsions is the stability and the size of the droplets. The former is kinetically stable, as it consists of roughly spherical droplets of one phase dispersed into the other, whereas the latter is thermodynamically stable. The droplets are about 100 times smaller in the latter, with a diameter size ranging from 5 to 200 nm, and because the size is less than 25% of the wavelength of the visible light microemulsions are transparent. They are macroscopically homogeneous but microscopically heterogeneous systems. Their thermodynamical stability is due to the very low interfacial tension between oil and water microdomains allowing their intimate contact. The microdomains are not static but in continuous movement and collision, allowing the exchange of material between droplets thus making them highly suitable as reaction media. The stability of the microemulsion can be influenced by the presence of further compounds, by temperature or pressure.

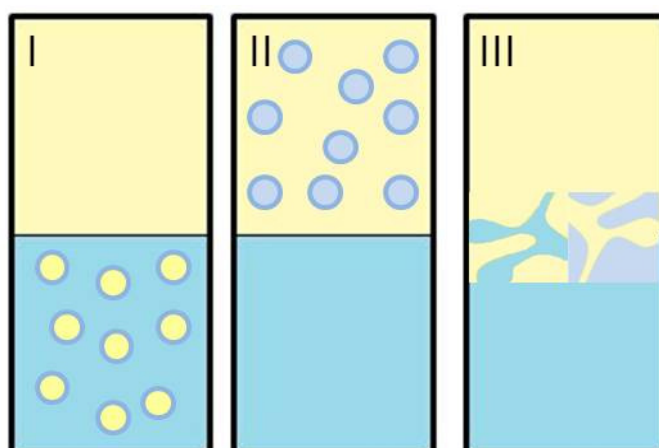
In 1943 Hoar and Schulman first described such colloidal dispersion as transparent emulsion and in 1953 assigned to it the name microemulsion [48]. Microemulsions were used long before they were characterized, as the first commercial microemulsion was liquid wax discovered by Radawald in 1929. However, not until 1970 they became widely investigated as it was discovered that they can improve oil recovery and therefore be used as source of income. Nowadays, the applications are extremely wide, from the classical ones in detergency and lubrication, to more modern ones, e.g. in catalysis, nanoparticles synthesis, solar energy conversion, etc. [49].

There are two basic types of microemulsions, dispersed and bicontinuous. In dispersed microemulsions droplets are present stabilized by surfactant while in the bicontinuous microemulsions a continuous network of water and oil is separated by membrane formed of surfactant molecules [47]. Each of the two types is further subdivided into water-in-oil (w/o) and oil-in-water (o/w) structures, and they are all illustrated in Figure 1.3.



**Figure 1.3** Types of the microemulsions: a) water-in-oil dispersed, b) water-in-oil bicontinuous, c) oil-in-water bicontinuous and d) oil-in-water dispersed.

At low surfactant concentration, there is a sequence of phase equilibria which depends on temperature and the nature of the constituents. These are referred to as Winsor phases (Figure 1.4) and they differ in number of phases in equilibrium [50]. Winsor I and Winsor II systems consist of two phases, in the former the lower o/w microemulsion phase is in equilibrium with the upper excess oil, whereas in the latter the upper w/o microemulsion phase is in equilibrium with excess water. Winsor III consists of three phases, middle o/w plus w/o bicontinuous microemulsion phase is in equilibrium with upper excess oil and lower excess water. The systems corresponding to a Winsor IV are classified as single phase microemulsions (not reported in Figure 1.4). By changing the composition of the system interconversion among Winsor phases can be reached.



**Figure 1.4** Winsor phases.

A water-in-oil microemulsion is formed when water is dispersed in a hydrocarbon based continuous phase. A surfactant adsorbed at the water-oil interface self-assembles to generate discrete aggregates known as inverse, reverse or inverted micelles. The surfactant orients its polar head towards the core of the micelles and the hydrophobic tail maintains favorable contact with oil. This occurs when surfactant packing parameter is  $>1$ , implying a negative spontaneous mean curvature. Beside this parameter, the formation of inverse micellar systems is influenced by the type of oil and surfactant, their concentration, the presence of electrolyte, the nature and valence of counterion, if present, the temperature, pressure, etc. Another important parameter is water-to-surfactant molar ratio,  $R = [H_2O]/[surfactant]$ , responsible for the size of micellar core. Only slight variation of these parameters can lead to completely different structures, therefore they must be carefully controlled.

### 1.3.3 Inverse Microemulsions as Reaction Media for the Synthesis of $SiO_2$ Nanoparticles

Synthesis of nanoparticles in microemulsion has been a subject of intense study since the early 1980's as it offers a unique method to control the kinetics of particle formation and growth by varying the physicochemical characteristics of the microemulsion system [4]. It is a powerful method where expensive or specialized instruments are not needed and the product obtained is microhomogeneous. The nanodroplets do not only act as nanoreactors, but also provide steric barrier to prevent the aggregation of nanoparticles. In microemulsion surfactant is partitioned between the oil, water and the interface of the micelles. For maximum effect it is desirable to have most of the surfactant at the interface rather than dissolved in oil or water. This compartmentalization usually makes chemistry in colloidal systems much different from that in homogeneous solutions and the equilibrium constants and reaction rates frequently vary by more than an order of magnitude in the two systems.



Formation of colloidal particles in w/o microemulsions occurs not only through the polymerization of monomers into polymeric reacting species but also through the subsequent polymerization of polymeric species into larger ones. This polymerization process usually occurs through the dynamic fusion and fission of w/o microemulsion droplets which host reacting species and are in continuous Brownian motion, at room temperature. Therefore, the steric hindrance of the surfactant film to the exchange between droplets through transient dimer formation usually increases with increasing the species size [51,52]. After reaching a critical size, polymeric species become nuclei which are confined inside individual droplets and do not undergo intermicellar dynamic exchange because sufficiently large intermicellar channels cannot be formed. These nuclei then adsorb small monomeric or oligomeric species to their surfaces and grow into particles. Therefore it is clear that the size of colloidal particles formed in w/o microemulsion is directly influenced by two factors:

(i) the number of micelles that host reacting species; the greater the number the greater will be the number of nuclei

(ii) the steric barrier to the intermicellar exchange provided by surfactant films; for films with a lower deformability or a stronger attachment to micelles, intermicellar water channels are less likely to occur.

The exchange rate between the micelles can be varied by controlling water-to-surfactant molar ratio,  $R$ . The ethyleneoxide (EO) groups of the nonionic surfactant in inverse micelles interact with water molecules through hydrogen bonding, and the driving force in the aggregation phenomenon is the dipole-dipole interaction between hydrated EO groups. At very low  $R$ , water preferentially solvates some of the EO groups along the polar head, and it is considered bound, and the micelle interface is rather rigid thus intermicellar exchange and growth rates of nanoparticles are lowered. Further addition of water results in the gradual formation of free or unbound water rather than in complete hydration of all the EO groups and the film becomes more fluid, so the rate of growth increases, as there is more core water available for the reaction. Increasing the water content a point is reached where water molecules with properties of bulk water are present in the hydrophilic domain. This is relevant for the formation of particles since hydrolysis reaction is facilitated. However, it must be taken into consideration that there is an upper limit as above a certain  $R$  the system is no more stable [53,54]. Many

reports show the dependence of nanoparticles size on R parameter, though this correspondence in the increase of the size with increasing R cannot be generalized.

This kind of systems are very advantageous for nanoparticles synthesis since the reactions can be performed inside the micellar cores and the size of the products may be further modified through the rationale choice of the hydrocarbon solvent [55] and the surfactants molecular structure [54]. Not only the quantity of water influences the size and the shape of final product [56] but also the properties of aqueous core, whether is basic [57-59] or acidic [8].

### *Solvent*

An organic solvent, often an alkane, is an essential component to form a stable w/o microemulsion. Its polarity and viscosity affect the size of silica nanoparticles. However, little attention has been paid to the role of the molecular dimensions and structure of an organic solvent but it is expected that they affect intermolecular forces and association free energy between the organic phase and surfactant in an inverse microemulsion. Jin *et al.* [55] investigated the possibility to control the size of silica nanoparticles by means of organic solvent. They noted that the increase of the molar volume of the single organic solvent increased significantly the nanoparticles size by increasing the size of the micelles where the synthesis takes place. With organic solvents with long alkane chain, such as *n*-hexadecane and *n*-decane, the water droplets become much larger and the microemulsion is unstable. In this case, solvent polarity may have become a determining factor and the long alkane chain was too hydrophobic to form a stable microemulsion with water. Oil molecules with a shorter length or a higher polarity (e.g. cyclohexane) can swell the hydrophobic layer of surfactant film to a larger extent by orienting themselves more easily along the surfactant tail or by penetrating more deeply toward the surfactant head thus increasing surfactant curvature and rigidity reducing the size of droplets. Therefore, the size of silica nanoparticles can be tuned by varying the molar volume of an organic solvent.

### *Type of Surfactant*

The most widely studied inverse micellar system is the one formed by the two-tail ionic surfactant known as AOT (sodium bis(2-ethylhexyl) sulfosuccinate). On the other hand, nonionic surfactant inverse micelles have been less studied despite the fact that they are commonly used. Nonionic surfactant inverse micelles can differ significantly from ionic surfactant systems, and extending the general conclusions reached for ionic systems to nonionic ones must be done with caution. The hydrophilic segment of typical nonionic surfactants is composed of polyethyleneoxide oligomers, and this moiety can occupy a considerable portion of the micellar core, particularly in small micelles.

The HLB value of the surfactant is effective parameter when choosing the type of the surfactant for the synthesis of nanoparticles in microemulsion. The surfactants with HLB less than 10, such as Span 80 and Span 20, are preferred for microsphere synthesis whilst surfactants with middle range HLB, between 10 and 15, such as NP-5, NP-9, Triton X-114 and AOT, are normally selected for nanoparticles synthesis [22].

Cmc values for nonionic surfactants are in the range  $10^{-3}$ - $10^{-5}$  mol L<sup>-1</sup>, which is 1-2 orders of magnitude lower than for the ionic surfactants with the same hydrophobic chain. This is due to the absence of ionic head groups which lead to electrostatic repulsion during micelle formation. Moreover, nonionic surfactants exhibit only a small effect in the presence of electrolytes compared to ionic surfactants [60].

The length of the hydrocarbon tail and the size of the hydrophilic head of the nonionic surfactant also have effect on the size of the particles. Smaller nanoparticles are favored by both longer tails and bigger head groups. The longer chain makes the surfactant film less deformable imparting a higher steric hindrance to hydrolyzed silica reacting species, hence leading to the smaller particles. The bigger head groups result in more water binding to the surfactant, thereby decreasing hydrolysis rates [61].

Commercial nonionic ethoxylated surfactants are synthesized by a polycondensation reaction the result of which is a mixture of oligomers whose degree of ethoxylation, so-called ethylene oxide number (EON), varies according to a Poisson's distribution [62]. As a consequence, these surfactants in a surfactant-oil-water system can provoke phenomena such as selective

fractionation or selective partitioning. In such a case, each oligomer exhibits its individual affinity for the bulk oil and water phases and the surfactant mixture at the interface can be strongly different from the one added in the system in the first place. For alkyl phenyl ethoxylated surfactants, the partition coefficient has been found to vary, besides as a function of EON, with the branching of hydrophobic tail as well as with number of carbon atoms in the alkyl group.

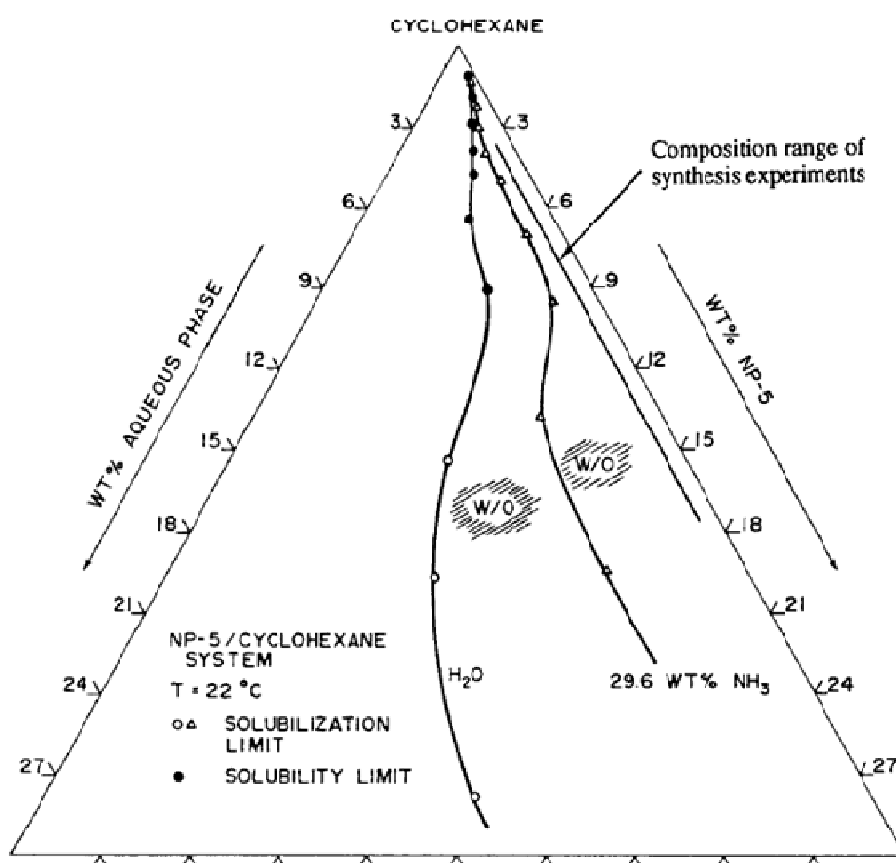
There are some surfactants that require the use of cosurfactant in order to form a stable microemulsion. The addition of a cosurfactant makes the interfacial film more fluid, thus increasing the rate of intermicellar exchange but also leading to a higher curvature of the droplets, therefore smaller particles. Moreover, the formation of smaller particles is favored by employing cosurfactants with a shorter chain [63]. One of the examples where the cosurfactant is required is the system *n*-decane/water/Triton X-100 where in absence of *n*-hexanol the microemulsion cannot be formed [55].

### *Basic Microemulsion*

As already mentioned, the synthesis of silica in a basic medium, more precisely in water-alcohol-NH<sub>3</sub> system, commonly referred to as Stöber synthesis [31], provides nanometric silica particles with a good control over final particle size. More effective method for controlling the growth of the polymer and its final particle dimensions, also in the presence of NH<sub>3</sub>, is by using nonionic inverse microemulsions.

The solution composition necessary to form a single-phase w/o microemulsion for the NP-5 surfactants was investigated for Igepal CO520 (5 polyoxyethylene nonylphenyl ether) at 22 °C [54] and Igepal CA520 (5 polyoxyethylene iso-octylphenyl ether) at 23 and 25 °C in *n*-heptane/aqueous solution [64,65]. More pertinent was the Igepal CO520/cyclohexane/aqueous solution investigated at 22 °C by Osseo-Asare and Arriagada [59]. A section of the ternary phase diagram in Figure 1.5 is illustrating the inverse microemulsion regions for water and concentrated ammonium hydroxide. The latter is acting as a lyotropic salt reducing the mutual solubility between the water and the surfactant. This may be interpreted as the result of the competition between hydroxyl ions and the oxyethylene groups of the surfactant for interaction with water molecules. The

hydration swelling of head groups is decreased in the presence of ammonia and therefore the surfactant's head-to-tail area ratio is decreased. This leads to the formation of droplets with smaller hydrodynamic diameter in the presence of aqueous ammonia than in the presence of pure water [66,67]. Moreover, as the ammonia concentration decreases the particle morphology becomes more irregular and the effect appears to be more significant at high R. However, it is suggested that increase in ammonia concentration, by resulting in shrinkage of the microemulsion stability region, should lead to an increase in the intermicellar exchange rate. This should promote particle aggregation and give rise to larger particle [58].



**Figure 1.5** Phase diagram for the Igepal CO520/cyclohexane/aqueous solution at 22 °C where aqueous solutions are water and concentrated ammonia hydroxide (29.6 wt%) [59].

### *Acidic Microemulsion*

The synthesis of silica nanoparticles in an acidic medium is nanotechnologically of a great interest, owing to the different physical nature of silica synthesized under acidic rather than basic conditions. For example, by switching from base to acid catalysis, the structure of the silica gel can be tuned from meso to microporous, consequently restricting the diffusion of the encapsulated molecules out of the silica matrix and thus decreasing their release rate. Moreover, the acidic medium makes the application more extensive since guest species wished to encapsulate are not always base resistant. Unfortunately, the application of an acid-catalyzed sol-gel process for the synthesis of nanosized silica is less than straightforward. As a matter of fact, acid-catalyzed syntheses carried out in a solution or a biphasic medium can provide microsized particles [68,69], while mesoscopic silica spheres prepared in the presence of templating agents have diameters larger than 100 nm [70]. The inverse micelles, already extensively used for the base-catalyzed synthesis of silica nanoparticles, seem to be an optimal reaction medium able to limit the growth of polymerizing silica within the nanometer range in the presence of an acid catalyst [8,71]. However, at the state of the art only few studies are reported about it, and just one concerns the whole process in an inverse microemulsion, with a water core that remains stable throughout course of the reaction [8]. Such system consists of the Igepal CO520 as surfactant, cyclohexane as oil, HNO<sub>3</sub> solution containing NaF as aqueous phase, and tetramethyl orthosilicate (TMOS) as reagent. The addition of NaF is due to its recognized ability to catalyze both the hydrolysis and the condensation step. The mechanism of the fluoride anion which favors various crystallization processes, such as biomineralization [72], has been described in section 1.2.4.

## 1.4. Pulsed-field Gradient STimulated Echo NMR

### 1.4.1 Introduction

There are two types of motions experienced by the molecules in solution distinguished by quite different time scales, the rotational diffusion and translational diffusion. The former is on the picoseconds to nanoseconds time scale and reflects the reorientational motions in molecules. It is indicated by rotational correlation time ( $\tau_c$ ) and can be obtained by NMR relaxation measurements. The latter is, however, on the milliseconds to seconds timescale and reflects the random translational motion of molecules (or ions) which is the essential form of transport in chemical and biochemical systems responsible for all chemical reactions. This motion, known also as self-diffusion, takes place at constant concentration therefore it is not induced by concentration gradient. It is defined by self-diffusion coefficient  $D$  ( $\text{m}^2 \text{s}^{-1}$ ) and is related to molecular size, as dictated by Stokes-Einstein equation:

$$D = \frac{kT}{3\pi\eta d_h} \quad (1.3)$$

where  $k$  ( $1.38 \cdot 10^{-23} \text{ JK}^{-1}$ ) is the Boltzmann constant,  $T$  (K) is temperature,  $\eta$  (Pa s) is viscosity and  $d_h$  (m) is hydrodynamic diameter. The relation is valid only for the spherical particles but generally molecular shapes are more complex and therefore the equation must be modified accordingly. Molecules will diffuse in all directions during a defined amount of time and not every molecule will reach the same distance from the starting point, therefore the root mean square (RMS) distance  $z$  is employed:

$$z = (2Dt)^{1/2} \quad (1.4)$$

and it represents an ensemble average of the molecules in solution. In order to measure true translational motion  $z$  needs to be much larger than  $d_h$ . The condition may not hold for large molecules like proteins and polymers and in that case the translation of a chain segment or the rotational diffusion is measured.

The diffusion experiments are frequently employed tool in the surface and colloid chemistry, especially for the study of micelles and inverse micelles. The diffusion coefficients are very useful for the determination of the aggregates size and/or shape and for the study of the microemulsion structure as a function of composition since able to indicate whether the phase change has occurred [73].

### 1.4.2 Pulsed Field Gradient NMR

The use of pulsed field gradient (PFG) NMR techniques to measure self-diffusion coefficients dates back to 1965 [74]. The method relies on differences in diffusion coefficients, and therefore in the molecular size, as a mean to analyze components in a solution mixture in a non-invasive mode.

In the PFG method, the attenuation of a spin-echo signal resulting from the dephasing of the nuclear spins due to the combination of the translational motion of the spins and the imposition of spatially well-defined gradient pulses is used to measure the former. The Equation (1.5) describes how the gradient along  $z$  axis labels the spatial position of nuclear spins through their Larmor frequency,  $\omega_z$  (rad  $s^{-1}$ ):

$$\omega_z = \gamma B_0 + \gamma G_z z \quad (1.5)$$

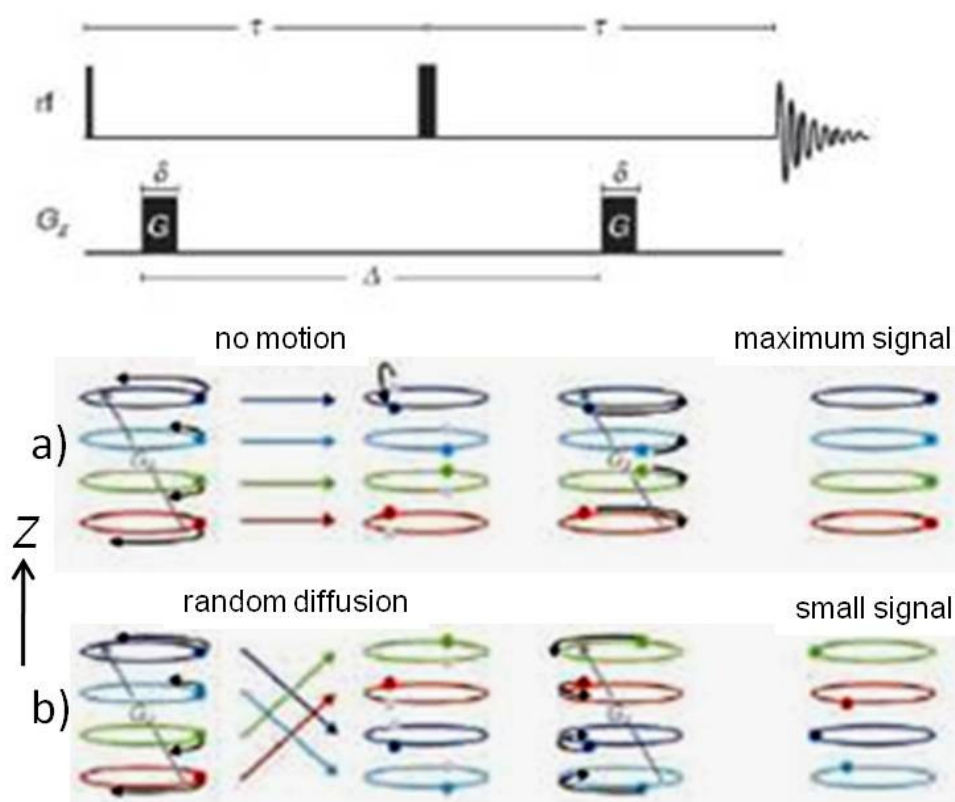
where  $\gamma$  (rad  $T^{-1} s^{-1}$ ) is a gyromagnetic ratio,  $B_0$  (T) is the strength of the static magnetic field oriented in  $z$  direction,  $G_z$  is the gradient applied in  $z$  direction and  $z$  is the position of the spin along the  $z$  axis. For single quantum coherence the induced position-dependant phase angle of the spins,  $\varphi_z$  (rad) is:

$$\varphi_z = \gamma G_z z \delta \quad (1.6)$$

where  $\delta$  (s) is the time duration of the applied gradient. After the application of  $90^\circ$  radio-frequency (RF) pulse the magnetization is brought to the  $xy$  plane with the coherent phase of the spins. The application of the gradient spatially encodes the spins, i.e. labels the position of the spins by producing a spatially dependent phase angle, because the Larmor frequency varies along  $z$  axis during the



gradient pulse. The spins present in each plane of the sample, perpendicular to  $z$  axis, are affected equally (Figure 1.6). At this point the system is left to evolve. During the evolution the spins undergo the translational diffusion and therefore change their position along the  $z$  axis. The chemical shifts and frequency dispersions due to residual  $B_0$  inhomogeneities are refocused by the application of the  $180^\circ$  RF pulse, therefore the magnetization is rotated and the sign of the phase angle is reversed. The second gradient, equal in magnitude and duration to the first one, is applied and spin positions are decoded. This second gradient will refocus the magnetization of all the spins dephased by the first one if the spins have not undergone any translational diffusion, and the maximum signal would be obtained (Figure 1.6 a). However, if the spins have moved during the diffusion interval,  $\Delta$ , between the two gradients, refocusing is incomplete and proportional to the average molecular displacement in the direction of gradient so the signal is diminished (Figure 1.6 b). The faster the diffusion, the poorer is refocusing and the smaller is the resulting signal.



**Figure 1.6** The effect of the gradient on the phase shift and signal intensity in a PGSE experiment when diffusion is a) absent and b) random.

The experiment described is the Pulsed Field Gradient Spin Echo (PGSE), also called Stejskal–Tanner experiment. The signal attenuation in this experiment, considering also the relaxation processes, is represented by the equation:

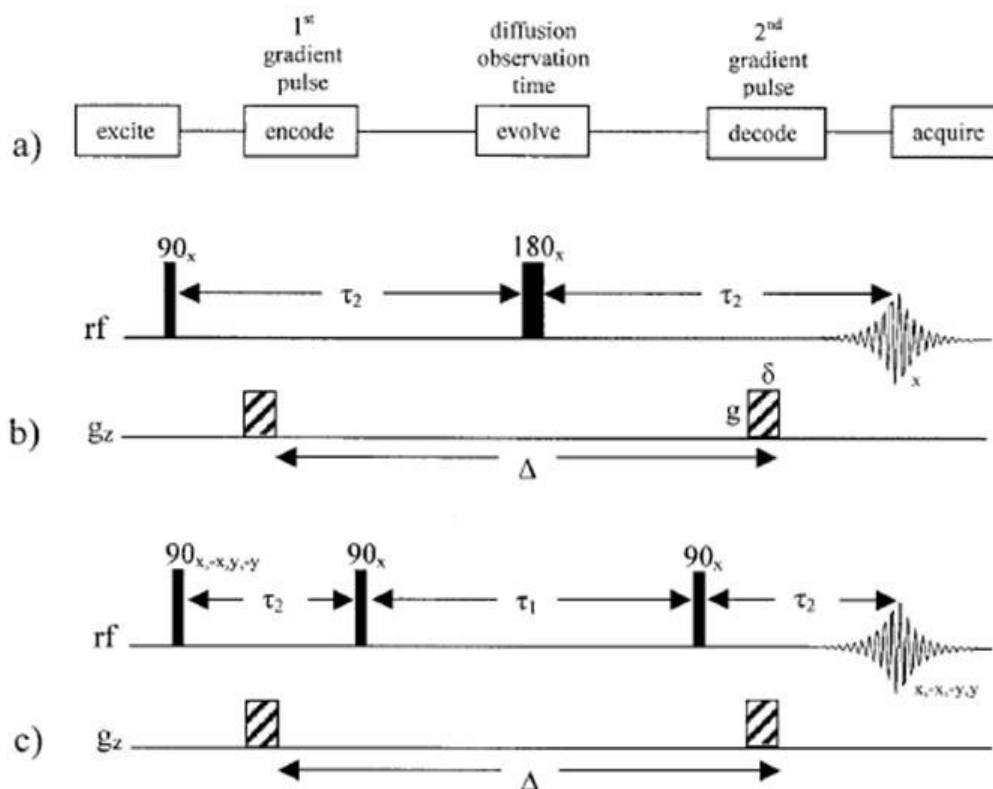
$$S_{2\tau_2} = S_0 \exp\left[-Dq^2 \left(\Delta - \frac{\delta}{3}\right) - \frac{2\tau_2}{T_2}\right] \quad (1.7)$$

where  $S$  and  $S_0$  are signal intensities in the presence and absence of  $G_z$ , respectively,  $D$  is the self-diffusion coefficient,  $q = \gamma_H G_z \delta$  with  $\gamma_H$  being the  $^1\text{H}$  gyromagnetic ratio. The final term takes in account nuclear relaxation governed by  $T_2$  as during the diffusion interval magnetization is placed in  $xy$  plane. If  $\tau$  is kept constant during all the experiments, the signal attenuation, due to relaxation, is constant and may be separated from the diffusion experiment. Equation (1.7) provides other three experimental parameters that can be varied during the diffusion measurement:  $G_z$ ,  $\delta$  and  $\Delta$ . An increase of one of these parameters will lead to increased signal attenuation and the former is the preferred variable in order to maintain the pulse sequence time duration constant.

In the PGSE experiment during the diffusion the magnetization is stored in  $xy$  plane and decays by  $T_2$  relaxation which is especially short for macromolecules. Moreover, the quality of the final spectrum is poorer due to  $J$  evolutions. This can be overcome by replacing the  $180^\circ$  pulse with two  $90^\circ$  pulses, as illustrated in Figure 1.7. The experiment Pulsed Field Gradient Stimulated Echo (PGSTE) has the advantage that the second  $90^\circ_x$  pulse stores the magnetization to the  $z$  plane by rotating only the  $y$  component whereas the disadvantage is that  $x$  component is eliminated by phase cycling or homospoil gradients (vs. for the  $90^\circ_y$  pulse). It can be seen from the Stejskal-Tanner Equation (1.8) that the signal intensity is reduced by a factor of two:

$$S_{2\tau_2+\tau_1} = \frac{1}{2} S_0 \exp\left[-Dq^2 \left(\Delta - \frac{\delta}{3}\right) - \frac{2\tau_2}{T_2} - \frac{\tau_1}{T_1}\right] \quad (1.8)$$

In the final term, referred to nuclear relaxation, it is taken in account the  $T_1$  relaxation during the diffusion interval as also the  $T_2$  relaxation present between first and second  $90^\circ$  pulse and after the third one. Only for small molecules  $T_1/T_2 \approx 1$  so the PGSE sequence may be preferred. However, for macromolecules  $T_1 \gg T_2$  so the benefits are much greater with respect to the loss of half of the signal.

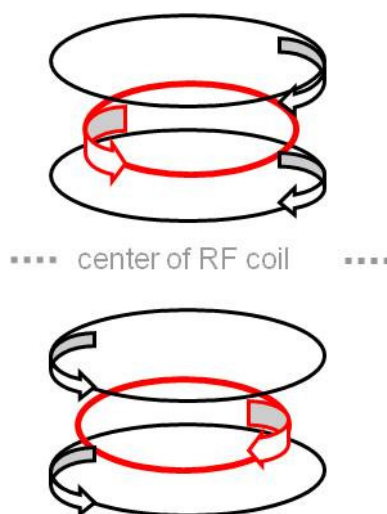


**Figure 1.7** PGSE NMR diffusion experiment: (a) the essential components, (b) the pulsed field gradient spin echo (PGSE) sequence, and (c) the pulsed field gradient stimulated echo (PGSTE) sequence [75].

### 1.4.3 Eddy Currents

Eddy currents are electrical currents generated in surrounding conductors, caused by rapid changes in gradient pulses and proportional to the strength of the gradient. The induced currents oppose to gradients and interfere with the main magnetic field. There are few methods to overcome their effect. In modern instruments the magnetic field gradients are produced by so called Maxwell pairs of coils positioned outside the main RF coil, one above and other below, and they carry current in opposite directions (Figure 1.8). Therefore, the field created by shielding the gradient coils cancels the fields produced by the main coil. Typically

a reduction of about 1% of eddy currents can be achieved [76]. It is important that the gradient is uniform along  $z$  direction.



**Figure 1.8** The main RF coil (red) and Maxwell pairs of coils (black).

Another way to overcome eddy currents is to pre-emphasize gradients. Increasing the current at the leading and trailing edges of the gradient pulses opposite signs from the eddy currents are produced in the required regions. This method puts the limitation on the maximum gradient strength.

It is also possible to use modified sequences of standard experiments. There are two possibilities, first is the longitudinal eddy-current delay (LED) sequence where an additional delay at the end of the sequence is introduced. It is called  $T_e$ , and stores the magnetization in  $z$  direction while eddy currents of the second gradient decay. At the end the  $90^\circ$  pulse is applied in order to shift magnetization back to  $xy$  plane. This method introduces additional heat which may produce convection artifacts.

One of the best solutions is to use self-compensating bipolar pulse-pair (BPP) gradient pulses.  $\delta$  is replaced by a combination of gradients  $(G)-180^\circ-(-G)$  with  $G = \delta/2$ . The two  $G$  are of opposite sign and the  $180^\circ$  pulse inverts the induced phase shift from the first gradient pulse within the pulse sandwich. Eddy currents induced by the first positive gradient are cancelled by the equivalent negative one, while  $180^\circ$  pulse prevents an encoding of chemical shifts which would cause signal attenuation.

The limitation of these two sequences is the time required as it might be too long, especially when  $T_2$  are short in macromolecular systems and it may lead to loss of the signal.

#### 1.4.4 Temperature Gradients and Convection Compensation

Due to the temperature gradients, liquid in nonviscous sample is moving along the sample axis. This is called convection and results in additional signal decay that can be mistaken for faster diffusion and therefore can make the diffusion analysis completely useless.

Assuming convection is constant in time and strictly laminar, its effect on diffusion can be efficiently eliminated. The experiment sequence is modified by applying the compensation block exactly halfway through the diffusion interval (Figure 1.9). The magnetization is moved to the  $xy$  plane by a  $90^\circ$  pulse and gets refocused by the first gradient. The second gradient, identical in sign, duration and length to the previous one, labels the phase of the spins in the opposite direction. The magnetization is then returned to the  $z$  axis for the second half of the diffusion delay. The ordered nature of convection assures that the phase evolution due to convection is opposite during the two halves of the diffusion delay and therefore compensate each other, while diffusion, being a random process, is not affected.

#### 1.4.5 Diffusion Ordered Spectroscopy (DOSY)

The most important application of PFG sequences is to measure the diffusion coefficients by means of diffusion ordered spectroscopy (DOSY). Generally speaking, DOSY increases the dimensionality of an NMR experiment by one.

In the simple DOSY spectrum the data are reported in two dimensions, where the axis of dimension 2 is the frequency and the axis of dimension 1 is the

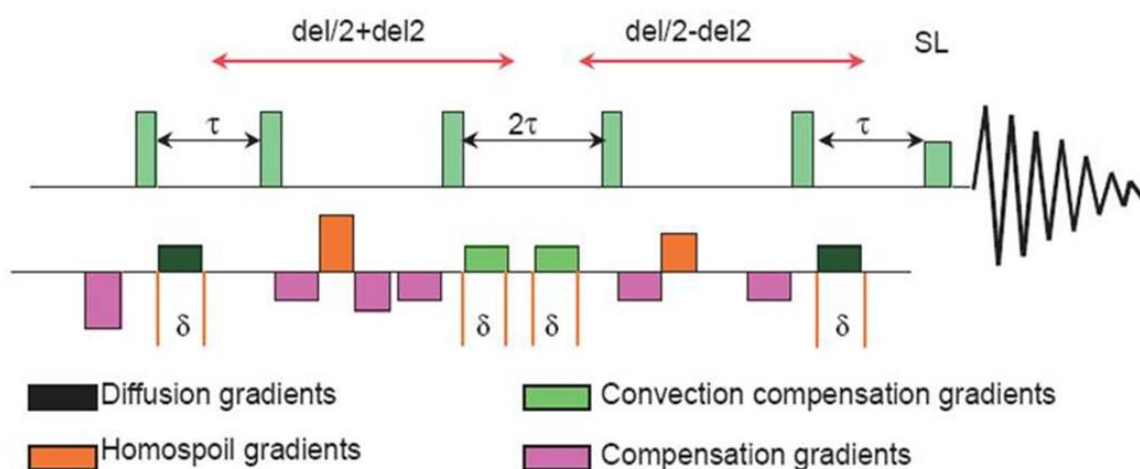
diffusion coefficient. The width of the peaks in the dimension 1 is the standard deviation of  $D$ . The data are commonly obtained by incrementing the “gradient effect” where its strength is arrayed and collecting all the FIDs. Approximate inverse Laplace transforms (ILTs) of the signal amplitude with respect to  $q^2$  yield the second dimension of a spectrum that correlates the chemical shift with its diffusion coefficient. Another possibility of analyzing data is to fit the echo intensities against  $q^2$  ( $\Delta - \delta/3$ ) on the basis of the Equation (1.8) and the components are then distinguished on the basis of the decay rate.

Diffusion coefficients errors can either be statistical or systematic. The most obvious source of statistical errors is inappropriate signal-to-noise ratio; therefore in DOSY experiments, relatively high S/N values must be reached even with the strongest phase encoding gradients. Systematic errors are primarily caused by instrumental imperfections (such as gradient nonlinearity over the active sample volume, phase distortions) and can be minimized by careful pulse sequence design and by adding a suitable internal reference to the sample.

#### *DgcsteSL\_cc*

Gradient Compensated STimulated Echo with Spin-Lock [77] and Convection Compensation [78] is a sequence provided by the software Varian VNMRJ. It is reported in Figure 1.9 and it was employed for the DOSY measurements in the present thesis work. The sequence is containing an identical number of positive and negative gradients in order to provide "internal" Eddy-current compensation. These currents create a secondary field that opposes the changing magnetic field at the beginning or end of gradient pulse and are cancelled by the negative gradients, indicated in purple in Figure 1.9. To overcome the convection problems halfway through the diffusion delay the magnetization is moved back to the transverse plane by a  $90^\circ$  pulse and gets refocused by the first green gradient pulse. The second green gradient, identical in sign, duration and length to the previous one, phase labels the spins in the opposite direction. The magnetization is then converted back to axial for the second half of the diffusion delay. Homospoil gradient pulses, colored in orange in Figure 1.9, are used to eliminate residual transversal magnetization during the diffusion delay. Of the 12 gradient pulses used in the pulse sequence only two (the black ones) are used to measure

the diffusion. Finally, the spin lock (SL) is used as a  $T_2$  filter to eliminate undesired broad signals.



**Figure 1.9** Gradient Compensated STimulated Echo with Spin-Lock and Convection Compensation pulse sequence [79].

## 1.5 Aims

The variety of application of  $\text{SiO}_2$  nanoparticles makes them highly interesting in many scientific fields and therefore their synthesis is studied intensively. However, the sol-gel process carried out in w/o microemulsion is not fully understood.

We aim to understand better the environment in which the synthesis takes place and to shed light on the evolution of the soluble species, both of the constituents of the microemulsion and of those taking part to reaction. We will follow the quantitative evolution of TEOS and EtOH and try to assess their preferential distribution in the various environments provided by this, on the mesoscale heterogeneous, reaction medium. Most authors agree that TEOS is localized mainly in the oil however they argue whether EtOH is preferentially in the water-pools or in oil.

The synthesis of SiO<sub>2</sub> nanoparticles in an acid-catalyzed system is especially interesting from nanotechnological point of view, owing to the different physical nature of silica synthesized under acidic rather than basic conditions, and from an applicative point of view since intended guest species are not always base resistant.

As acid-catalyzed inverse microemulsions are rather unexplored first we intend to characterize the system by means of <sup>1</sup>H, <sup>13</sup>C and PGSTE NMR, the hydrolysis and condensation will be studied by means of NMR, IR and SAXS. Besides synthesizing and isolating SiO<sub>2</sub> nanoparticles from the acid-catalyzed microemulsion, we aim at investigating to what extent, for acid-catalyzed systems, the slowdown of the hydrolysis step affects the overall process and, potentially, the size of the final particles.

The metal doped silica systems are important for optical applications [24] and if the metal ions are finely dispersed on silica matrix very efficient catalysators can be obtained [25]. Therefore the synthesis of silica nanoparticles in acidic inverse microemulsion will be carried out in the presence of both Cu<sup>2+</sup> and Co<sup>2+</sup> ions with the aim to get correspondingly doped nanoparticles.

Noteworthy, Cu<sup>2+</sup> and Co<sup>2+</sup> doped nanoparticles were scarcely investigated and their synthesis in acid-catalyzed inverse microemulsion has not been yet reported.

The evolution of the microemulsions and final products characterization will be supported by the results obtained on the very systems by means of SAXS, TEM, TGA and DSC by the group of professor Alvise Benedetti from INSTM and Ca' Foscari University of Venice.



## 2 EXPERIMENTAL

### 2.1 Materials

Igepal CA520 (5 polyoxyethylene iso-octylphenyl ether), tetraethyl orthosilicate (TEOS) with 98 % purity, cyclohexane, and aqueous ammonia (NH<sub>3</sub>) solution (29.6 %wt) were all purchased from Sigma Aldrich and used without further purification.

### 2.2 Preparation of samples

#### 2.2.1 Microemulsions

Microemulsions were prepared by dissolving the surfactant Igepal CA520 in cyclohexane at 0.1 M concentration. To 10 mL of the solution the required volumes of the inner phase were added:

(i) 0.161 mL of water, to reach a water-to-surfactant molar ratio  $R= 4.4$ , referred to as “H<sub>2</sub>O microemulsion”;

(ii) 0.161 mL of concentrated aqueous NH<sub>3</sub> (29.6 %wt), to reach  $R= 3.0$ , referred to as “NH<sub>3</sub> microemulsion”;

(iii) 0.1 mL of acidic solution of HNO<sub>3</sub> or HCl in the two different concentrations (0.1 M and 0.05 M), each in the presence of  $3.8 \cdot 10^{-2}$  M NaF and its absence, to reach  $R= 5.7$ , for the better understanding the names of the eight samples analyzed are listed in Table 2.1;

(iv) 0.1 mL of HCl 0.1 M containing 0.5 M of metal precursor, either  $\text{CuCl}_2$  or  $\text{CoCl}_2$ , to reach  $R= 5.2$  and metal-to-TEOS ratio of 0.065. The samples are referred to as  $\text{Cu}^{2+}$  and  $\text{Co}^{2+}$  doped system, respectively.

**Table 2.1** Samples investigated for the acid-catalyzed synthesis of  $\text{SiO}_2$  nanoparticles.

<b>HNO<sub>3</sub> systems</b>	<b>HCl systems</b>
HNO <sub>3</sub> 0.1 M	HCl 0.1 M
HNO <sub>3</sub> 0.05 M	HCl 0.05 M
HNO <sub>3</sub> 0.1 M + NaF	HCl 0.1 M + NaF
HNO <sub>3</sub> 0.05 M + NaF	HCl 0.05 M + NaF

### 2.2.2 Reaction Media

The reaction was initiated by adding the needed TEOS amount to the microemulsions previously prepared in order to obtain adequate “reaction medium”:

(i) in base-catalyzed system 0.191 mL of TEOS to obtain water-to-TEOS molar ratio  $h= 7.5$ ;

(ii) in acid-catalyzed systems 0.25 mL of TEOS to obtain  $h= 5.2$ ;

(iii) in doped systems 0.171 mL of TEOS to obtain  $h= 6.5$ .

“H<sub>2</sub>O microemulsion” was not used as reaction medium.

### 2.2.3 Classical HCl-Catalyzed Sol-Gel

Adaptation of a literature procedure [44] was applied for comparison of the silica samples and referred to as classical HCl-catalyzed sol-gel. Two separate solutions were prepared:

- (i) 3.49 mL of EtOH and 10 mL of TEOS
- (ii) 1.62 mL of HCl 0.01 M and 3.49 mL of EtOH.

The first solution was added to the second one and the mixture was stirred for 40 min at room temperature. 20 h afterwards the solid was filtered and washed with EtOH and water. Finally, the product was dried at 110 °C for 24 h.

### 2.2.4 Isolation of Nanoparticles

The nanoparticles had been isolated from the reaction medium 1 week after the reaction commencement in base-catalyzed system, and 2 to 3 weeks in acid-catalyzed and doped systems.

The basic microemulsion was broken by addition of acetone, the lower phase was collected, the solvent evaporated, and the solid was washed three times with dichloromethane.

In the acidic medium the solvent was evaporated and the residue, consisting mainly of Igepal, was washed only two times with dichloromethane in order to remove the surfactant only partially.

In the doped systems the solvent was evaporated and the residue, consisting also mainly of Igepal, was washed few times with each of the four solvents, dichloromethane, diethyl ether, water and acetone, to remove both the surfactant and excess of metal precursors.

## 2.3 NMR Measurements

### 2.3.1 $^1\text{H}$ , $^{13}\text{C}$ and $^{29}\text{Si}$ NMR Measurements

The NMR spectra were recorded on a JEOL Eclipse 400 (9.4 T) NMR spectrometer operating at 399.78 MHz for  $^1\text{H}$ , 100.53 MHz for  $^{13}\text{C}$ , and 79.42 MHz for  $^{29}\text{Si}$ . All spectra were acquired at room temperature without field-frequency lock.

For  $^1\text{H}$  NMR, four scans were acquired with  $20^\circ$  pulses, to avoid radiation damping due to the presence of the fully protonated solvent, employing a spectral width of 3.6 kHz over 8K complex points, interleaved by 12.3 seconds.

For  $^{13}\text{C}$ , 3300 scans were acquired employing  $45^\circ$  pulses and a 19.12 kHz spectral width over 32K complex data points.

The  $^{29}\text{Si}$  spectra were acquired by insensitive nuclei enhanced by polarization transfer (INEPT) [80,81], exploiting the scalar coupling to methylene protons,  $^3J(^{29}\text{Si}, ^1\text{H})$  3.7 Hz [82], with a spectral width of 4 kHz over 8K complex points, accumulating 512 scans with a recycle time of 16 s.

The raw data were zero filled either two or four times prior to Fourier transform (FT), and the  $^{29}\text{Si}$  ones were processed as absolute value. All the chemical shifts were referenced to tetramethylsilane (TMS). Cyclohexane, which resonates at 1.444 ppm from TMS in the  $^1\text{H}$  spectrum and at 27.69 ppm in the  $^{13}\text{C}$  spectrum, was used as internal reference for  $^1\text{H}$  and  $^{13}\text{C}$  chemical shifts.

### 2.3.2 PGSTE NMR Measurements

The  $^1\text{H}$  NMR diffusion measurements were carried out at  $25^\circ\text{C}$  on a Varian 500 NMR spectrometer (11.74 T) operating at 500 MHz for  $^1\text{H}$ , equipped with a model L650 Highland Technology pulsed field gradient amplifier (10 A) and a standard 5 mm indirect detection, pulsed field gradient (PFG) probe. A DgcsteSL\_cc: Gradient Compensated STimulated Echo with Spin Lock [77] and Convection Compensation

[78] pulse sequence was employed, with 15 different  $z$ -gradient strengths,  $G_z$ , for basic samples and 20  $G_z$ , for acidic ones, between 2 and 63 G/cm, a pulsed gradient duration,  $\delta$ , of 2 ms, and a diffusion interval,  $\Delta$ , chosen in the range 50-100 ms. The gradients were calibrated on the value of  $D = 1.90 \cdot 10^{-9} \text{ m}^2\text{s}^{-1}$  for  $^1\text{H}$  in  $\text{D}_2\text{O}$  (99.9 %) [75]. Solvent suppression was accomplished by presaturation. The lock was made on the  $\text{CDCl}_3$  of a 3 mm coaxial insert.

The data were processed by fitting the echo intensities [77] against  $q^2(\Delta - \delta/3)$  on the basis of Stejskal-Tanner equation (1.8), neglecting the nuclear relaxation term, by means of the relevant routine of the Varian VNMRJ software, version 2.2C.

The diffusion ordered spectroscopy (DOSY) [83] spectrum was processed through the Matlab Toolbox [84] after multiplication of the raw data with a Gaussian apodization function.

The best fit of the  $t$ -Bu proton signal intensities to the Poisson distribution of Equation (3.5) was carried out by means of the routine Solver of the software Excel Microsoft.

## 2.4 FT-IR Measurements

The FT-IR spectra were acquired in the range  $4000\text{-}400 \text{ cm}^{-1}$  by means of a Perkin-Elmer System 2000R spectrometer. Samples were either milled in KBr pellets (solid silica) or as thin films (the microemulsions). The latter were obtained through cyclohexane evaporation after casting a few drops of the reaction mixture onto KBr pellets.

## 2.5 UV-Vis Measurements

A Uvikon 941 plus spectrophotometer from Kontron Instruments was employed for measurement of UV-Vis spectra of  $\text{Cu}^{2+}$  and  $\text{Co}^{2+}$  doped reaction media. Cyclohexane was used as a reference standard in both cases. All spectra were recorded in the range between 300 and 850 nm.

## 2.6 Photoluminescence and Raman Measurements

The photoluminescence and Raman spectra were acquired with a InVia Raman microscope (Renishaw, Wotton-under-Edge, UK), equipped with 632.8 nm HeNe, 785 nm diode and 514.5 nm  $\text{Ar}^+$  lasers. The powder samples were placed on a microscope slide and the spectra were collected via the Raman microscope with a back scattering geometry.

## 3 RESULTS AND DISCUSSION

To shed light on the evolution of soluble species, both of the constituents of the microemulsion and of those taking part to reaction, NMR studies of the nuclei present in the system, that is  $^1\text{H}$ ,  $^{13}\text{C}$  and  $^{29}\text{Si}$ , were performed and the diffusion coefficients of the components were determined by PGSTE during the reaction, as most of the previous studies concerned only the final product. Moreover, the matter of debate is whether the ethanol, byproduct of the hydrolysis reaction, is situated in the aqueous core of inverse micelles or in oil; thus its preferred localization was investigated. First of all microemulsion itself was examined since nonionic microemulsions are not thoroughly understood, yet.

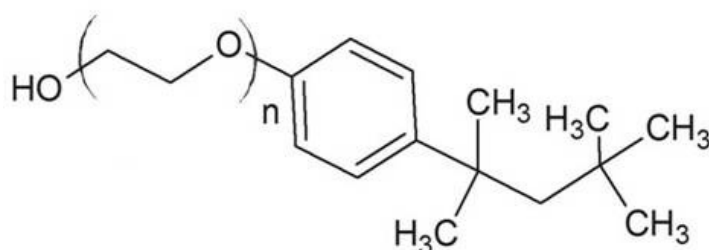
### 3.1 Basic Medium

#### 3.1.1 NMR Characterization of Microemulsions

Cyclohexane, used as organic phase in inverse microemulsion, originated just one signal both in the  $^1\text{H}$  and  $^{13}\text{C}$  spectra with either no or very scarce overlap with the signals of the other molecules of the system, therefore it was a convenient solvent for the NMR studies and it was used also as internal reference. During the  $^1\text{H}$  NMR diffusion measurements solvent suppression was required to obtain good results and cyclohexane elimination was easily accomplished by presaturation.

Igepal CA520 (5 polyoxyethylene iso-octylphenyl ether), represented in Scheme 3.1, was employed in most of the experiments, instead of Igepal CO520 (5 polyoxyethylene nonylphenyl ether), which was the surfactant chosen for this

synthetic route by most of the authors [54,57-59,85]. It was preferable from the perspective of the NMR experiments since its iso-octyl tail originated only three signals in the  $^1\text{H}$  spectrum and four in the  $^{13}\text{C}$  one, whereas the latter, due to the variable branching of the nonyl residue, gave rise to a myriad of signals of low intensity. However, the reaction was carried out in the presence of both surfactants and no differences were detected, probably because the variation of alkyl moiety of the hydrophobic tail is of minor importance and the more important head group was unchanged.

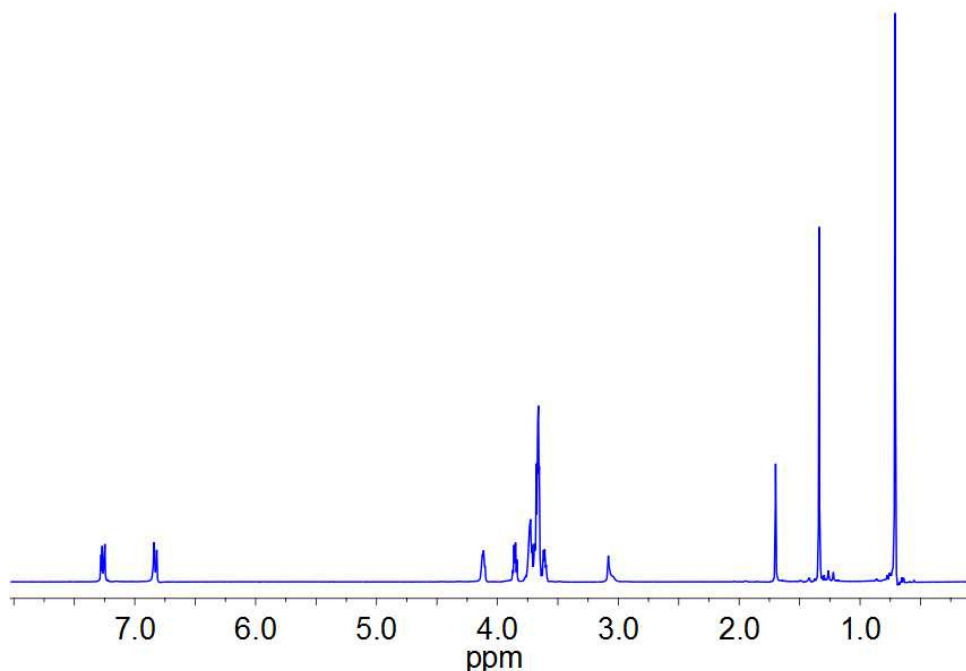


**Scheme 3.1** Schematic molecular structure of Igepal CA520, with an average  $n = 5$ .

### $^1\text{H}$ NMR

In the surfactant's  $^1\text{H}$  NMR spectrum the signals of the aromatic protons appeared at the highest frequency end of the spectrum and the protons of the tail at the lowest one, with that of the *t*-Bu methyl group being the tallest and most shielded (Figure 3.1).

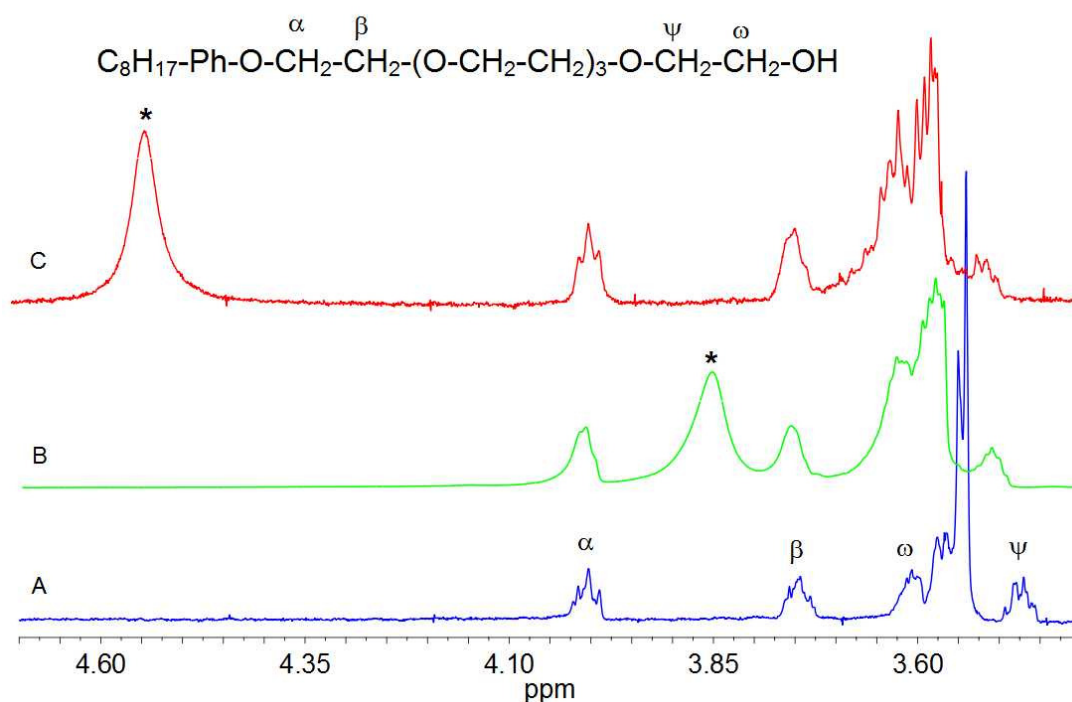




**Figure 3.1**  $^1\text{H}$  NMR spectrum of Igepal CA520 in  $\text{CDCl}_3$ .

The resonances rich in information, since highly sensitive to the phase change, were those of the polyethyleneoxide head group in the central part of the spectrum, often referred to as polyoxyethylene envelope. The spectra evolved from the solution in an organic solvent, such as cyclohexane or  $\text{CDCl}_3$ , to the microemulsion in a way that parallels the evolution due to hydration of both Triton X-100 [86] and polyethyleneoxide (PEO) alcohol surfactants [87]. The signals assignment is reported in Figure 3.2 and it was carried out by means of  $^1\text{H}$ - $^1\text{H}$  correlated spectroscopy (HH COSY) and  $^1\text{H}$ - $^{13}\text{C}$  correlated spectroscopy (HC COSY). It was further confirmed by the high sensitivity to the environment displayed by the methylene groups of the terminal ethyleneoxide (EO) unit (positions  $\psi$  and  $\omega$ ). Four  $\text{CH}_2$  protons of the head group resonated well apart from one another and from all the other “internal” methylene protons between 3.50 and 3.65 ppm, which refer neither to the first EO unit bonded to the phenyl ring nor to the terminal one, which bears the OH [86]. Furthermore, the assignment was in agreement with the one reported in literature for Triton X-100 [88], the surfactant with the same hydrocarbon tail as Igepal CA520 but

with higher ethylene oxide number (EON) as its head group contains 9-10 EO units. The commercial alkyl phenyl ethoxylated surfactants are mixtures of oligomers whose EON varies in agreement with a Poisson distribution [89]. Moreover, the EON determines the partitioning of the surfactants between oil and water in microemulsion systems.



**Figure 3.2** Region of the  $^1\text{H}$  NMR spectra corresponding to the signals of the exchangeable protons (\*) and of the surfactant head groups, with the relevant assignment, for the samples: (A) 0.1 M solution of Igepal CA520 in cyclohexane, (B) “ $\text{NH}_3$  microemulsion”, and (C) “ $\text{H}_2\text{O}$  microemulsion”.

The sensitivity of the Igepal head group was exploited to follow changes in the  $^1\text{H}$  spectra on going from a 0.1 M solution in cyclohexane to the microemulsions, obtained by adding either water or concentrated ammonia. Upon formation of the microemulsion, the signals of the polyethyleneoxide envelope, due to hydration, shifted to higher frequencies and widened the covered chemical shift range (Figure

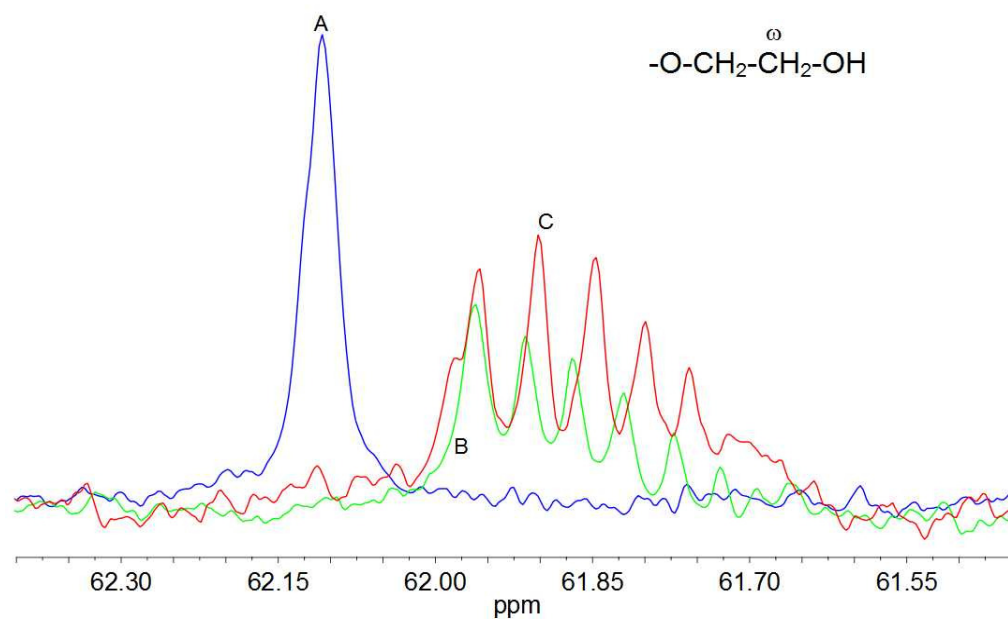
3.2 B and C). Although the volumes of the aqueous phases were equal the effect was more pronounced for water than for concentrated ammonia, probably because in the latter case the very high solute concentration affected the hydrogen bonding network of water. The signal of the  $\psi$  CH<sub>2</sub> group shifted to higher frequencies as well. Spectral changes were observed also in the alkyl region where the broadening of the tail signals was accompanied by a slight shift to lower frequencies.

A very useful <sup>1</sup>H signal for the study of the microemulsions was the broad singlet originated by the exchangeable protons of the NH and OH groups of ammonia, water, and surfactant (labeled with \* in the Figure 3.2). In the “H<sub>2</sub>O microemulsion” it resonated at 4.55 ppm, value close to the one of the bulk water (~ 4.8 ppm), indicating water pools with a well defined network of hydrogen bonds, while in the “NH<sub>3</sub> microemulsion” due to the perturbation of the network it resonated at lower frequency (3.85 ppm) and moved to higher one upon water addition.

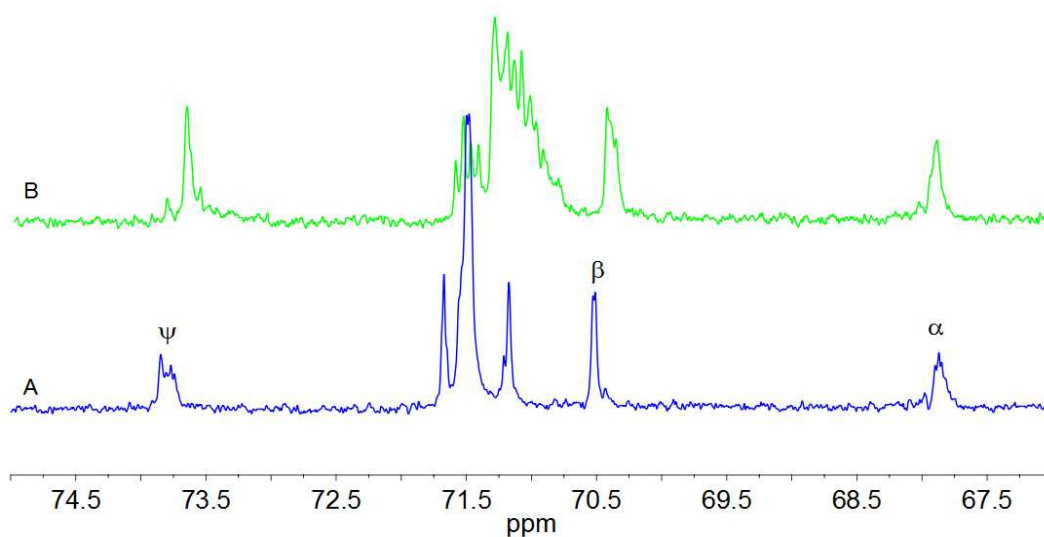
### <sup>13</sup>C NMR

The <sup>13</sup>C signals of the surfactant were assigned on the basis of the literature data concerning Triton X-100 [86,88] and polyethyleneoxide (PEO) [90] and with the help of HH and HC COSY spectra. The head group carbons assignment was further confirmed by the shifts of the relevant signals in different environments, where the highest variation was displayed by the terminal OH bearing carbon (position  $\omega$ ) since its OH group participates as a donor in hydrogen bonding with water, and the least by the  $\alpha$  and  $\beta$  nuclei, those next to the phenyl ring.

Igepal head group carbons were sensitive to the surrounding environment similarly as the corresponding protons. When aqueous phase was added to cyclohexane solution to form microemulsion, the  $\omega$  carbon, singlet resonating at 62.1 ppm, moved to lower frequencies by 0.25 ppm and split into five signals (Figure 3.3). The splitting was slightly less intense after the addition of concentrated NH<sub>3</sub> with respect to water. The higher number of signals in the <sup>13</sup>C spectra of the microemulsion systems was due to the resolution of the signals originated by the surfactant molecules having different EONs.



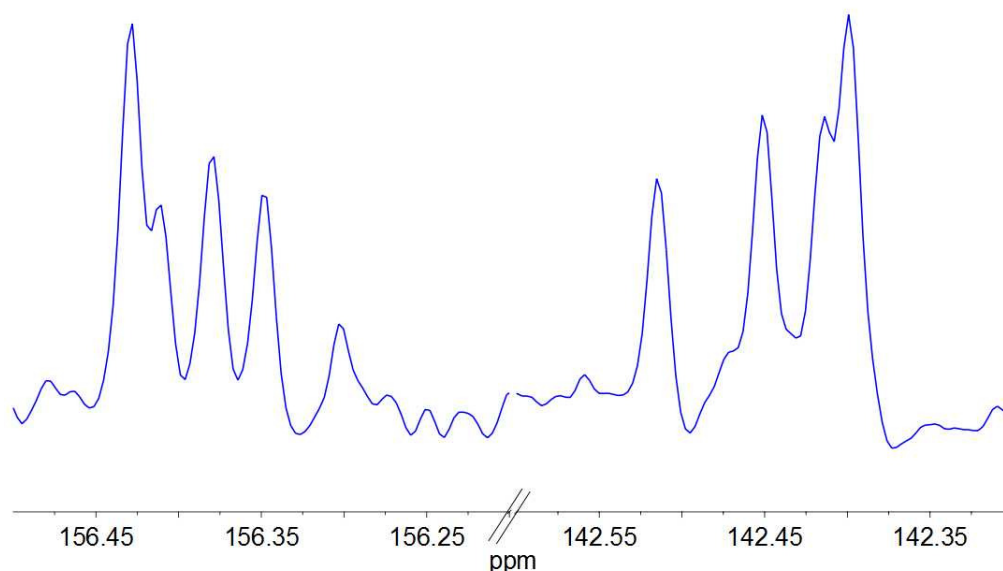
**Figure 3.3** Region of the  $^{13}\text{C}$  NMR spectrum of the signals of the  $\omega$  carbon of the Igepal head group: A) 0.1 M solution of Igepal CA520 in cyclohexane, B) “ $\text{NH}_3$  microemulsion” and C) “ $\text{H}_2\text{O}$  microemulsion”.



**Figure 3.4** Region of the  $^{13}\text{C}$  NMR spectrum of the signals of the Igepal head group carbons: A) 0.1 M solution of Igepal CA520 in cyclohexane and B) “ $\text{NH}_3$  microemulsion”.)

An analogue behavior was shown by the most of the carbons of the polyoxyethylene envelope between 72.0 and 71.0 ppm. The  $\alpha$ ,  $\beta$  and  $\psi$  head group carbons and *t*-Bu carbons of the tail shifted slightly to higher frequency, by about 0.07 ppm (Figure 3.4).

On the other hand, in  $\text{CDCl}_3$  solution, the electronic effect of the PEO chain length was appreciable, at the operating fields of 9.4 T, only for the carbons of the phenyl ring in position 1, i.e. the one bearing the polyethyleneoxide chain, and 4, in *para* to the former (Figure 3.5), and the shift differences were very small, in the order of a few hundredths ppm.



**Figure 3.5**  $^{13}\text{C}$  NMR signals of the aromatic quaternary carbons of Igepal CA520 in  $\text{CDCl}_3$ .

The water was able to resolve the NMR signals of the surfactant's oligomers. The spectral changes that were due to the phase transition (solution-microemulsion) induced by water addition must be related to the water-PEO interaction since it has been proposed that the hydration and the average conformational state strongly depend on each other [91,92]. PEO is a very flexible polymer with a high degree of internal motion in solution [90], as shown by several NMR and Raman spectroscopic

studies. The probability of finding the two CH<sub>2</sub> groups of the same EO unit in *gauche* conformation is rather high in water, even for the very short PEO chains [93]. For longer ones the helical arrangement of the solid state is retained partially [94,95] where the 7/2 helix consists of a *trans-gauche-trans* sequence for each O-C-C-O repetitive unit. Helical conformation of the head groups for micelles of Triton X-100 in water is favored by packing requirements at the micellar surface, and these regulate also the penetration of water molecules between the head groups. When surfactant is present as monomeric specie in water the PEO chains are more elongated [96].

The small changes in <sup>1</sup>H and <sup>13</sup>C spectra of the surfactant occurring during the hydrolysis reaction corresponded to shifts of the opposite sign with respect to those induced by the formation of the microemulsion. This was probably due to the consumption of water, which decreased the hydration of the surfactant head group.

### PGSTE NMR

The diffusion coefficients for the surfactant, reported in Table 3.1, in the “H<sub>2</sub>O” and “NH<sub>3</sub> microemulsion” were obtained from the signal of the *t*-Bu protons that resonated at 0.71 ppm (Figure 3.1) which, being the most intense, was the most reliable one. The values of the aromatic signals, together with those of the α, β, ψ and ω protons, were in agreement. The measured diffusion coefficients of Igepal in “H<sub>2</sub>O” and “NH<sub>3</sub> microemulsion” are  $2.11 \cdot 10^{-10} \text{ m}^2 \text{ s}^{-1}$  and  $2.40 \cdot 10^{-10} \text{ m}^2 \text{ s}^{-1}$ , respectively. The exchange of the surfactant molecules between the oil, where they are present as unimeric species, and the micellar interface was fast on the NMR time-scale; consequently value of any NMR observable was the weighted average of the values in the two sites. This can be rationalized in terms of the two-site approach, commonly employed in the case of surfactant molecules in micellar self-assemblies.

The diffusion coefficient of the exchangeable –NH and –OH protons signal in the “NH<sub>3</sub> microemulsion”, used later on as the reaction medium,  $3.34 \cdot 10^{-10} \text{ m}^2 \text{ s}^{-1}$ , was much higher than for the same signal in “H<sub>2</sub>O microemulsion”,  $0.97 \cdot 10^{-10} \text{ m}^2 \text{ s}^{-1}$ . This was rationalized by the intermicellar diffusion of NH<sub>3</sub> through the bulk oil, in line with

its not negligible oil solubility. The diffusion coefficient of the surfactant did not change as dramatically; therefore the transition to a bicontinuous system was excluded.

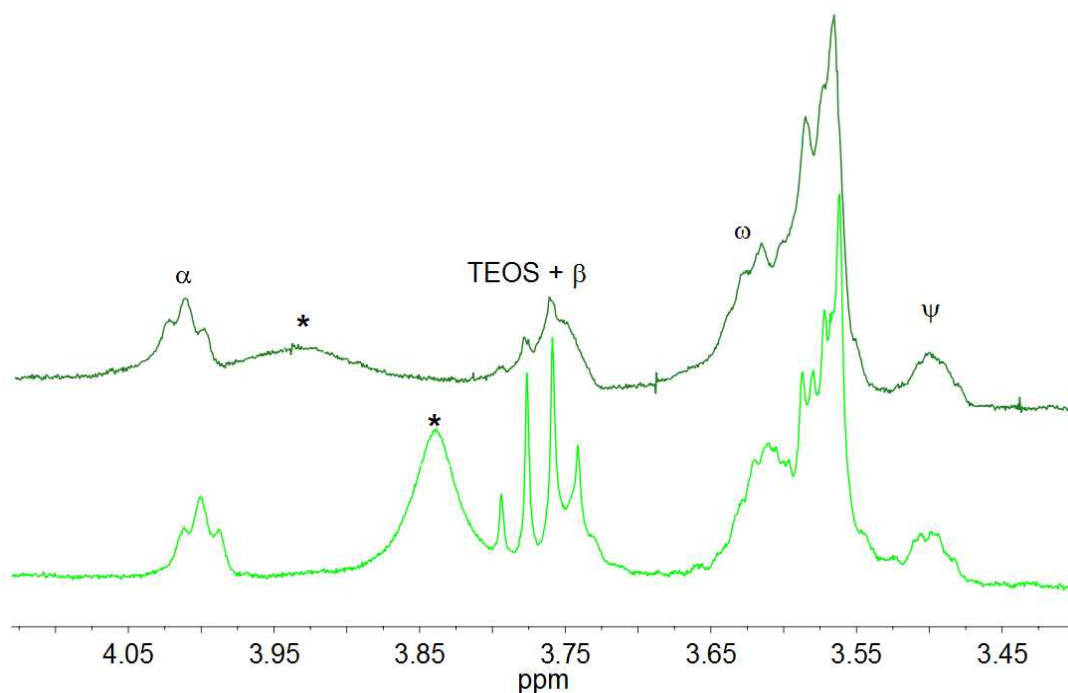
Diffusion coefficients are commonly exploited to characterize microemulsions, for example, to determine the connectivity of the phase and the size of water droplets. [73,97] The results provided an insight into the compartmentalization caused by the inverse micelles. The diffusion coefficient of exchangeable protons in the “H<sub>2</sub>O microemulsion” was approximated as the diffusion coefficient of the inverse micelles since that of the “NH<sub>3</sub> microemulsion” was affected by the diffusion of NH<sub>3</sub> molecules in the oil. Its value, lower than the surfactant’s one ( $2.11 \cdot 10^{-10} \text{ m}^2 \text{ s}^{-1}$ ), indicated that there was lots of surfactant dissolved in the bulk oil, which may act as a surfactant’s reservoir. The discrete micellar size [54] was further confirmed by calculation of the hydrodynamic diameter ( $d_h$ ) of inverse micelles employing the Stokes-Einstein relation (Equation 1.1) where  $\eta$  is the cyclohexane viscosity constant, 0.9 mPa s [98] and D is diffusion coefficient of micelles. The hydrodynamic diameter thus obtained was about 5 nm which is in line with SAXS findings in the same system [85].

### 3.1.2 NMR Characterization of Reaction Medium

#### <sup>1</sup>H NMR

The <sup>1</sup>H singlet originated by the exchangeable protons of the NH and OH groups of ammonia, water, surfactant and EtOH (Figure 3.6) was very useful to follow the proceeding of the hydrolysis reaction. The signal broadened remarkably already at early reaction times, and since its integrated intensity should not change because the protons of the water molecules consumed by the overall reaction were returned as EtOH alcoholic protons, the broadening was accompanied by a fast height decrease. In fact, EtOH protons provoked the broadening since they did not contribute to any extended hydrogen bonding network as EtOH was mainly dissolved in the cyclohexane. The broadening of the signal of the head group  $\psi$  protons also

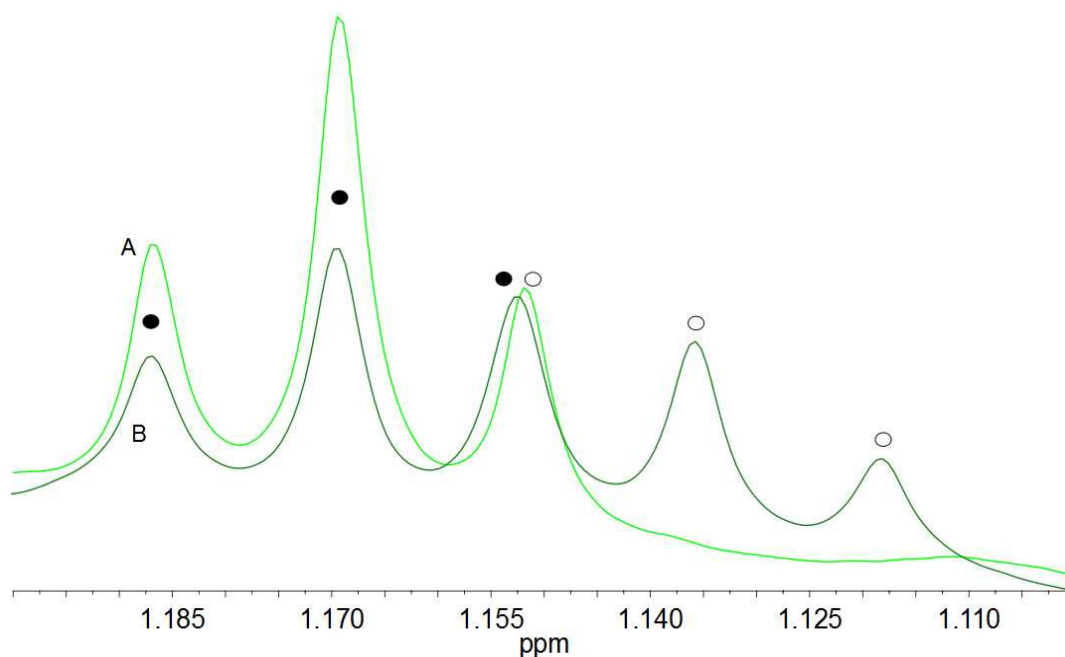
occurred, and it was the only change of the surfactant signals observed during the reaction advancement.



**Figure 3.6** Region of the  $^1\text{H}$  NMR spectra corresponding to the signals of the exchangeable protons (\*) and of the surfactant head group protons for the samples: reaction mixture (A) 0.5 h and (B) 37 h after the reaction beginning.

The protons of TEOS methylene groups were partially overlapped to the  $\beta$   $\text{CH}_2$  signal of the surfactant head group (Figure 3.6), while the quartet of the  $\text{CH}_2$  of the byproduct EtOH was completely buried in the broad polyoxyethylene envelope. The triplets of the methyl groups of both TEOS and EtOH appeared at lower frequencies than the cyclohexane signal, at about 1.17 and 1.14 ppm, respectively, and were exploited to follow the hydrolysis reaction advancement (Figure 3.7).



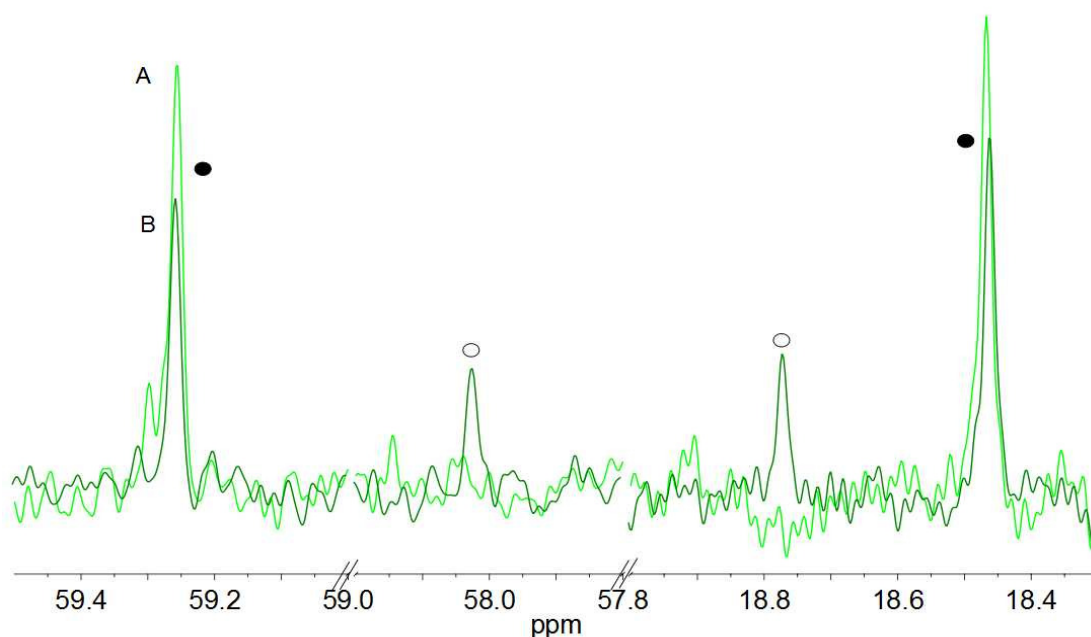


**Figure 3.7**  $^1\text{H}$  NMR signals of the methyl groups of TEOS (at higher frequency, ●) and EtOH (at lower frequency, ○) from the reaction mixture: (A) 0.5 h and (B) 25 h after the reaction beginning.

No different signals from those of TEOS, EtOH and of the components of the microemulsion were detected. Consequently, the absence of intermediate species containing organic residues was assessed.

### $^{13}\text{C}$ NMR

In the  $^{13}\text{C}$  NMR spectrum the  $\text{CH}_2$  carbons of TEOS and EtOH resonated at 59.27 and 57.95 ppm and  $\text{CH}_3$  carbons at 18.45 and 18.78 ppm, respectively (Figure 3.8). The resonances appeared well apart from each other and also from all the other signals, therefore could be exploited efficiently in the kinetic study.



**Figure 3.8**  $^{13}\text{C}$  NMR signals of the methylene (at higher frequency) and methyl (at lower frequency) carbons of TEOS (●) and EtOH (○) from the reaction mixture: (A) 0.5 h and (B) 25 h after the reaction beginning.

### $^{29}\text{Si}$ NMR

$^{29}\text{Si}$  NMR spectroscopy was used in order to distinguish amongst different silicon species, usually present as reaction intermediates in the sol-gel process [23,40,99]. To oppose to the very low TEOS concentration, 0.04 M, the spectra were acquired through INEPT which is efficient technique to artificially increase the signal intensity by polarization transfer from protons to the coupled heteroatoms, especially in the case of nuclei, like  $^{29}\text{Si}$ , with negative gyromagnetic ratio. The spectra, accumulated for about 2 hours to allow the perception of the TEOS consumption kinetics, displayed only the TEOS signal, decreasing in time as it gets hydrolyzed. Moreover, also directly detected  $^{29}\text{Si}$  NMR spectrum in the presence of  $\text{Cr}(\text{acac})_3$ , as relaxation agent, was run in the attempt to reveal soluble intermediate species. The

spectra showed, in addition to that of TEOS, only the broader signal due to the glass of the NMR tube and of the probe-head [58]. Yet the  $^{29}\text{Si}$  NMR spectroscopy greatly contributed to the understanding of the Stöber synthesis [32], where much higher concentrations of the starting tetraalkyl orthosilicate were used. The monohydrolyzed monomer was detected as the most abundant reaction intermediate with the signal of the  $\text{CH}_2$  carbon detected at + 0.4 ppm with respect to that of TEOS [32]. In our system partially hydrolyzed TEOS was observed neither in the  $^{29}\text{Si}$  nor in the  $^1\text{H}$  and  $^{13}\text{C}$  NMR spectra.

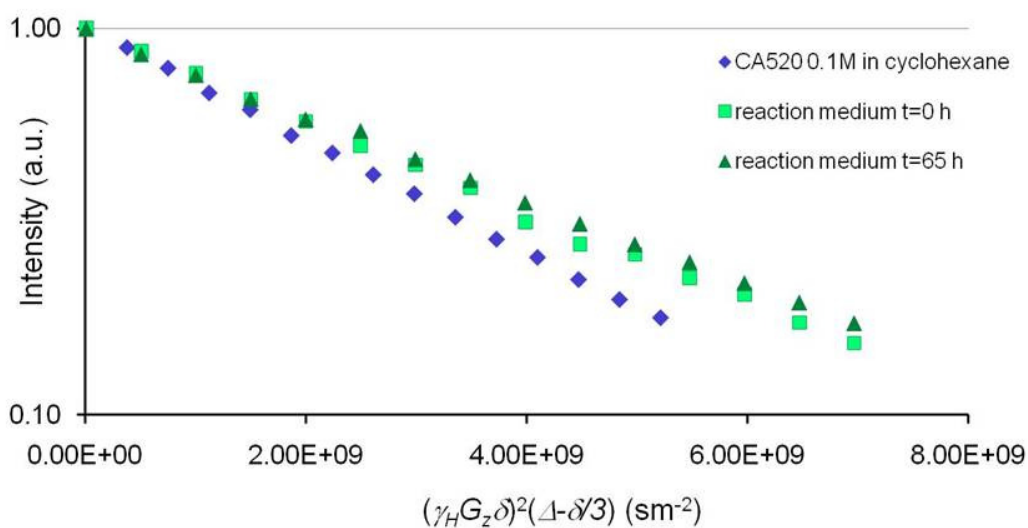
### *PGSTE NMR*

The diffusion coefficient values in the reaction medium were determined for the surfactant, TEOS, EtOH and the exchangeable protons, at the reaction beginning and 65 h afterwards (Table 3.1). The echo intensities were fitted against the gradients strength (Figure 3.9), at constant diffusion delay, on the basis of Stejskal-Tanner equation (1.8) neglecting the nuclear relaxation term, for all the samples reported in Table 3.1. The echo decays did not show any deviation from a unique exponential curve (Figure 3.9) indicating that the values are an average of the different situations experienced by the relevant molecules, i.e., in the reaction medium the surfactant exchanged among three sites: the bulk oil, the surface of the reverse micelles and the surface of silica nanoparticles. The residence time in each environment was much shorter than the diffusion interval,  $\Delta$ . A multiexponential echo decay was found in the Igepal CA520/*n*-heptane/water ternary system [64] which is highly concentrated and in which the surfactant molecules are mostly at the interface. In that system the residence time of Igepal at the interface, where it diffused slowly, had to be longer than diffusion interval in order to observe multiexponential decay, without the fast exchange with Igepal in oil, where the diffusion was fast.

**Table 3.1** Diffusion coefficients reported in  $10^{-10} \text{ m}^2 \text{ s}^{-1}$  plus/minus the standard error from the fitting process and measured at 25 °C.

Sample	Igepal <i>t</i> -Bu	Exchangeable protons	TEOS	EtOH
0.1 M Igepal in cyclohexane <sup>a</sup>	$3.38 \pm 0.02$			
“H <sub>2</sub> O microemulsion” <sup>a</sup>	$2.11 \pm 0.02$	$0.97 \pm 0.01$		
reaction medium at <i>t</i> = 0 h <sup>b</sup>	$2.40 \pm 0.02$	$3.34 \pm 0.01$	$7.7 \pm 0.1$	
reaction medium at <i>t</i> = 65 h <sup>b</sup>	$2.57 \pm 0.02$		$8.3 \pm 0.1$	$8.87 \pm 0.07$
EtOH in cyclohexane at 20 °C <sup>c</sup>				$9.36 \pm 0.04$

a)  $\Delta = 100 \text{ ms}$ . b)  $\Delta = 75 \text{ ms}$ . c) Reference [98].



**Figure 3.9** Plot of the echo decays for Igepal CA520 *t*-Bu signal (log scale) for the 0.1 M solution of Igepal in cyclohexane and the reaction medium at *t*= 0 and *t*= 65 h.

The diffusion coefficients for TEOS and EtOH were obtained from the decays of the middle signal of the CH<sub>3</sub> triplets, and the other two signals confirmed the values. The CH<sub>2</sub> protons could not be employed due to the overlap with the signals of the surfactant's head group. The diffusion coefficient for the signal of the exchangeable protons is reported only for the "H<sub>2</sub>O microemulsion" and the starting reaction medium while for the latter sample analyzed 65 h after TEOS addition its determination was hampered by the severe broadening of the signal which led to a partial overlap with the proton signals of the first EO unit. The time (65 h) was chosen in order to have a significant presence of silica nanoparticles which should have water molecules adsorbed on the surface, and therefore should influence their diffusion. These water molecules adsorbed on the silica nanoparticles' surface are necessary to keep them in solution [8].

The diffusion coefficient value of the surfactant did not provide detailed information about the formation and growth of the silica nanoparticles since it had increased only slightly 65 h after the reaction beginning, i.e. in an advanced stage. The surfactant's diffusion should be hampered by nanoparticles, greater in size than the inverse micelles, not only by binding, but by acting as obstacles. Yet, their effect was negligible because they were by far less numerous than the inverse micelles [58]. It must be recalled that the surfactant is in the fast exchange between various sites and that its diffusion coefficient is a mean value. One of the sites is the nanoparticles' surface, where it provides their steric stabilization and blocks incoming reacting species, contemporarily keeping the particles in solution.

The diffusion coefficient of EtOH,  $8.87 \cdot 10^{-10} \text{ m}^2 \text{ s}^{-1}$ , higher than the surfactant's, indicated that the partitioning of the reaction byproduct between the water pool and the oil, occurred with preference for the latter, as previously suggested by Riello *et al.* [85], and it is in agreement with the localization of the alcohol determined in a cyclohexane-AOT-water inverse microemulsion, always by means of PGSE-NMR [98]. An estimation of EtOH partitioning between the two environments was done using the measured diffusion coefficient ( $D_{\text{obs}}$ ) considering fast exchange of EtOH among the various situations during the diffusion interval. The molar fraction of EtOH in the aqueous phase ( $X_{\text{mic}}$ ) was calculated according to Equation (3.1):

$$X_{mic} = \frac{D_{oil} - D_{obs}}{D_{oil} - D_{mic}} \quad (3.1)$$

where  $D_{oil}$  is the diffusion coefficient for EtOH in cyclohexane [98] and  $D_{mic}$  is approximated by the value of the diffusion coefficient of the exchangeable proton in the “H<sub>2</sub>O microemulsion”. An  $X_{mic}$  value of 0.06 was obtained, recalling the maximum possible value of 1 ( $X_{mic} + X_{oil} = 1$ ). Conversely, calculating  $X_{mic}$  by means of the partition equilibrium constant ( $K_c$ ) and employing as  $V_{oil}$  and  $V_{water}$  the volumes of cyclohexane and NH<sub>3</sub> solution, respectively, according to Equation (3.2):

$$K_c = \left( \frac{X_{mic}}{1 - X_{mic}} \right) \left( \frac{V_{oil}}{V_{water}} \right) \quad (3.2)$$

a value of  $X_{mic} = 0.10$  was obtained. It was in good agreement with the previous one, considering the coarse approximations. Moreover,  $K_c$  may depend significantly on the surfactant and, above all, on the composition of the aqueous phase. The  $K_c$  used for the present calculation is the value reported in literature for the partitioning of ethanol in AOT/water/cyclohexane system, measured at 20 °C [98].

### 3.1.3 Hydrolysis

The highly sensitive <sup>1</sup>H nucleus was the best suited to follow TEOS hydrolysis allowing the immediate detection, even of small amounts, of proton containing species. The protons of the methylene groups of TEOS were partially overlapped with the β CH<sub>2</sub> signal of the surfactant head group, while the quartet of the methylene of the produced EtOH was completely buried in the polyethyleneoxide envelope (Figure 3.6), and therefore not useful to follow the kinetics. On the other hand, the triplets of the methyl groups of both TEOS and EtOH appeared at lower frequencies, at about 1.17 and 1.14 ppm (Figure 3.7), respectively, and were convenient for the quantitative study of the reaction advancement.

In the  $^{13}\text{C}$  NMR spectrum, the  $\text{CH}_2$  and  $\text{CH}_3$  carbons of both TEOS and EtOH resonated well apart from each other (Figure 3.8) and were not overlapped with other signal; therefore, each of them could be exploited efficiently.

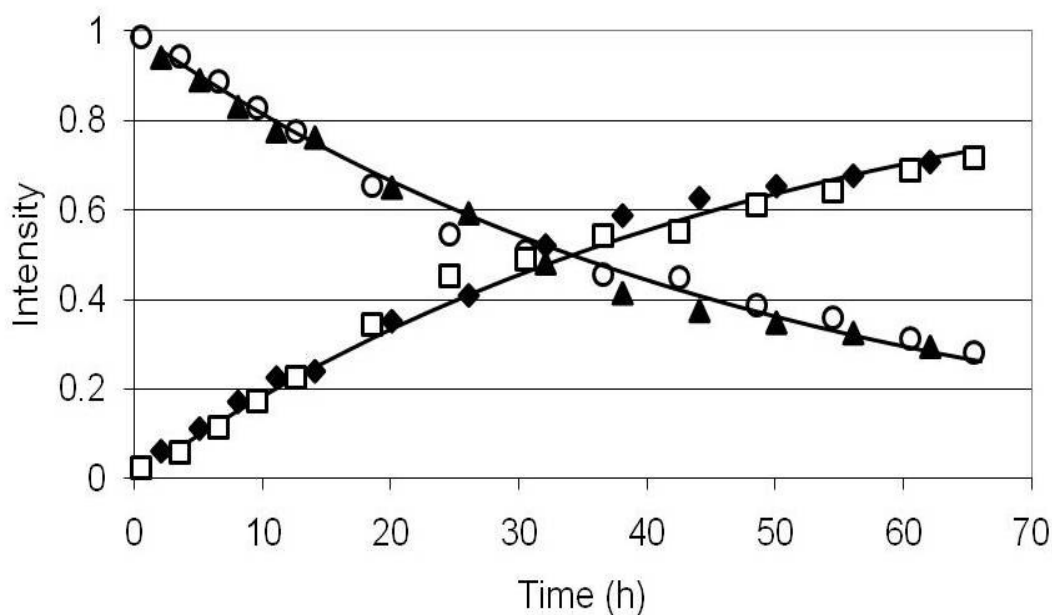
The trend of TEOS methyl  $^1\text{H}$  signal intensities versus time was nicely fitted according to the exponential decay of the first order kinetic (Equation (3.3)) with respect to TEOS concentration (Figure 3.10) [53,54]:

$$\frac{d[\text{TEOS}]}{dt} = -k[\text{TEOS}][\text{OH}^-] \quad (3.3)$$

The spectra of both  $^1\text{H}$  and  $^{13}\text{C}$  were recorded in time intervals of 3 hours and the value of hydrolysis constant so obtained was  $k_h = k[\text{OH}^-] = 0.024 \text{ h}^{-1}$  [100]; it is an average value of two independent measurements. The value is in agreement with the constants reported in literature for TEOS hydrolysis in microemulsion, obtained by IR spectroscopy [53,54], and for the overall process of  $\text{SiO}_2$  production, determined by SAXS [85]. Since the rates of TEOS hydrolysis and of nanoparticles formation had almost the same constants it was concluded that the particles' growth is controlled by hydrolysis of TEOS, which is therefore the rate determining step. The hydrolysis constant was further confirmed by the good fit of the trend of the EtOH signal intensities according to Equation (3.4), deduced from Equation (3.3) and from the stoichiometry of the reaction:

$$[\text{EtOH}(t)] = 4[\text{TEOS}(t=0)]\{1 - \exp(-k_h t)\} \quad (3.4)$$

The intensities of the  $^{13}\text{C}$  signals of TEOS and EtOH were in line with the corresponding  $^1\text{H}$  data (Figure 3.10).



**Figure 3.10** Intensities versus reaction time of the  $^1\text{H}$  TEOS ( $\circ$ ) and EtOH ( $\square$ ) methyl signals and  $^{13}\text{C}$  TEOS ( $\blacktriangle$ ) and EtOH ( $\blacklozenge$ ) methylene signals. The black lines are the fitting of the intensities of  $^1\text{H}$  methyl signals carried out by means of Eq (3.3) for TEOS and Eq (3.4) for EtOH.

It is evident from Figure 3.10 that the TEOS concentration declined while the EtOH concentration increased exponentially.

The intensities of the  $^{29}\text{Si}$  signals were not suitable for an exhaustive kinetic study due to the poor signal-to-noise ratio; conversely  $^{29}\text{Si}$  NMR spectroscopy was able to provide detailed information about the microscopic dynamics of the Stöber synthesis, performed at a much higher concentration of the silicon precursor.

The modified Stöber reaction, where a system was initially subjected to an acid treatment so that variously hydrolyzed monomers and dimers were present before addition of  $\text{NH}_3$ , elucidated that [40]:

- (i) the nucleation rate is limited by the hydrolysis of the singly hydrolyzed monomer;
- (ii) the first nucleus is the doubly hydrolyzed product, and it phase separates;



(iii) the best suited aggregation model seems the one that postulates that the particle size is governed by the competition between the processes of nucleation and aggregation.

The number of particles increases with time being the nucleation continuous during the course of reaction [32], and the particle size increases with water concentration in the presence of electrolyte, the latter favoring higher aggregation rates [40].

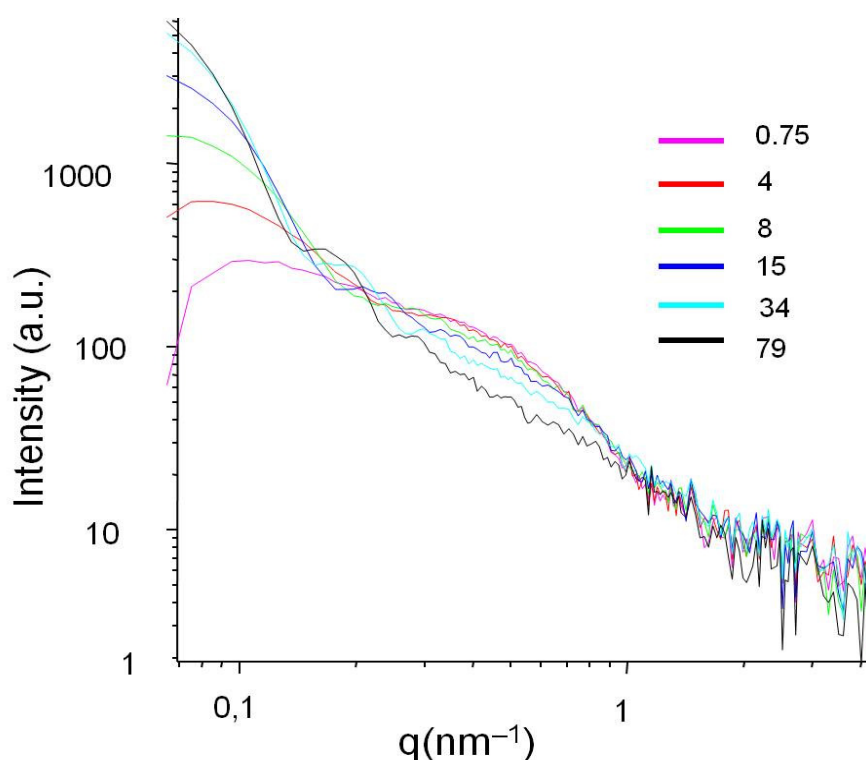
These results must be transferred to microemulsion systems with great caution as the confinement of the inverse micelles affects both the nature of the intermediates species and kinetics of the intermediate steps (condensation and growth). They can be intra- and/or inter-micellar and depend mainly on: the water-to-surfactant molar ratio,  $R$ , and  $\text{NH}_3$  concentration. By increasing both of them the stability boundary of the microemulsion is approached and the intermicellar exchange becomes easier. However, at low  $R$ , the TEOS hydrolysis is slow due to the small amount of free water, so fewer nuclei are formed, and consequently, larger particles are produced [58,59].

### 3.1.4 Characterization of the Product

#### SAXS

The growth of the particles was easily followed by small angle X-ray scattering (SAXS) and the spectrum of the system as a function of time (log-log scale) is shown in Figure 3.11 [85]. Two interesting features were observed:

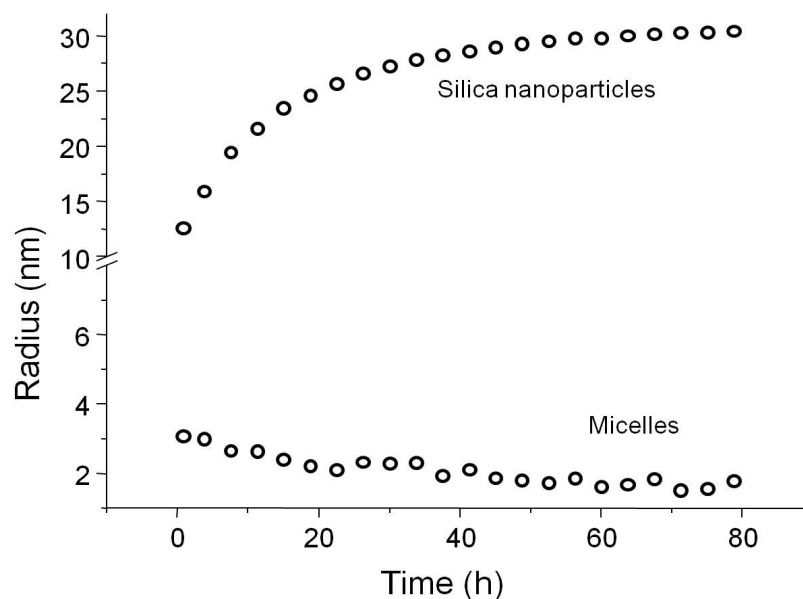
- (i) the change in shape of the scattering profile, and
- (ii) an increase in the intensity, especially at low values of scattering vector modulus ( $q$ ).



**Figure 3.11** *In situ* time-resolved SAXS measurements of the scattering intensity of the reaction medium; the intensity profiles are labeled according to reaction time (hours) [85].

At low  $q$  a difference in the scattering patterns was observed whereas at high  $q$  the intensity plots were overlapped indicating that at the low  $q$  the signal can be related to the evolution of the silica in the system, while at high  $q$  the empty micelles contribute to scattering. Already an hour after the beginning of the reaction silica with high density of cross-linking was observed.

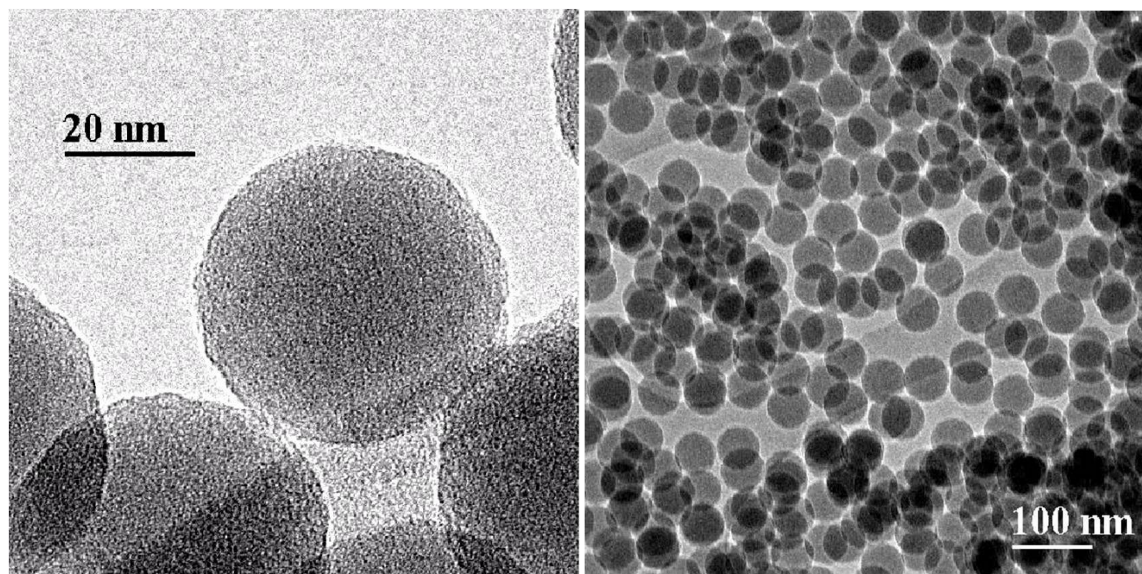
The kinetic of nucleation and growth was of the first order with respect to TEOS, as confirmed by the plot of the volume fraction vs. time data. The average radii of silica nanoparticles and of the empty micelles were obtained through the fitting procedure of the SAXS data. From Figure 3.12 [85] it can be seen how the growth of the silica nanoparticles was initially fast, then decreased and afterwards it was almost time independent. The reduction of micellar radius was due to the consumption of water during the hydrolysis reaction and the SAXS intensity of this smaller micellar system indicated the characteristic radius of about 2 nm.



**Figure 3.12** Growth of the radius of the silica nanoparticles and of the empty micelles as a function of time [85].

### TEM Analysis

Size and morphology of the silica particles were measured using a transmission electron microscope (TEM). The particles obtained in the reaction medium, with an  $R$  value chosen near the minimum of the curve of the particle size, are shown in TEM micrographs in Figure 3.13. The final product were small particles with a diameter of about 40 nm, in line with the results reported in the literature for synthesis carried out in an Igepal CO520/concentrated ammonia/cyclohexane solution with a comparable  $R$  [58]. Their uniformity suggested that the events of nucleation and growth are well separated in time for this microemulsion composition. Actually, SAXS studies confirmed that nucleation takes place during a limited period of time; in fact, the number density of the particles became constant after the first 10 h [85].



**Figure 3.13** TEM micrographs of the SiO<sub>2</sub> nanoparticles.

### 3.2 Acidic Medium

The inverse micelles have been used for the production of silica nanoparticles for some time but the mechanism for their formation has been investigated only for the base-catalyzed hydrolysis of TEOS. At the state of the art only few studies about the application of the inverse micelles for the acid-catalyzed synthesis of silica nanoparticles are reported and only one applies to the entire synthesis carried out in inverse microemulsion where the aqueous core remains stable throughout the reaction. In the Igepal CO520/HNO<sub>3</sub> 0.1M/cyclohexane system particles with the radius of 2.6 nm were obtained, and NaF was added to the aqueous core in order to catalyze hydrolysis and condensation steps [8]. The authors used TMOS, instead of TEOS, as silicon precursor, but it is less preferable due to more complicated synthetic route, since it is instable to air.

The nonionic inverse microemulsions, prepared with an acidic aqueous phase and subsequently used as a reaction medium in the present thesis work, were characterized by means of  $^1\text{H}$  and  $^{13}\text{C}$  NMR spectroscopy, SAXS and the diffusion coefficients were measured by PGSTE NMR.  $^{29}\text{Si}$  NMR spectra were not recorded since did not provide new insights of the reaction advancement in the basic microemulsion. The assignments of the NMR signals were made on the basis of literature data for Triton X-100 [86,88] and previous findings in basic medium [100]. The final product was characterized by TEM and IR and compared with the classical HCl-catalyzed sol-gel silica [44] by thermogravimetric analysis (TGA) and differential scanning calorimetry (DSC).

### 3.2.1 NMR Characterization of Microemulsions

#### *Stability of the Acidic Microemulsions*

Various ratios of acetic acid and water were used in order to find the best suited one, and different water-to-surfactant molar ratios were examined, maintaining constant the surfactant's concentration, so to produce the microemulsion. The rare compositions that provided a stable microemulsion resulted not suited for the synthesis of silica nanoparticles as the reaction did not proceed, probably because the acetic acid has preference for the organic phase while the micellar core contains mostly the water molecules.

Conversely, the mineral acids, hydrochloric and nitric, gave good results. First, the system analogous to that in basic medium ( $R= 4.4$ ,  $h= 11$ ) [100] was prepared using  $\text{HNO}_3$  0.1 M but the hydrolysis resulted very slow. Most of the water present in the pools was shell water, the one that provides the surfactant hydration while the core water responsible for the hydrolysis was not enough to ensure the efficient reaction. This confirms that the mechanism of acid-catalyzed hydrolysis is the same as in bulk solution, i.e. the rate determining step is water attack to a protonated

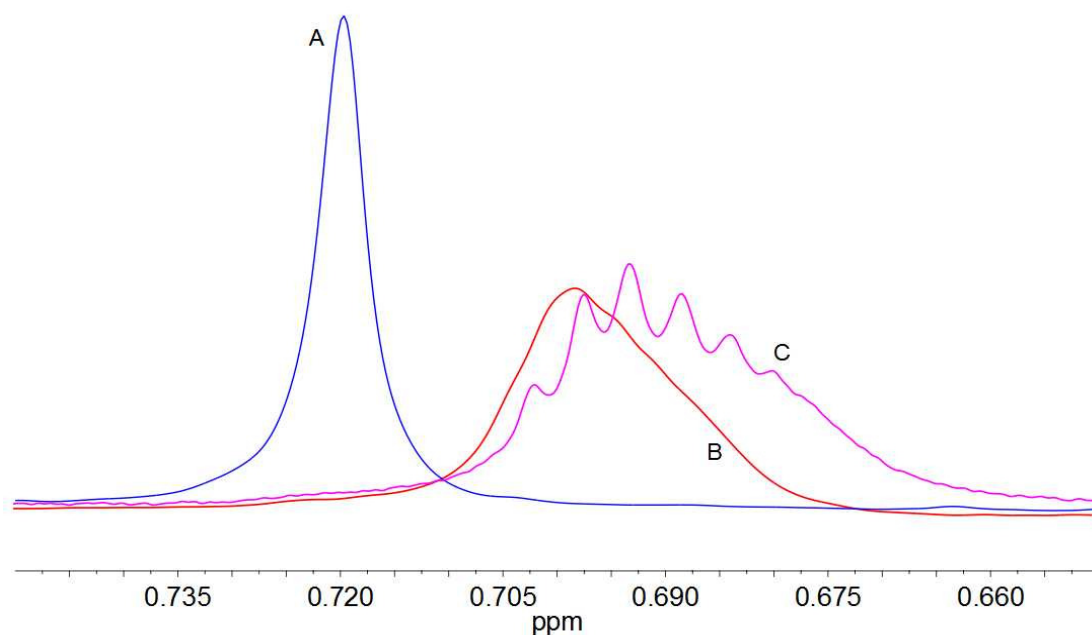
alkoxide. We have, therefore, increased the volume of the aqueous phase to obtain  $R= 5.7$  in order to have rates of TEOS hydrolysis comparable to the “NH<sub>3</sub> microemulsion”. The concentration of TEOS was also increased to obtain  $h= 5.2$ . The analogue system was prepared with the HCl 0.1 M as internal phase. The drawback of the employed microemulsions was the poor stability at higher water and TEOS concentrations. In the case of the latter, the problem arose some time after the beginning of the reaction since it was due to the destabilizing effect of the byproduct ethanol, which partitioned in higher amount in the micellar core with respect to the basic microemulsion. Indeed, at the water-to-TEOS molar ratio used the alkoxide hydrolysis was slow; nevertheless, the polymerization step remained the rate-determining one like in bulk synthesis catalyzed by acid.

The decrease of the acid concentration slowed down the rate of hydrolysis which was directly proportional to the acid concentration used [101]. Slower hydrolysis might favor the condensation so we prepared systems with HNO<sub>3</sub> 0.05 M and HCl 0.05 M as internal phase. Moreover, the addition of fluoride, as catalyst, to the internal phase of all the samples in the concentration of 0.038 M [8] was considered since it is reported that traces of F<sup>-</sup> have an outstanding catalytic effect on the polymerization rate in silica sol-gel systems [82]. The samples studied herein are summarized in Table 3.4 where reported together with the relevant hydrolysis constant,  $k_h$ , values.

### <sup>1</sup>H NMR

The <sup>1</sup>H NMR spectrum of Igepal revealed some subtle changes with respect to that of an analogous system using water as the internal aqueous phase [100]. A small variation for the envelope of the signals arising from the inner EO protons was observed. Noteworthy was the multiplicity displayed by the *t*-Bu protons of the tail, the signal of which had passed from singlet in cyclohexane solution, basic and neutral medium to multiplet in acidic one (Figure 3.14). This originated from the higher resolution of different EO oligomers present in the head group of the commercial surfactant and it was deepened with the PGSTE NMR [102].

However, neither the specific acid nature ( $\text{HNO}_3$  or  $\text{HCl}$ ), its concentration (0.1 or 0.05 M), nor the eventual addition of NaF significantly affected the  $^1\text{H}$  spectrum of the surfactant.

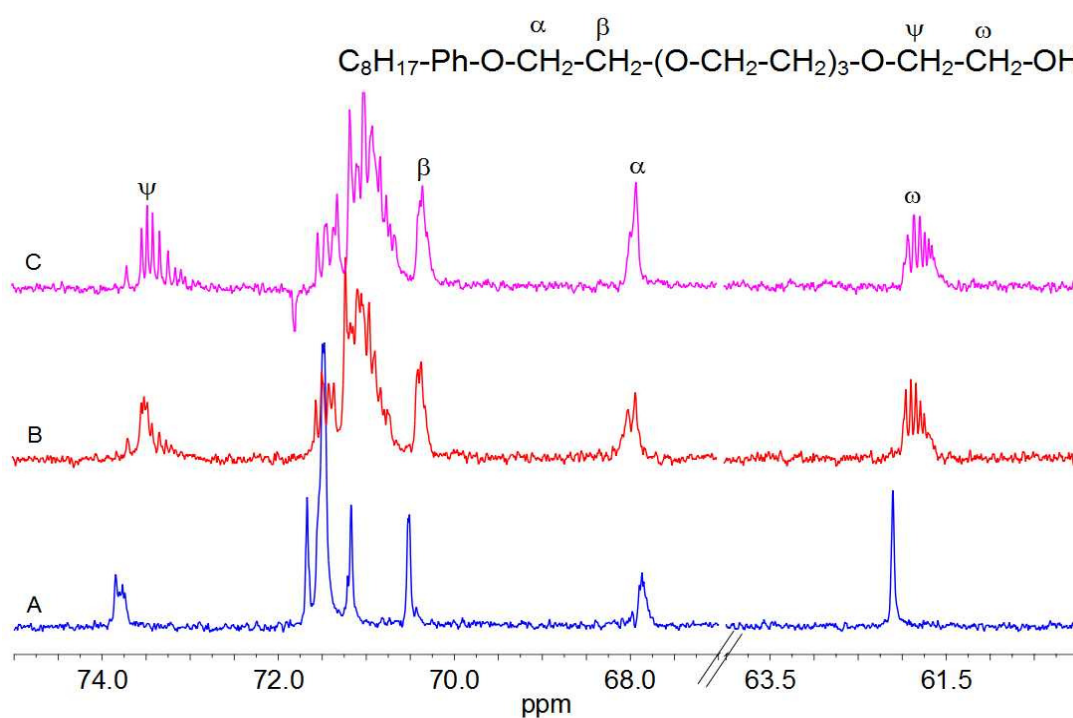


**Figure 3.14**  $^1\text{H}$  NMR signal of the surfactant's *t*-Bu group for samples: (A) Igepal CA520 0.1 M solution in cyclohexane, (B) “ $\text{H}_2\text{O}$  microemulsion” and (C) “ $\text{HNO}_3$  0.1 M + NaF microemulsion”.

Information on the microstructure of the aqueous core in the inverse micelles was given by the NMR signal of the exchangeable protons, that is, those of the Igepal terminal OH group, of water and of acid since the chemical shift of the nuclei engaged in hydrogen bonds varied even when the environment changed only slightly. The hydrogen bond network of the water pools was perturbed by the addition of NaF so a small shift to a lower frequency was observed on its addition.

$^{13}\text{C}$  NMR

The  $^{13}\text{C}$  NMR spectrum of hydrophobic moiety of Igepal in the acidic microemulsions did not differ from that of the “ $\text{NH}_3$ ” and “ $\text{H}_2\text{O}$  microemulsions”, whereas the signals of the hydrophilic head group originating from oligomers with different EONs displayed an enhanced separation, also noticeable for  $\text{C}\psi$  (Figure 3.15). Furthermore, most  $^{13}\text{C}$  nuclei of the surfactant head group experienced a minor shift to a lower frequency. No alteration of the spectral pattern was observed by changing the strength of the acid, its nature and adding NaF thus suggesting that Igepal did not partake in the specific anion effect.



**Figure 3.15** Head group region of the  $^{13}\text{C}$  NMR spectra for samples: A) 0.1 M solution of Igepal CA520 in cyclohexane, (B) “ $\text{H}_2\text{O}$  microemulsion” and (C) “ $\text{HNO}_3$  0.1 M microemulsion”.

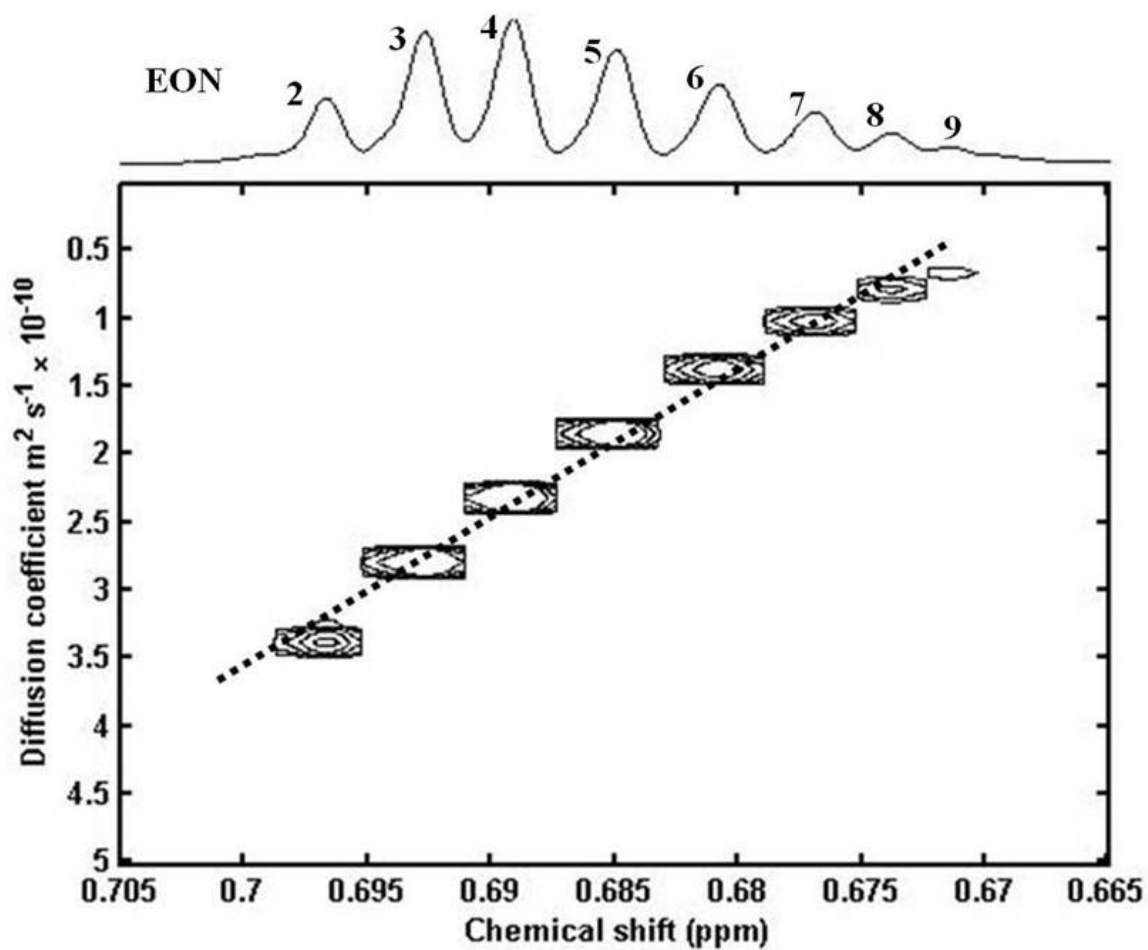


### *PGSTE NMR*

The diffusion coefficients were determined for the surfactant and the exchangeable protons in the microemulsion, and are reported for the sample “HNO<sub>3</sub> 0.1 M + NaF” in Table 3.3, and will be discussed in section 3.2.2 *PGSTE NMR*, together with the diffusion coefficients observed in the reaction medium.

The resolution of the signals in acidic inverse microemulsion of the *t*-Bu protons of various oligomers present in the commercial Igepal CA520 led to their unambiguous assignment by means of diffusion measurements and led also to assessment of their distribution. The measurements allowed gaining deeper insight into the medium by the determination of the partition degree between oil and aggregates for each oligomeric species. The experiment is of the kind of micelle assisted DOSY, but it can be defined as extreme since the object of interest are species with similar diffusion coefficients. At present, in order to increase the resolution of the molecules with close diffusion coefficients, methods like micelle assisted DOSY (MAD) [104-106] and chromatographic NMR [107] are under investigations. Both approaches are chromatographic as they rely on the differential partition between two phases.

The signal intensity for each oligomer in “HCl 0.1 M microemulsion” is reported in Table 3.2 as percentage, together with the appurtenant EONs, diffusion coefficients and partition parameters. From the measured  $D_s$  it was seen that the faster diffusing species are those with smaller EONs. Moreover, a linear relationship was envisaged in the DOSY spectrum (dotted line in Figure 3.16) between diffusion coefficients  $D_{obs}$  and chemical shifts  $\delta_{obs}$ ;  $D_s$  are progressively increasing upon increasing the resonance frequency. Thus the chemical shift variations within the oligomeric mixtures should be attributed mainly to the surrounding environment.



**Figure 3.16** Region 0.705 - 0.665 ppm, corresponding to the *t*-Bu signals, of the DOSY spectrum of Igepal CA520 in “HCl 0.1 M microemulsion”. The raw data were multiplied with a Gaussian apodization function to enhance resolution.

**Table 3.2** Diffusion coefficients and partition parameters for the individual oligomeric species obtained from the *t*-Bu signal in “HCl 0.1 M microemulsion”.

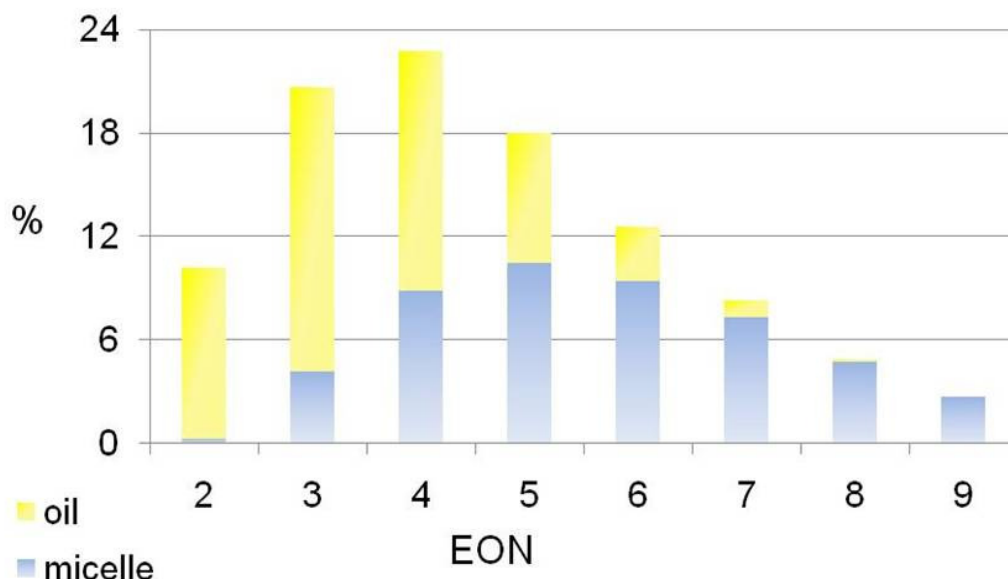
EON	Abundance [%]	$D_{\text{obs}}/10^{-10}$ [ $\text{m}^2\text{s}^{-1}$ ]	$X_{\text{oil}}$	$K_c$
2	10	3.38	0.98	0
3	19	2.80	0.80	26
4	21	2.32	0.61	61
5	18	1.85	0.42	123
6	14	1.38	0.25	266
7	9	1.02	0.11	628
8	5	0.79	0.03	1909
9	4	0.66	0	-

The preferential environment for each oligomer was calculated from Equation (3.1), using the values of measured diffusion coefficients ( $D_{\text{obs}}$ ). The molar fractions of oligomers in cyclohexane ( $X_{\text{oil}}$ ) are reported in Table 3.2, recalling that  $X_{\text{oil}} = 1 - X_{\text{mic}}$ .  $D_{\text{oil}}$  is the diffusion coefficient of Igepal in cyclohexane and  $D_{\text{mic}}$  is the diffusion coefficient of the micelles.

As  $D_{\text{oil}}$  the value of  $3.38 \cdot 10^{-10} \text{ m}^2 \text{ s}^{-1}$  was used [100] and as  $D_{\text{mic}}$  the  $D$  value of the molecules with EON= 9, which display the slowest diffusion, and it was in agreement with the value obtained from the Stokes-Einstein relation (Equation (1.3)) with the micellar radius,  $r_h = 3.7 \text{ nm}$ , determined by SAXS [103].

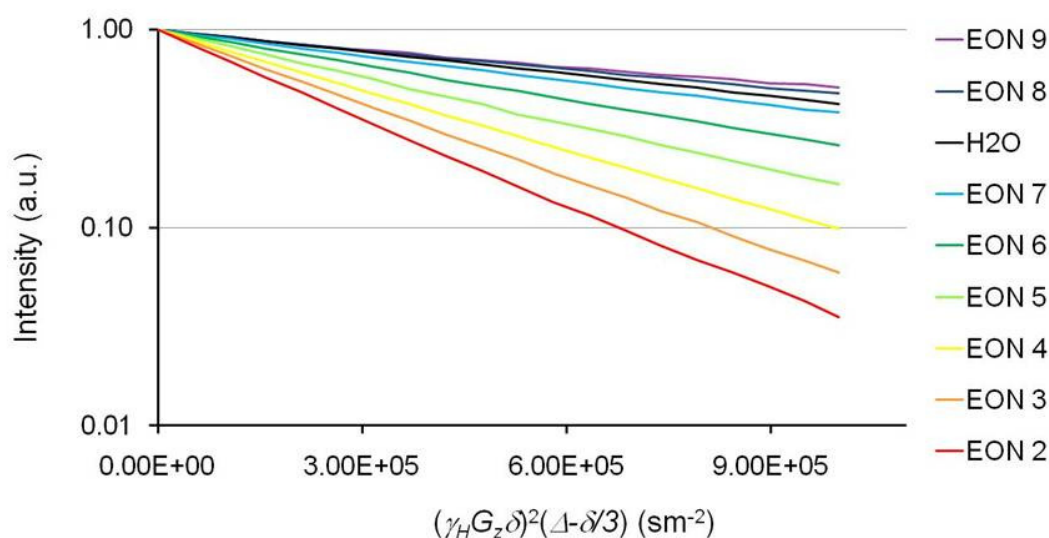
The molar fractions of Igepal oligomers in micelles and oil were highly influenced by their EON, and the variation of  $X_{\text{oil}}$  and  $X_{\text{mic}}$  according to EON is represented in Figure 3.17. The observed  $D$ s were lower for the more hydrophilic species, with higher number of EO units in the head group, not only because of the

higher molecular weight but also because they spent more time in the aggregates. The EON 5 molecules can be found in almost equal amount at the micellar interface and in the oil.



**Figure 3.17** Normalized signal intensities of *t*-Bu vs. EON; the columns represent molar fractions  $X_{oil}$  (yellow) and  $X_{mic}$  (blue) for each oligomer.

Noteworthy is that the EON 9 molecules, being present exclusively in the inverse micelles, had  $D$  even lower than that of exchangeable protons, mostly water of the inner pools,  $0.86 \cdot 10^{-10} \text{ m}^2 \text{ s}^{-1}$  (Table 3.3). The echo decays for *t*-Bu of different oligomers and for exchangeable protons are reported in Figure 3.18. It must be considered that the exchangeable proton signal reflects also the contribution of the small quantity of water dissolved in the oil, and of the OHs of the small EON species, resident mainly in the oil.

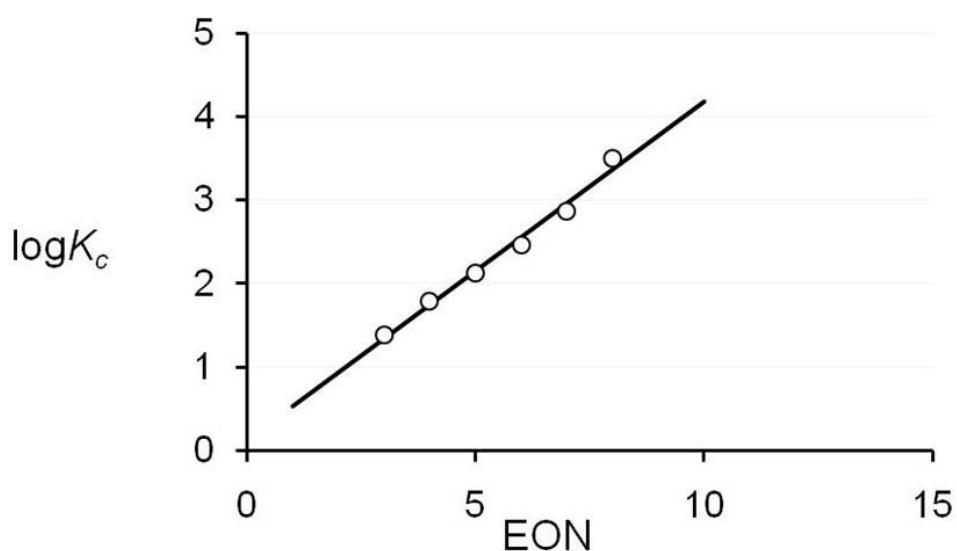


**Figure 3.18** Plot of the echo decays (log scale) for the *t*-Bu and the exchangeable protons signals.

High concentrations of the surfactant are an economical disadvantage, a waste and a nuisance in the isolation of the product. It was reported for Igepal CO520 that the surfactant dissolved in cyclohexane is 30 - 40% at high and it reaches even 90 - 100% at low water content [108,109]. In the system used in the present study the waste was about 50% as calculated from the EON distribution and the relevant  $X_{oil}$ . However, this experiment made possible the determination of the surfactant dissolved in oil and provided detailed information which may open new perspectives such as the design of mixtures of monodisperse surfactants capable of giving stable inverse micelles at reduced surfactant content. The EON 9 species might look like a promising starting candidate, however it was reported that a monodisperse EON species does not assure optimal results [46]. Conversely, the species with the lowest EON can be discarded since they reside entirely in the oil and do not contribute to the aggregates.

The values of the partition constant between the inverse micelles and the oil,  $K_c$ , obtained from Equation (3.2) are also reported in Table 3.2. The volume of the water solution was employed as that of the polar phase, but this is not entirely correct,

being the surfactant molecules confined at the interface, rather than dissolved in the inner phase; however, it is just a constant factor in all the  $K_c$ . The  $\log K_c$  is proportional to the free energy of transfer between the two environments in the ideal behavior approximation. The same correlation was noticed between  $\log K_c$  and EON, for EONs ranging from 3 to 8 (Figure 3.19). It is in line with the additivity of the contribution of the EO units to the free energy of transfer reported for polyethyleneoxide [110]. Noteworthy is that the intercept and the slope of the linear fit in Figure 3.19 are on the same order of magnitude of those found for ethoxylated octylphenols in a water/*n*-hexane bicontinuous microemulsion with the excesses of both oil and water [111].

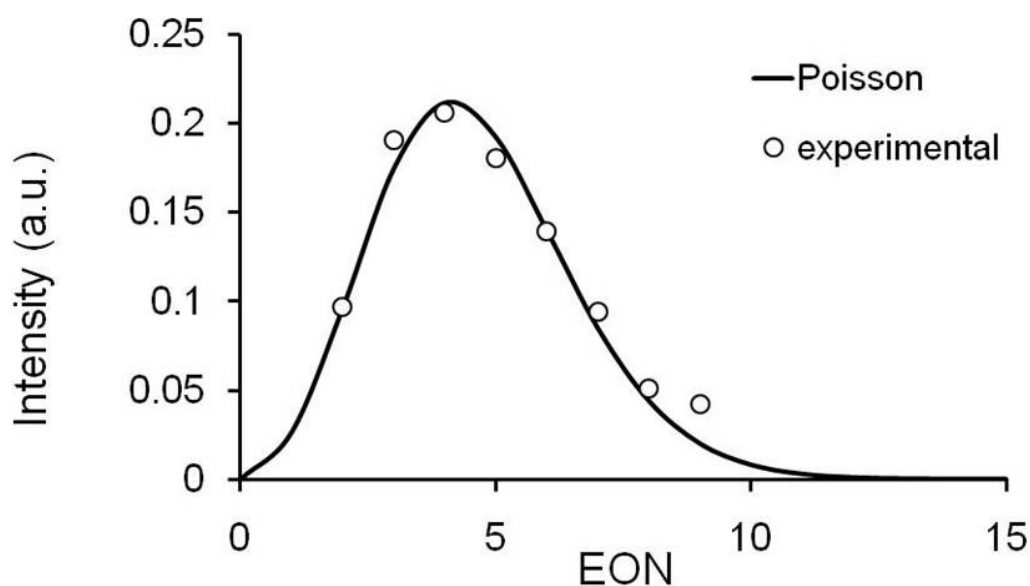


**Figure 3.19** Plot of the logarithm of the partition constant  $K_c$  as a function of their EONs, together with the linear fit.

The high resolution of *t*-Bu signals allowed the comparison of their intensities to that predicted by the Poisson distribution (Figure 3.20) in the form devised by Flory [62] for the polymers originated by the addition of monomers to a fixed number of polymer molecules, and exemplified right by polyethyleneoxides:

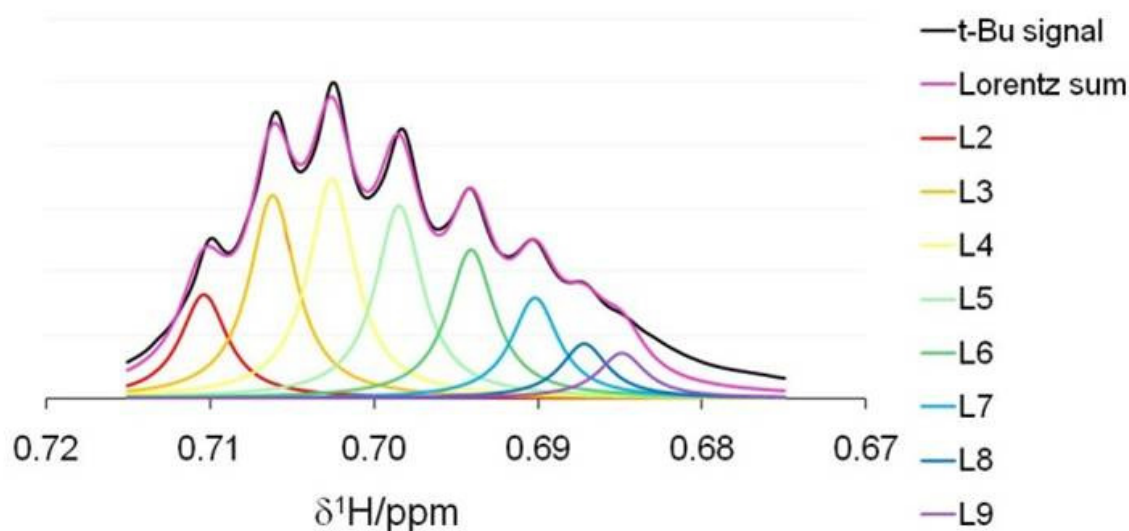
$$P(EON) = e^{-\nu} \frac{\nu^{EON-1}}{(EON-1)!} \quad (3.5)$$

The hypothesis of the Poisson distribution for the PEO head-groups resulted well suited, and in agreement with the indications of the producer. The distribution had value 4 (3.6 considering the first decimal digit) as mode ( $\nu$ ), and the mean EON was 5 (4.6 considering the first decimal digit).



**Figure 3.20** Plot of the experimental intensities normalized to 1, and of the calculated Poisson distribution vs. EON.

The *t*-Bu signals in the  $^1\text{H}$  spectrum were fitted by means of the sum of eight Lorentzian functions, numbered from 2 to 9 in Figure 3.21 according to the relevant EON number. The spectrum was processed with slightly increasing exponential window to improve resolution, keeping at the same time the Lorentzian shape. The intensities and line-width, the same for all eight functions, were optimized using the analysis tool Solver of the software Microsoft Excel2007, minimizing the squared errors with respect to the experimental signal.



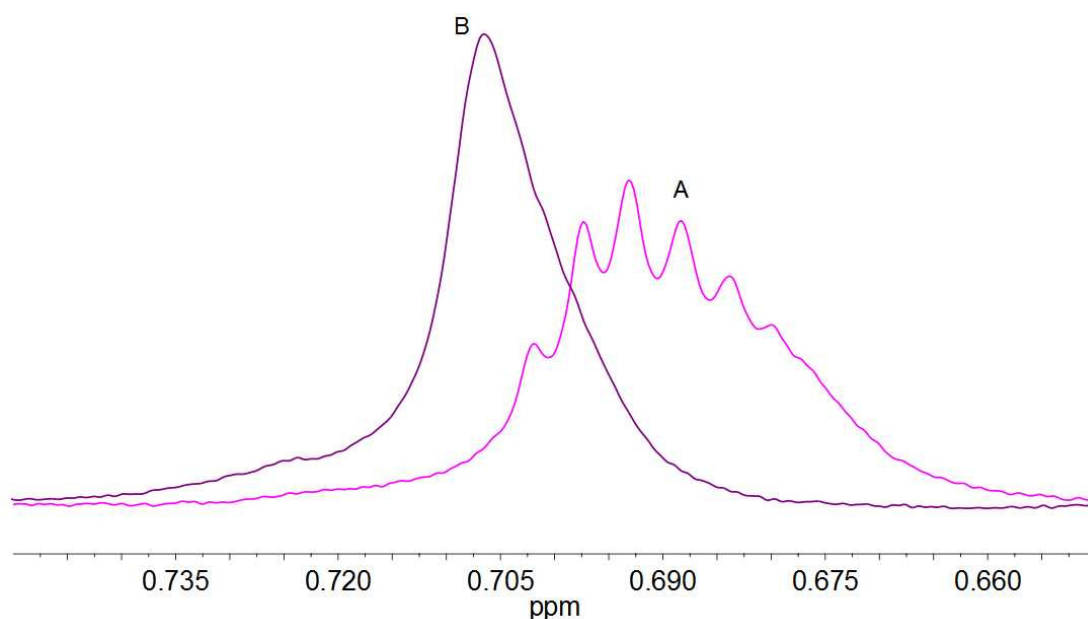
**Figure 3.21** Fitting of the experimental *t*-Bu  $^1\text{H}$  NMR signals (black trace) by means of the sum (pink trace) of eight Lorentzians.

### 3.2.2 NMR Characterization of Reaction Media

#### $^1\text{H}$ NMR

During the course of the hydrolysis reaction the water was consumed and the distinct separation among the *t*-Bu peaks decreased so the multiplet turned into singlet experiencing a slight shift to higher frequencies (Figure 3.22); this phenomenon may be used as an indicator of water consumption during the reaction. The same shift direction was also observed for the resonances of the  $\alpha$  protons.





**Figure 3.22**  $^1\text{H}$  NMR signal of the surfactant's *t*-Bu group for samples: (A) “ $\text{HNO}_3$  0.1 M + NaF” system at  $t = 0.5$  h and (B) at  $t = 20$  h after TEOS addition.

The substantial constancy of the  $^1\text{H}$  spectrum of the surfactant as the reaction proceeded suggested that the microemulsion remained stable throughout.

A small shift to a lower frequency of the exchangeable protons signal was observed during the hydrolysis reaction because of the consumption of the water and because of the presence of the new silanol protons and the new OH groups of the byproduct EtOH. This shift occurred earlier in the presence of NaF (several hours), as opposed to its absence (1 day). The signal broadened, although to a lower degree when compared to the analogue base-catalyzed system where the broadening effect was accompanied by the increase in quantity of silica being produced in the condensation step, as determined by SAXS [85]. It might be due to the participation of a mobile proton with a rather long residence time in the exchange, for instance, of water adsorbed on the silica surface [100].

The  $^1\text{H}$  NMR spectrum of TEOS in acidic medium did not differ with respect to that in the “ $\text{NH}_3$  microemulsion”, suggesting that in both cases the cyclohexane was its preferred localization. The TEOS and EtOH methylene signals resonated in the

same part of the spectral region for those of Igepal CH<sub>2</sub> β protons and the envelope of the inner EO protons of the surfactant head group, respectively. Hence, for simplicity, the reduction in intensity for TEOS CH<sub>3</sub> signals and the increase in intensity for the EtOH CH<sub>3</sub> signals were monitored and exploited to follow the progress of the hydrolysis step. No further signals that could be ascribed to partially hydrolyzed TEOS species were detected.

### <sup>13</sup>C NMR

In the <sup>13</sup>C NMR spectrum of Igepal signals of the hydrophobic moiety during the course of the reaction did not vary, however for the signals of the hydrophilic head group originating from oligomers with different EONs minor shifts and poorer resolution were noted which was attributed to the consumption of water.

Since TEOS is prevalently localized in cyclohexane, in both acidic and “NH<sub>3</sub> microemulsion”, carbon signals shifts were unaltered. Conversely, the EtOH CH<sub>3</sub> and CH<sub>2</sub> carbons shifted to lower frequencies with respect to those observed for the “NH<sub>3</sub> microemulsion”, up to 0.22 and 0.14 ppm, respectively, with slight regression when nearing the reaction completion. These chemical shift variations were of the same sign as those observed for the carbons of the surfactant head group and may be attributed to hydrogen bonding and to the presence of H<sup>+</sup>.

At variance with Stöber synthesis system and analogously to basic microemulsion, in the acidic one in <sup>13</sup>C NMR spectra no signals of partially hydrolyzed TEOS species were observed.

### PGSTE NMR

The diffusion coefficients were measured, besides in the microemulsion, in the reaction medium 53 h after the reaction beginning (Table 3.3). The values are reported for the sample “HNO<sub>3</sub> 0.1 M + NaF”, where the Ds were observed for the surfactant, the exchangeable protons and EtOH.

**Table 3.3** Diffusion coefficients reported in  $10^{-10} \text{ m}^2 \text{ s}^{-1}$  plus/minus the standard error from the fitting process and measured at 25 °C, for the sample “HNO<sub>3</sub> 0.1 M + NaF”.

Sample	Igepal <i>t</i> -Bu	Exchangeable protons	EtOH
microemulsion	$2.00 \pm 0.07$	$0.86 \pm 0.002$	
reaction medium at <i>t</i> = 53 h	$2.10 \pm 0.04$	$1.92 \pm 0.002$	$6.23 \pm 0.02$

The diffusion coefficients were determined from the echo decay of the proton signal of the Igepal *t*-Bu group, of the exchangeable proton signal and of the signals corresponding to the relevant methyl triplet of EtOH. The diffusion coefficient reported for *t*-Bu protons of Igepal in the microemulsion in Table 3.3 is an average value of various oligomers. The echo intensities, registered during the constant diffusion interval,  $\Delta = 100 \text{ ms}$ , were fitted to the Stejskal-Tanner equation (1.8) neglecting the nuclear relaxation term.

In the microemulsion, prior to TEOS addition, the diffusion coefficient of the exchangeable protons,  $0.86 \cdot 10^{-10} \text{ m}^2 \text{ s}^{-1}$ , mostly revealed the diffusion of the micellar core, as the protons were prevalently confined inside it. While in the reaction medium 53 hours after the reaction beginning it was remarkably higher ( $1.92 \cdot 10^{-10} \text{ m}^2 \text{ s}^{-1}$ ) due to the contribution of the alcoholic proton of the byproduct EtOH, a large part of which diffused into cyclohexane.

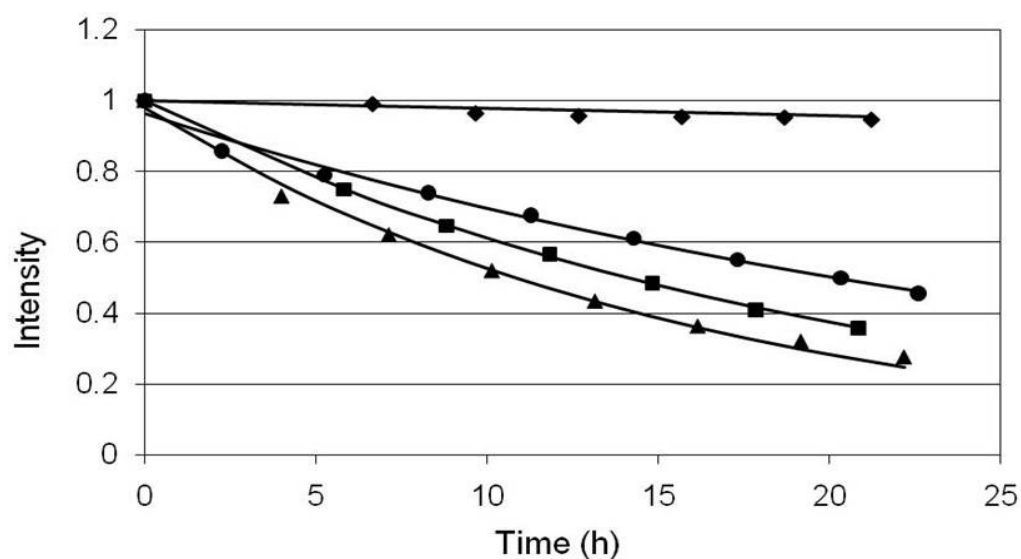
The finding that EtOH is residing predominately in the oil phase was supported by its molar fraction in the micelles,  $X_{\text{mic}} = 0.36$ , calculated in the same manner as in base-catalyzed system, through Equation (3.1). As the diffusion coefficient of the micelles,  $D_{\text{mic}}$ , the value of  $0.66 \cdot 10^{-10} \text{ m}^2 \text{ s}^{-1}$  was used, which is the one measured for the EON 9 molecules in the microemulsion and also derived from the Stokes-Einstein relation (Equation (1.3)) with  $\eta = 0.9 \text{ mPa s}$  and micellar radius,  $r_h = 3.7 \text{ nm}$ , afforded by SAXS [103].  $D_{\text{obs}}$  is the actual value for EtOH in the reaction medium 53 h after the reaction beginning ( $6.23 \cdot 10^{-10} \text{ m}^2 \text{ s}^{-1}$ ) when most of the TEOS had reacted. Therefore,

by employing an acid solution as the water pool, the EtOH concentration in the micellar cores at reaction completion is much higher than that for concentrated  $\text{NH}_3$ , where value of  $X_{\text{mic}}$  is 0.06 [100].

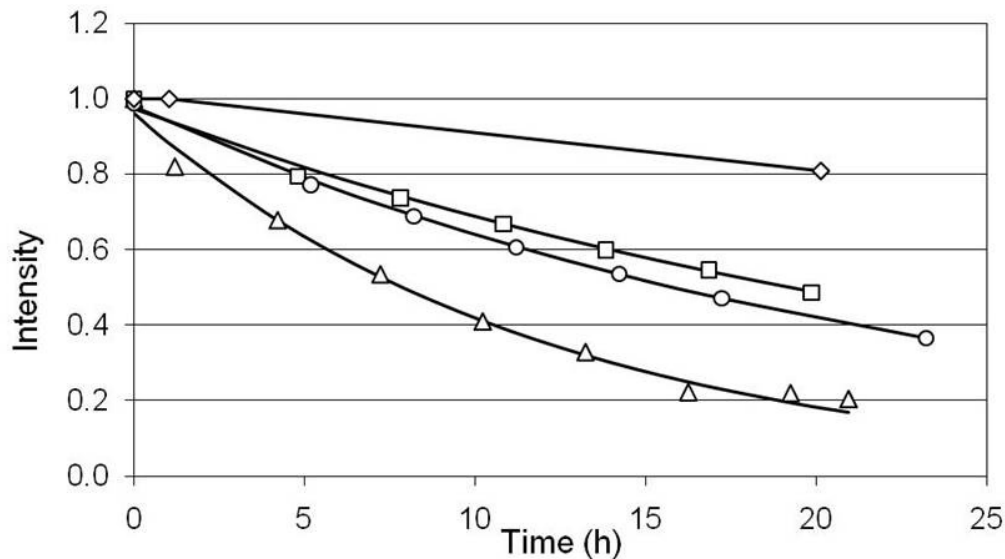
### 3.2.3 Hydrolysis

The decay of TEOS  $\text{CH}_3$  proton signal, monitored for  $\sim 20$  hours, where the spectra were registered every 3 hours, was satisfactorily fitted by means of an exponential function, and is reported in Figure 3.23 for  $\text{HNO}_3$  and in Figure 3.24 for HCl samples. It indicated that in the nonionic inverse microemulsion the hydrolysis of TEOS follows first-order kinetics, analogously to basic medium [53,54,100] and bulk solution [101]. The decay of TEOS carbon signals was also monitored for  $\sim 20$  h and the spectra were registered at the same time intervals as  $^1\text{H}$  spectra. Furthermore, the trends of the intensities of TEOS carbon signals during the reaction are in line with those of the corresponding proton signals. The trend was further confirmed by the intensity trend of EtOH  $\text{CH}_3$  protons. The kinetic constants, given as  $k_h$  in Equation (3.6), are reported for all the samples analyzed in Table 3.4. Each value is the result of an average for two independent measurements.

$$\frac{d[\text{TEOS}]}{dt} = -k_h[\text{TEOS}] \quad (3.6)$$



**Figure 3.23** Intensity of the  $^1\text{H}$  NMR signal of the  $\text{CH}_3$  groups of TEOS for reaction media: “ $\text{HNO}_3$  0.05 M + NaF” (filled diamonds), “ $\text{HNO}_3$  0.05 M” (filled circles), “ $\text{HNO}_3$  0.1 M + NaF” (filled squares), and “ $\text{HNO}_3$  0.1 M” (filled triangles). The black lines are the fitting of the intensities carried out by means of Eq (3.6).



**Figure 3.24** Intensity of the  $^1\text{H}$  NMR signal of the  $\text{CH}_3$  groups of TEOS for reaction media: “HCl 0.05 M + NaF” (empty diamonds), “HCl 0.05 M” (empty circles), “HCl 0.1 M + NaF” (empty squares), and “HCl 0.1 M” (empty triangles). The black lines are the fitting of the intensities carried out by means of Eq (3.6).

**Table 3.4** Investigated samples with the relevant  $k_h$ .

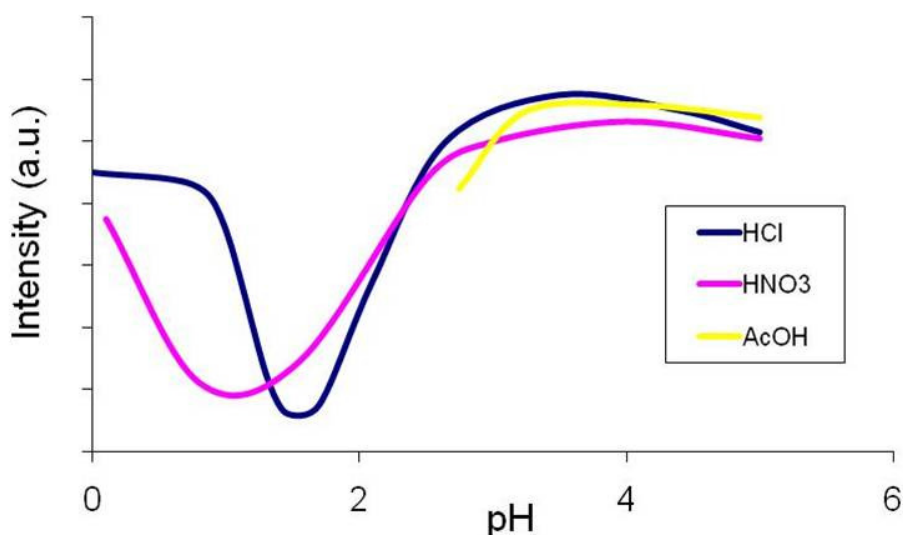
Sample	$k_h$ [h <sup>-1</sup> ]
HNO <sub>3</sub> 0.1 M	0.06
HNO <sub>3</sub> 0.05 M	0.05
HNO <sub>3</sub> 0.1 M + NaF	0.03
HNO <sub>3</sub> 0.05 M + NaF	< 0.01
HCl 0.1 M	0.08
HCl 0.05 M	0.03
HCl 0.1 M + NaF	0.04
HCl 0.05 M + NaF	< 0.01

First-order kinetics with respect to both water and acid have been reported [101] and in our system the  $k_h$  was about halved upon halving the H<sup>+</sup> concentration. The reaction rates proved to be very sensitive to the water content; therefore, several attempts were necessary to prepare microemulsion with a proper volume of the acid solution as aqueous phase in order to establish a hydrolysis rate on the same order of magnitude to that found in base-catalyzed microemulsion [100].

The presence of NaF led to a remarkable decrease of  $k_h$  in the 0.05 M acid microemulsions, however it was of minimal importance for the systems containing acid with a 0.1 M concentration, as already shown by Finnie *et al.* for TMOS hydrolysis [8]. Due to the basic properties of F<sup>-</sup>, in the water core of the inverse micelles it was present mainly in undissociated HF form, and therefore responsible for the decrease of the H<sup>+</sup> concentration, causing the observed decrease of TEOS hydrolysis rates.

Our measurements of  $k_h$  clearly pointed out the rate dependence on the nature of the acid catalyst. This is in line with the specific effect of the acid anion found in the

condensation step of the synthesis of silica in bulk solution (Figure 3.25) [23] and the reason why the synthesis in microemulsion was carried out with different acids.

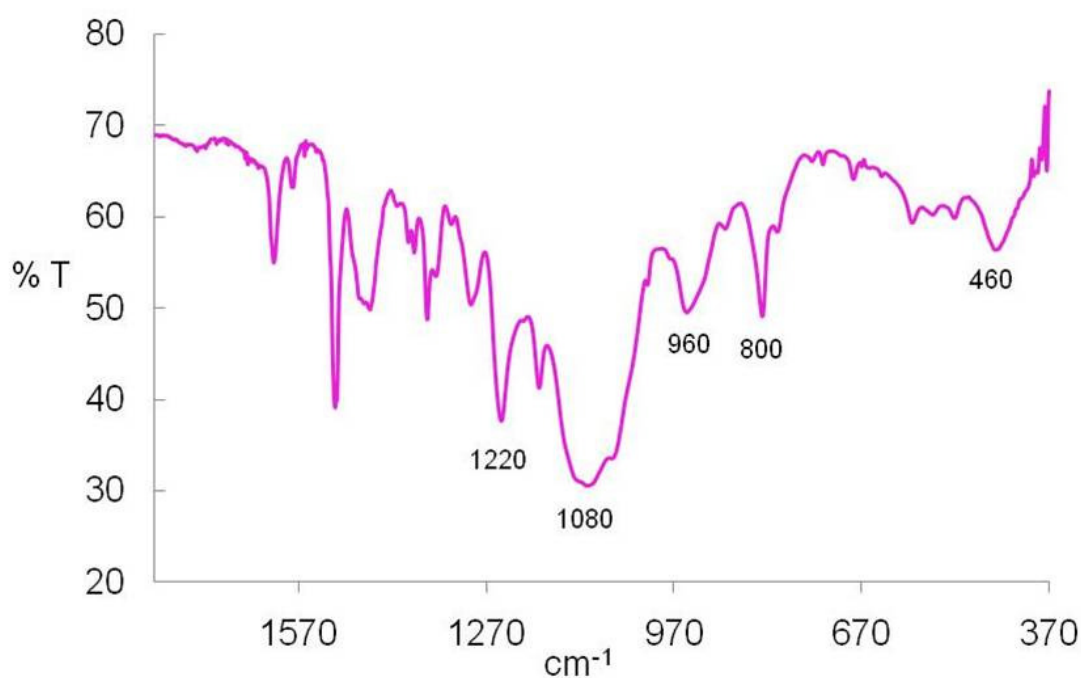


**Figure 3.25** The variation of the condensation rate according to pH for acids: acetic, hydrochloric and nitric [112].

At very low pH values, HCl induces shorter gel times than HNO<sub>3</sub>, with a crossover at slightly higher pH's, yet always below the silica isoelectric point. This holds also for the synthesis of mesoporous silica with nonionic surfactant assemblies as structure directing devices, where faster rates of alkoxide hydrolysis were obtained in the presence of hydrophilic ions (e.g., F<sup>-</sup>, SO<sub>4</sub><sup>2-</sup>) because of their dehydrating action on the nonionic micellar surface [113]. Indeed, hydrophilic anions compete with the surfactant for water causing a decrease in the surfactant's cloud point. An alternative explanation may be the change in permeability of the surfactant layer as a result of the specific interaction of acid anions with PEO groups and other nonionic polar polymers [114,115]. Zhao *et al.* [116] proved a specific anion effect synthesizing mesoporous silica in the acid-catalyzed system with PEO as templating agent, where silica precipitation becomes faster in the order HBr ≈ HCl < HI < HNO<sub>3</sub> < H<sub>2</sub>SO<sub>4</sub> < H<sub>3</sub>PO<sub>4</sub>.

### 3.2.4 Condensation

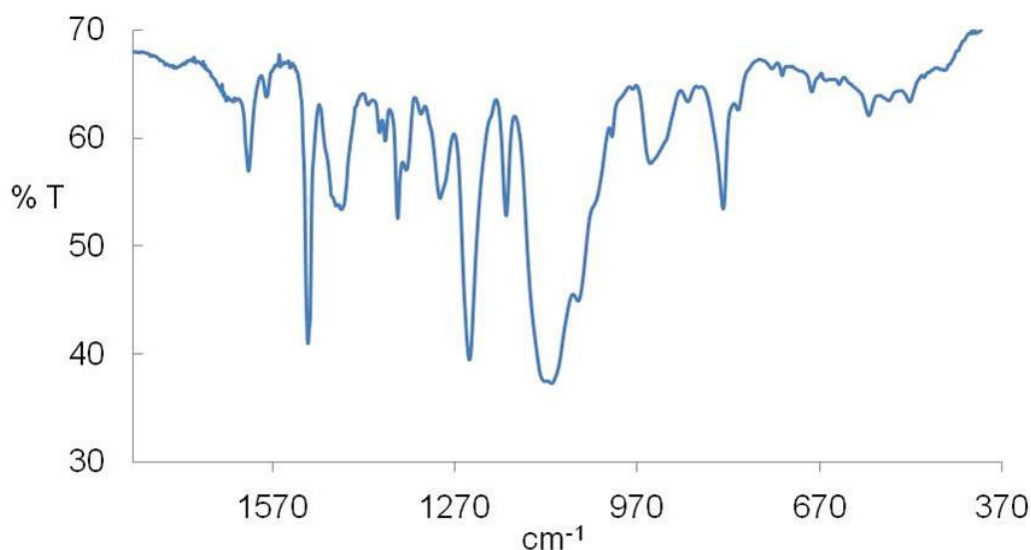
The condensation was followed by FTIR spectroscopy preparing the samples as thin film on potassium bromide pellets. The characteristic bands of silica (Figure 3.26), according to the literature [117], are those at  $1220\text{ cm}^{-1}$  and  $1080\text{ cm}^{-1}$  of the longitudinal and transversal Si-O-Si asymmetric stretching modes, respectively, the band of the symmetric one at  $800\text{ cm}^{-1}$  and additional stretching of the terminal silanol bonds at  $960\text{ cm}^{-1}$ . The band at  $460\text{ cm}^{-1}$  is assigned to Si-O-Si bending modes of tri- and tetra-substituted silicon sites in the polymers [23,118]. The exact position of the bands depends on the degree of silica cross-linking and its physical structure. In amorphous silica, bond lengths and angles may vary sensitively with respect to the ideal geometry of a compact assembly of  $\text{SiO}_{4/2}$  tetrahedra.



**Figure 3.26** FT-IR spectrum of “ $\text{HNO}_3$  0.1M+NaF” system 25 h after TEOS addition. Numbers are indicating characteristic  $\text{SiO}_2$  bands.



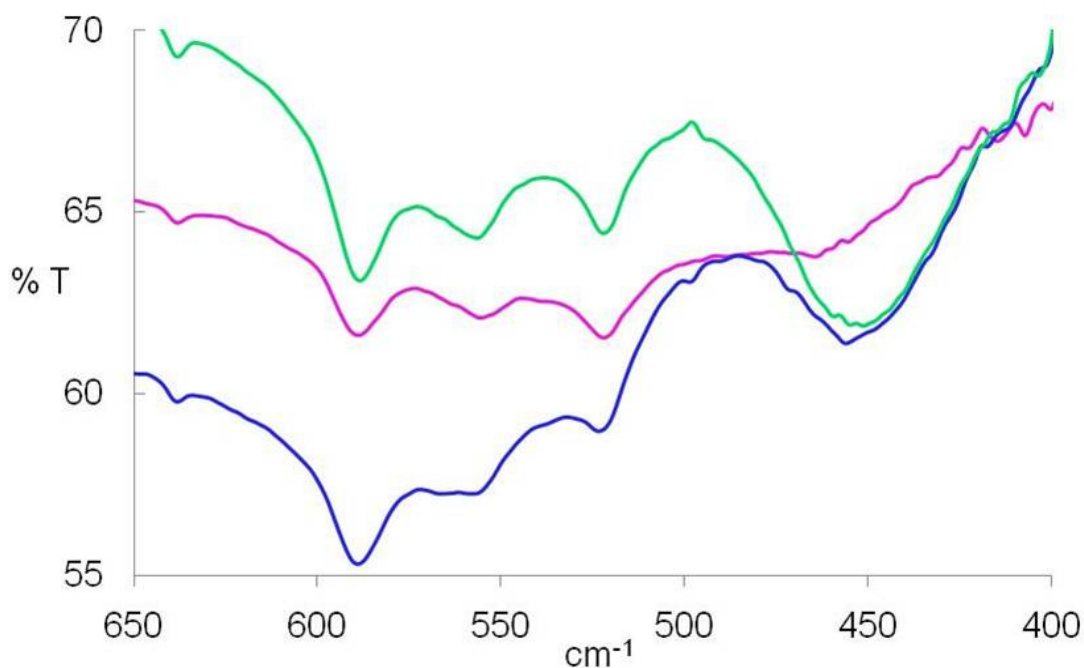
The bands of other components of the reaction medium in the IR spectrum, at the concentrations employed herein, were dominated by the strong surfactant and water signals. However, as it can be seen from the spectrum of Igepal in cyclohexane solution, reported in Figure 3.27, the exception was the lower frequency region where there were no signals observed.



**Figure 3.27** FT-IR spectrum of Igepal cast as a thin film on a KBr pellet from a cyclohexane solution.

The band of Si-O-Si bending was clearly evident between 400 and 500  $\text{cm}^{-1}$  so it was the most suited one to follow the silica formation. Moreover, it was not influenced by hydrolysis step since in the “ $\text{HNO}_3$  0.1 M system”, the band at 455  $\text{cm}^{-1}$ , absent at reaction commencement, began to be noticeable after 5 h when the quantity of hydrolyzed TEOS was approximately 40%, and continued to intensify for a few days. This suggested that under strongly acidic conditions the hydrolysis reaction completes long before the gel point, even though the TEOS hydrolysis was quite slow in the present microemulsion systems with respect to that of TMOS [8], and of the same order of magnitude as the “ $\text{NH}_3$  microemulsion” system [54,85,100]. Therefore,

it was concluded that the rate of condensation is still delayed with respect to the rate of hydrolysis (Figure 3.28).

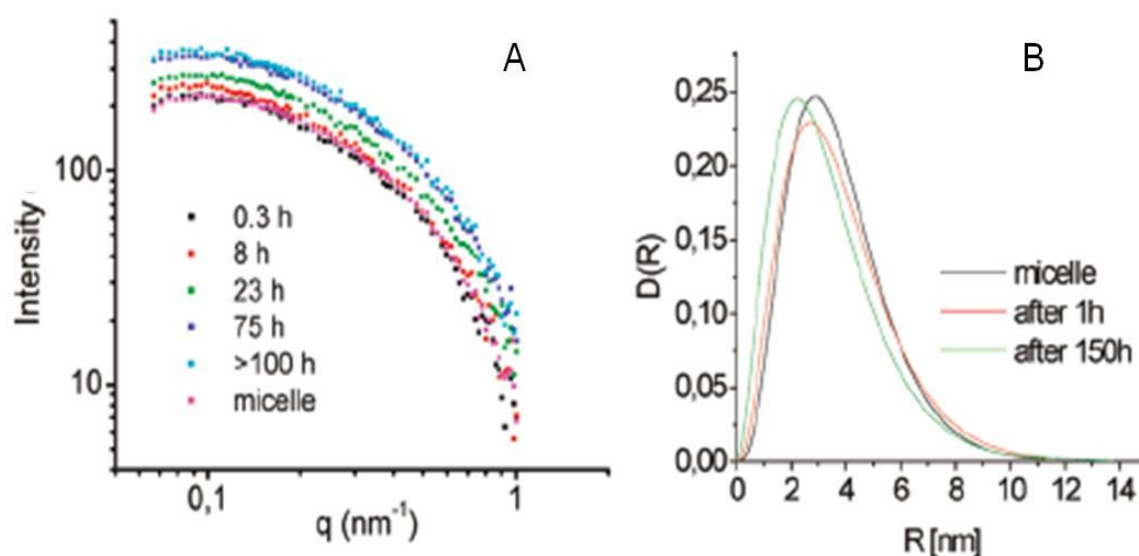


**Figure 3.28** 650-400  $\text{cm}^{-1}$  region of the FT-IR spectra for the systems “ $\text{HNO}_3$  0.1 M” at  $t=5$  h (purple) and at  $t=25$  h (blue), “ $\text{HNO}_3$  0.1M+NaF” at  $t=25$  h (green) after TEOS addition.

Furthermore, the band at  $455 \text{ cm}^{-1}$  confirmed the ability of NaF to accelerate the condensation, as previously noted [82]. The two analogue systems, in absence and presence of  $\text{F}^-$  revealed that the band of silica is much stronger in the latter case in spite of slightly slower hydrolysis. The action of fluoride should not be exclusively kinetic, but also mechanistic, according to the findings of Winter *et al.* [82] who showed that its presence produced highly branched polymers at the early stages of the process in bulk syntheses.

## SAXS

The microemulsion systems, monitored *in situ* at different time intervals, before and after the addition of TEOS, according to SAXS patterns maintained the same size distribution with a characteristic micellar core radius of  $\sim 4$  nm with no evidence of other characteristic sizes. Moreover, the data in Figure 3.29 A) show the completion of the reaction kinetics at 100 h.



**Figure 3.29** A) Scattering spectrum of the sample “HNO<sub>3</sub> 0.1 M + NaF” as a function of time (log-log scale) after TEOS addition and cyclohexane scattering subtraction. B) Distribution of the particle radii of the same system before and after 1 and 150 h the addition of TEOS [103].

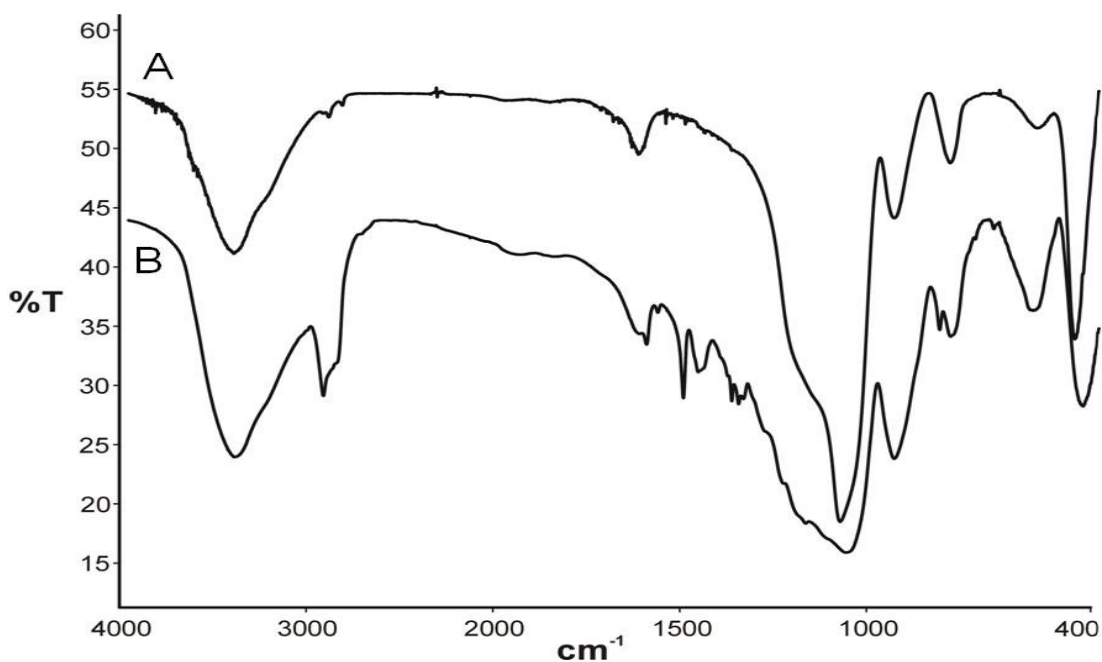
The absence of big particles confirmed that no coalescence takes place between the droplets content during intermicellar collision. The electron density of the internal phase increased and it was related to the presence of the polymerization product inside the water pools, while the micelles remained intact. The size of the micelles therefore limited the size of the nanoparticles to about 4 nm making them hardly visible on TEM micrographs.

According to the quantitative results, under the assumption that all TEOS had reacted, the final averaged volume of silica was  $\sim 15$  % with a significant percentage of water and EtOH present in the pools.

### 3.2.5 Characterization of the Products

#### IR Spectra

The IR spectrum of the silica nanoparticles synthesized in acid-catalyzed system displayed an intense band at  $960\text{ cm}^{-1}$  of silanol Si-O stretching, in agreement with a considerable amount of residual SiOH groups, similarly to the one of the product obtained with the bulk method, while the envelope of the stretching Si-O-Si bands between  $1250$  and  $1060\text{ cm}^{-1}$  was broader, suggesting a higher skeletal disorder [119]. Another small difference was the more intense band at  $580\text{ cm}^{-1}$ , indicative of the presence of four-membered rings [120].



**Figure 3.30** FT-IR spectrum of silica obtained from A) classical HCl-catalyzed sol-gel process and of B) silica obtained from the “HCl-0.1M” system, also showing weak signals due to igepeal residues.

### TEM Analysis

The micrographs in Figure 3.31 are representative examples of all the isolated samples and they show similar structural features. The solid products were isolated from the “HNO<sub>3</sub> 0.1 M + NaF” (A and B) and “HCl 0.1 M” (C) reaction media and the two types of silica nanostructured materials were identified:

- (i) spherical particles with size  $\langle R \rangle_{\text{TEM}}$  equal to about 2 nm, significantly smaller than the micellar size determined by SAXS (A and C), and
- (ii) larger, irregularly shaped aggregates with sizes up to 100 nm (B).

The presence of the larger aggregates was less evident in the HCl systems. Nonetheless, for all observed systems the notable spherical particles were relatively few.

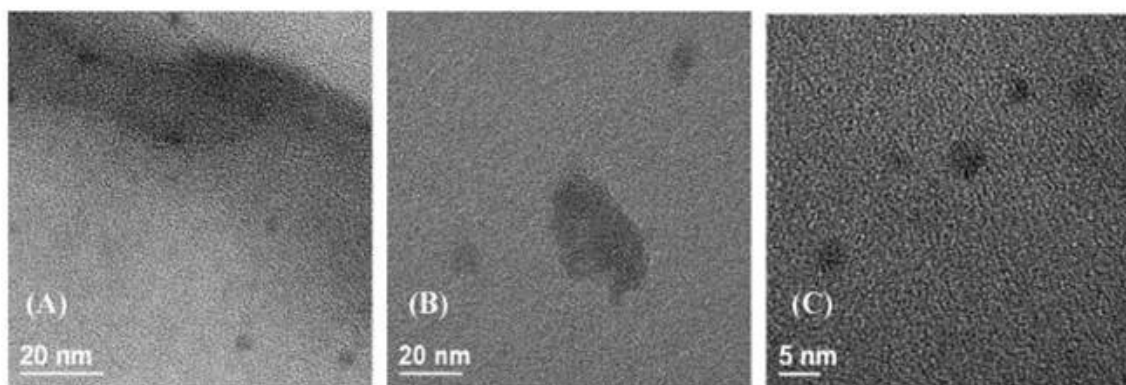
The surfactant barrier, preventing the coagulation of primary particles, provided steric stabilization which was necessary to keep the particles apart in acidic medium, where the aggregates are either uncharged or very weakly charged. At the completion of the synthesis the isolation of the product led to the destabilization of the microemulsion system. The content of the core of the inverse micelle came in contact, and reacted, with the content of the nearest pools to form larger aggregates, through, for example, coupling of clusters; whereas some isolated micelles formed spherical particles with the size of the inverse micelle core.

There are two possible scenarios for TEOS partitioning into the inverse micelles during the reaction:

- (i) homogeneous partitioning - at the end of reaction each micelle core contains a gel of reacted TEOS, water, and EtOH with more or less the same composition;
- (ii) non-homogeneous partitioning - at the end of reaction there is the contemporary presence of empty, partially, or completely filled pools, where the core is simply water, or a mixture of water, EtOH, and TEOS, hydrolyzed or partially condensed to form silica.

In spite the different synthesis paths possible the final product was the same, and the difference between the sizes of the single spherical particle obtained by SAXS and TEM ( $\langle R \rangle_{\text{SAXS}} = 4$  nm and  $\langle R \rangle_{\text{TEM}} = 2$  nm) was a result of a shrinkage effect due to the evaporation of the solvents from the gel during the sample

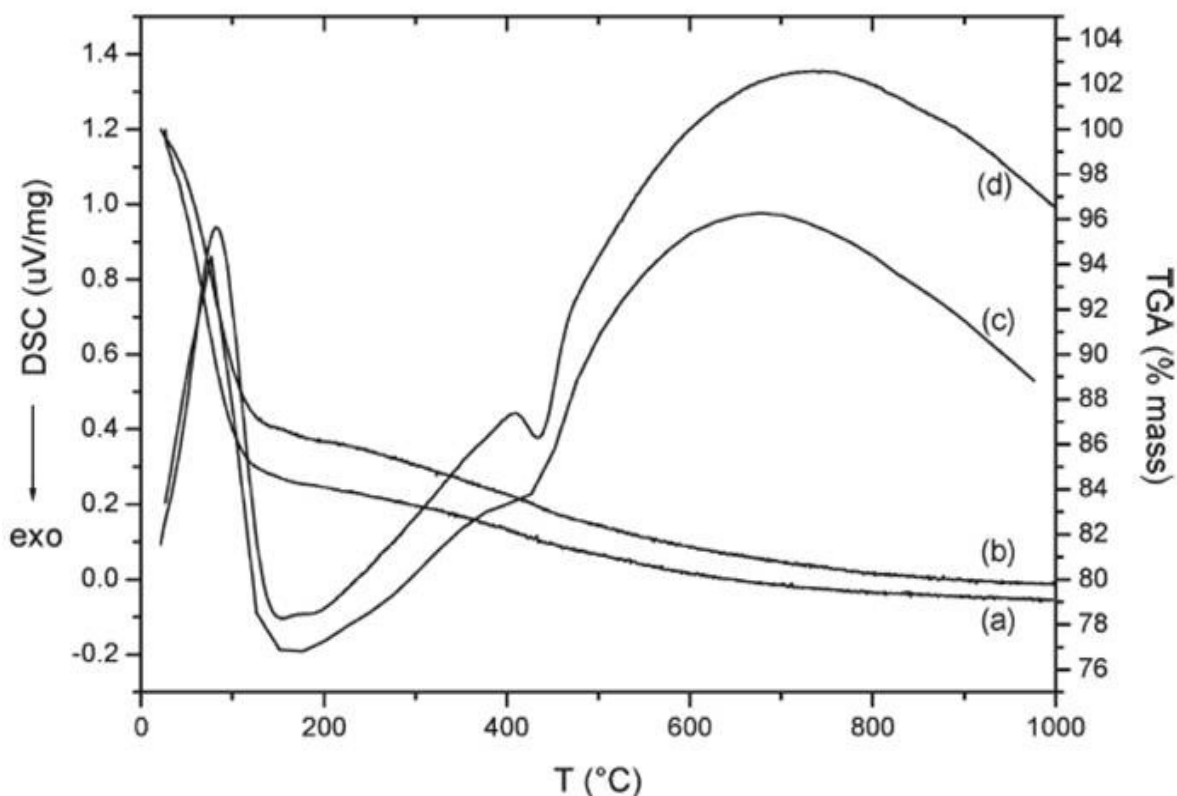
preparation for TEM analysis. The volume of the particle obtained by TEM was about 15 % smaller of the one obtained by SAXS, that is, in line with the volume fraction of the silica found in the pools at the end of the reaction.



**Figure 3.31** TEM micrographs of solid silica isolated from the “HNO<sub>3</sub> 0.1 M + NaF” (A and B) and “HCl 0.1 M” (C) reaction media.

#### *TGA and DSC Measurements*

The final products obtained in the microemulsion systems were compared with the classical HCl-catalyzed sol-gel silica, where the synthesis procedure was adapted from the literature [44]. As an example of acidic microemulsion the “HCl 0.1 M” sample was taken. The weight loss observed with TGA for the two samples did not differ significantly, with the mass loss percentage of 20.91 for the former and 20.26 for the latter [103] (Figure 3.32 a) and b)). The mass loss visible between 30 and 130 °C was ascribed to the removal of physisorbed and chemisorbed water, and any residual solvent as would be expected to be present in both samples. A further weight loss, although less significant, occurred between 130 and 600 °C, and was attributed to complete dehydroxylation of surface silanols to give siloxane groups and the removal of any unhydrolyzed ethoxy groups arising from TEOS.



**Figure 3.32** TGA of (a) silica prepared in “HCl 0.1 M microemulsion” and (b) silica prepared via classical HCl-catalyzed sol-gel. DSC of (c) silica prepared in “HCl 0.1 M microemulsion” and (d) silica prepared via classical HCl-catalyzed sol-gel.

Moreover, DSC data demonstrated the similarity between silica prepared with the two methods, in microemulsion and bulk. An endothermic peak visible between 30 and 140 °C, extremely similar for both samples, was assigned to the removal of surface bound water [103] (Figure 3.32 c) and d)). The proceeding transitions, also endothermic, indicated a similar profile for the dehydroxylation of silanol groups and removal of unhydrolyzed alkoxy groups [3].

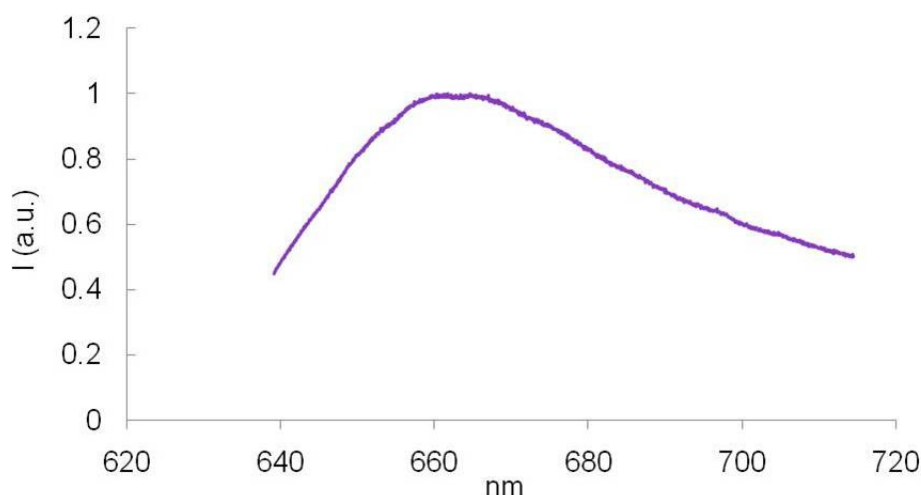
The consistency of the observed TGA and DSC data in Figure 3.32 confirmed the formation of a sol-gel like silica structure in the water pools of the “HCl 0.1 M microemulsion” and also the similarity between the products obtained by acid-catalyzed sol-gel methods in microemulsion and bulk. It appeared that under the

conditions employed herein the reaction was not significantly different from the one in bulk solution, yet the TEOS hydrolysis was slowed down in the microemulsion due to its compartmentalization in the oil. However, the hydrolysis rate was not crucial for the control of the particle size, which was determined by the size of the micellar core.

### *Fluorescence of SiO<sub>2</sub> Nanoparticles*

The fluorescence phenomenon has been deeply investigated in bulk silica [121] and presently is under scrutiny in silica nanoparticles [122,123]. The fluorescence obtained from the absorption in the UV region is very important for practical applications because it implies the conversion of UV radiation into visible light [24]. Silica fluorescence undergoes thermal quenching [121] so the emission spectra obtained by visible irradiation at room temperature are very weak.

The fluorescence of the SiO<sub>2</sub> nanoparticles prepared in “HCl 0.1 M microemulsion” was observed after the irradiation with a HeNe laser with energy of 1.96 eV (633 nm). The curve, reported in Figure 3.33, peaked at 1.87 eV (664 nm) has an asymmetric shape with the tail at lower energies.



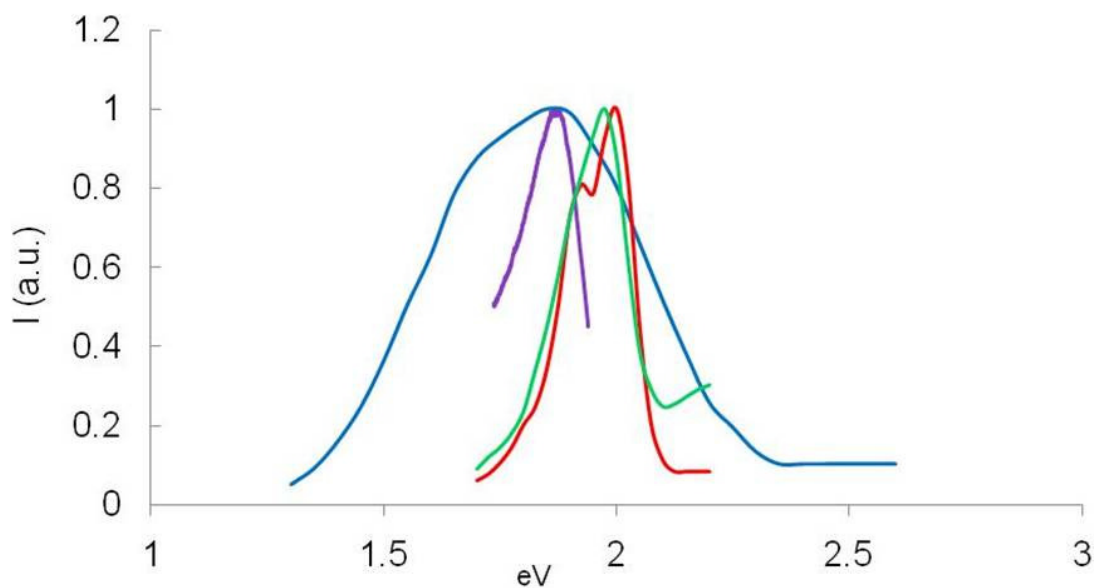
**Figure 3.33** Photoluminescence emission spectrum of SiO<sub>2</sub> nanoparticles prepared in “HCl 0.1 M microemulsion” with excitation at 633 nm (1.959 eV).



In bulk silica two distinct absorption bands can originate the photoluminescence emission band centered at 1.9 eV [121]. The former corresponds to a strong ultraviolet (UV) absorption band at 4.8 eV (oscillator strength  $f= 0.03\text{--}0.05$ ) [124,125] and the latter to a weak absorption at 2.0 eV ( $f= 1.5\cdot 10^{-4}$ ) [124,126-128]. Responsible for the emission around 1.9 eV are defects corresponding to the non-bridging oxygen hole center (NBOHC) or oxygen dangling bond,  $\equiv\text{Si-O}\bullet$ , where ( $\equiv$ ) and ( $\bullet$ ) symbolize the bond with three oxygens and an unpaired electron, respectively [126]. Luminescence and EPR investigations, together with theoretical investigations, localized the unpaired electron on the radical oxygen [129]. The very high specific surface area of silica nanoparticles favors a large concentration of surface structural defects and therefore luminescence [122]. However it must be considered that the system may contain significant amounts of  $\text{Cl}^-$ , a well known quencher.

In silica coating after densification at 500 °C in air photoluminescence was also observed at still lower energies (higher  $\lambda$ ), e.g. a luminescence peaked between 360 and 370 nm (3.44 and 3.35 eV) with excitation peak at about 320 nm (3.85 eV) [130].

It is interesting to compare the fluorescence spectrum of the present nanoparticles with those reported in literature (Figure 3.34). The ensemble spectrum of the silica nanopowder, which had been prepared by laser pyrolysis of silicon nanocrystals, and attributed to the luminescence of nonbridging oxygen hole centers (NBOHCs;  $\equiv\text{Si-O}\bullet$ ), covers a wide range of wavelength [123]. This is likely due to a broad distribution of sizes of the nanoparticles. The much narrower spectrum of the two Aerosil300 samples, which differ with respect to the thermal treatment, is in line with good size homogeneity of the nanoparticles, with an average size of 7 nm [122]. The as narrow spectrum of our nanoparticles is in agreement with good size homogeneity, too. The lower energy of the maximum may be due to the somewhat smaller size (4 nm), hence the photoluminescence spectrum might be exploited to determine the particle size. However, texture differences cannot be ruled out in determining the position of the maximum and the bandwidth.



**Figure 3.34** Fluorescence spectra of SiO<sub>2</sub> nanoparticles prepared in “HCl 0.1 M microemulsion” (purple) excitation at 1.959 eV, Aerosil sample 1 (red) and Aerosil sample 2 (green) with excitation at 4.77 eV [122], polydisperse silica nanoparticles (blue) with excitation at 266 nm (4.66 eV) [123].

### 3.3 Comparison of Base and Acid-Catalyzed Syntheses

In base-catalyzed systems the kinetic of hydrolysis of the alkoxide determines the size of the final product [53], whereas in acidic microemulsion very small particles are afforded by the sol-gel process, irrespectively of the starting material, either TEOS or TMOS, which undergoes complete hydrolysis in microemulsion in half an hour [8].

The nucleation and growth processes depend on pH, so below the silica isoelectric point hydrolysis is favored, while both condensation and dissolution

reactions are hindered which means that a lot of nuclei are generated quickly, but very small growth takes place. In base-catalyzed microemulsion the aggregates grow through the addition of monomers, originated also by the concurrent depolymerization reaction which, on the contrary, does not take place in acidic medium where the aggregates grow through the coupling of clusters. Acid-catalyzed systems produce microporous nanoparticles with open, randomly branched structure since it is predicted the formation of linear siloxy chains through a protonated silanol, thus preferentially involving more reactive chain-end silicate species; base-catalyzed systems, on the other hand, produce nanoparticles with high density of cross-linking [23].

Very small particles, with diameters of 5-15 nm, were obtained in HCl-catalyzed inverse microemulsion, however at pH above silica isoelectric point, by means of a reaction route in which the hydrolysis step is completely bypassed [71,131]. The starting materials were sodium meta and ortho silicates and they polymerized in an Igepal/cyclohexane inverse microemulsion where it was observed that the size of the final particles can be increased simply by increasing silicate concentration in the water phase. This confirmed the hypothesis of Finnie *et al.* [8] that the small size of the particles may be attributed to the efficient barrier effect of the surfactant film which prevents the coagulation of primary particles. Due to the barrier, particles grow inside the pools by condensation of hydrolyzed precursor and there is no exchange of the droplet contents during intermicellar collisions.

In both acid and base-catalyzed systems employed herein the size of the final particles cannot be increased by increasing TEOS concentration since this would imply the increase of EtOH concentration, a part of which remains in the micellar core, and in higher quantity would provoke the rupture of the microemulsion.

During the isolation of the nanoparticles from the reaction medium the surfactant was not removed completely in order to provide the steric stabilization otherwise they aggregate due to the lack of charge. Conversely, in a basic microemulsion charge stabilization is active due to the electrostatic repulsion.

### 3.4 Cu<sup>2+</sup> and Co<sup>2+</sup> Doped SiO<sub>2</sub> Nanoparticles

The sol–gel method allows doping materials with a large number of organic and inorganic molecules, thus increasing the range of applications in many fields of science and technology, from catalytic supports, to doped thin films of high purity for specific applications. The metal doped silica systems are important for optical applications in the field of solid-state lasers, optical waveguides, fiber amplifiers, planar displaying devices, etc. [24]. Rare earth ions doped silica for optical applications has been studied by great number of authors in the last few decades [6]; conversely, the transition metal ions doped particles are not yet widely investigated. However, nanoparticles doped with rare earth or transition metal ions are perspective candidates for efficient phosphors in a new generation of light sources, e.g. in compact fluorescence lamps and in semiconductor-based white light emitting diodes [26].

The introduction of metals in the glass matrix by the sol-gel method has a strong influence on the optical visible absorption spectrum and on their photoluminescence properties. Coloring in these systems is due to the atomic transitions in the *d* orbitals of the incorporated metals and/or due to the formation of small metal or metal oxide particles. On the other hand, if the metal ions are finely dispersed on an inert substrate very efficient catalysators can be obtained [25].

Thus the synthesis of silica nanoparticles in acidic inverse microemulsion was carried out in the presence of either Co<sup>2+</sup> or Cu<sup>2+</sup> ions with the aim to get correspondingly doped nanoparticles. The acidic medium was chosen for the synthesis since it was efficient method, according to many authors, for the preparation of both silica coatings and doped materials. Villegas *et al.* [130] reported the synthesis of Cu coatings using TMOS and methyltriethoxysilane as SiO<sub>2</sub> precursors at different concentrations of several Cu(I) and Cu(II) salts with HCl as catalyst. De Sales *et al.* [132] synthesized both silica coatings and doped materials using Cu(NO<sub>3</sub>)<sub>2</sub>·3H<sub>2</sub>O at various TEOS/Cu molar ratios in EtOH/H<sub>2</sub>O/HNO<sub>3</sub> system, and the same Cu precursor and acid catalyst were used by Paulose *et al.* [133] for

the synthesis of Cu doped monoliths. Cu doped silica gels were synthesized by Duval *et al.* [134] in the TEOS/EtOH/H<sub>2</sub>O system with HCl and CuCl as catalyst and metal precursor, respectively. Yang *et al.* [135] reported the synthesis of Cu and Co doped SiO<sub>2</sub> xerogels in EtOH/H<sub>2</sub>O/TEOS/HCl system with CuCl<sub>2</sub>·2H<sub>2</sub>O and Co(CH<sub>3</sub>COO)<sub>2</sub>·4H<sub>2</sub>O as metal precursors. The same system was used by Lenzi *et al.* [136] for the synthesis of Co doped silica based materials with the CoCl<sub>2</sub>·6H<sub>2</sub>O precursor. However, at least to our knowledge, the synthesis of Cu and Co doped nanoparticles in acid-catalyzed inverse microemulsion has not been yet reported. Tagenaka *et al.* [137] reported the synthesis of silica supported Co catalysts in aqueous NH<sub>3</sub> inverse microemulsion where different synthesis procedure gave particles with diameters of 20-60 nm which precipitate from the reaction medium.

Therefore we preferred acid-catalyzed route in order to maintain particles in solution during the synthesis so to prevent the aggregation and to obtain much smaller particles. Since the synthesis of undoped nanoparticles in acidic medium has proven to give better product with HCl than HNO<sub>3</sub> as catalyst in both hydrolysis and condensation steps, the former was chosen also for the synthesis of doped nanoparticles. Consequently, the chloride salts were employed as metal source.

### 3.4.1 Characterization of Microemulsions

#### *<sup>1</sup>H and <sup>13</sup>C NMR*

The <sup>1</sup>H and <sup>13</sup>C NMR spectra of the acid-catalyzed inverse microemulsions containing Co<sup>2+</sup> and Cu<sup>2+</sup> have been investigated and compared to those registered in the absence of metals, that is in the “HCl 0.1 M microemulsion”.

The aromatic signals did not change significantly, nor did the tail signals, except the *t*-Bu protons which in these systems presented as singlet since the effect of water diminished because metal ions were hydrated by water molecules that used to hydrate the surfactant's head.



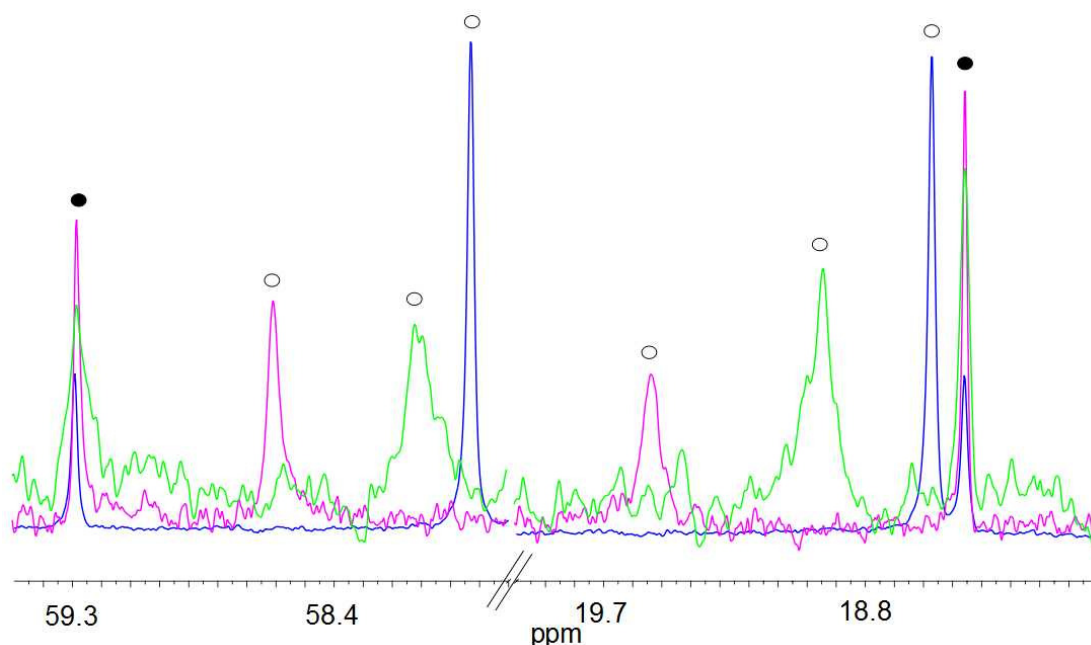
### 3.4.2 Characterization of Reaction Media

#### *<sup>1</sup>H and <sup>13</sup>C NMR*

The spectra of Igepal in the reaction medium did not vary during the synthesis of Cu<sup>2+</sup> and Co<sup>2+</sup> doped SiO<sub>2</sub> nanoparticles. The TEOS signals, being present prevalently in the oil, resonated at the same frequency as in the “HCl 0.1 M reaction medium” [103], however the reaction byproduct, EtOH, partitioned highly in micellar core, was affected by the presence of dopants.

In the <sup>1</sup>H spectrum of the Co<sup>2+</sup> doped system the EtOH methyl triplet shifted to 0.03 ppm higher frequency respect to “HCl 0.1 M reaction medium”, while methylene signals were buried under the signals of the polyethyleneoxide envelope and therefore unable to investigate. The shift of EtOH methyl protons in Cu<sup>2+</sup> doped system was not determined since we could not distinguish them from the very broad TEOS signals; however, in the spectrum registered 90 h after reaction beginning, i.e. after the complete consumption of TEOS, we did not observe EtOH signals which were probably buried under the signal of cyclohexane.

In the <sup>13</sup>C NMR spectrum both methyl and methylene EtOH signals shifted to higher frequencies respect to “HCl 0.1 M reaction medium”, as it can be seen from Figure 3.36, and the shifts were clear in both systems, although much higher for the Co<sup>2+</sup> doped system. The CH<sub>3</sub> carbon presented a shift of 0.97 ppm and CH<sub>2</sub> carbon of 0.69 ppm. In the Cu<sup>2+</sup> doped systems the shifts were 0.37 ppm for CH<sub>3</sub> and 0.19 ppm for CH<sub>2</sub> carbon.



**Figure 3.36** Region of the  $^{13}\text{C}$  NMR spectra of methyl (lower frequencies) and methylene (higher frequencies) signals of TEOS (●) and EtOH (○) registered 14 h after reaction beginning for the samples: “HCl 0.1 M reaction medium” (blue), “Cu doped reaction medium” (green) and “Co doped reaction medium” (purple).

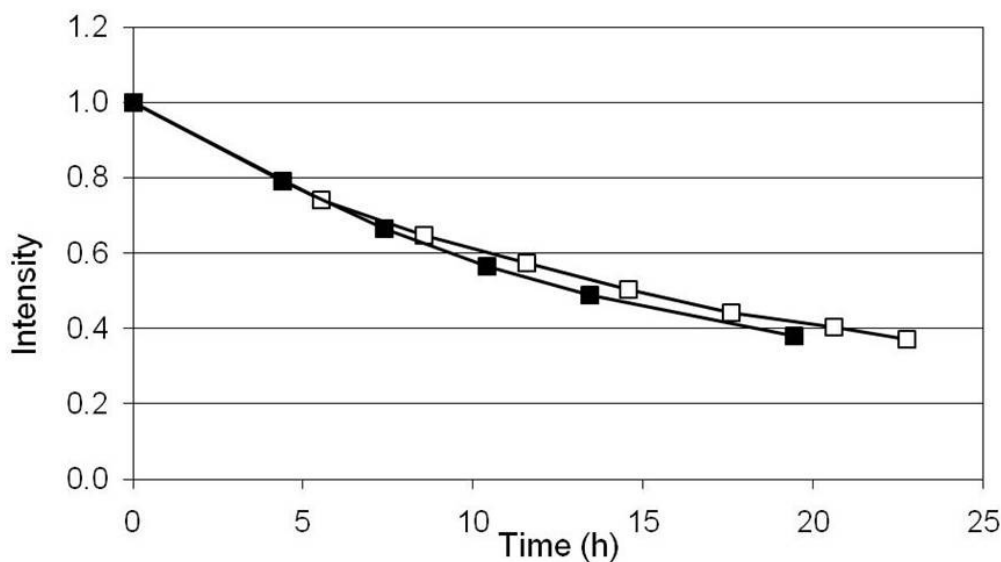
### 3.4.3 Hydrolysis

The  $^1\text{H}$  and  $^{13}\text{C}$  NMR spectra, registered every 3 hours during the period of about 20 hours, were used to follow hydrolysis advancement. The trend of TEOS methyl proton signal intensities versus time was fitted according to the well established first order kinetic equation (3.6) respect to TEOS concentration. The trend of TEOS methylene proton signals could not be determined as the signals were overlapped by the signals of polyoxyethylene envelope of Igepal head groups while the TEOS  $\text{CH}_3$  and  $\text{CH}_2$  carbons were in agreement with the proton data.



The kinetics constants were determined as an average of two independent measurements for both  $\text{Cu}^{2+}$  and  $\text{Co}^{2+}$  doped systems, and the data thus obtained showed that the hydrolysis rates were equal for both systems and fast ( $k= 0.05 \text{ h}^{-1}$ ) (Figure 3.37), yet much slower if compared to the rate observed in the undoped “HCl 0.1 M microemulsion” ( $k= 0.08 \text{ h}^{-1}$ ) [103]. This occurred because in the doped systems hydration of the ions diminishes the core water available for the hydrolysis reaction.

The trend of the EtOH methyl signal intensities could not be used as the support of the rate determination like in previous systems because the signals, if not overlapped, were too broad.

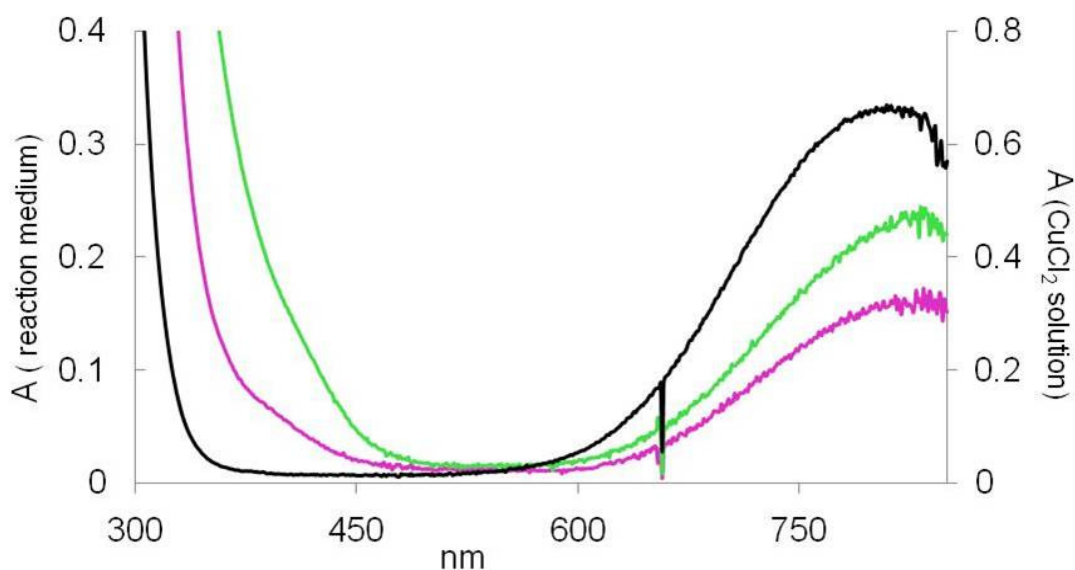


**Figure 3.37** Intensities vs. reaction time of the  $^1\text{H}$  TEOS methyl signals in the  $\text{CoCl}_2$  (□) and  $\text{CuCl}_2$  (■) doped systems.

### 3.4.4 UV-Vis Spectra

From the spectra recorded for the  $\text{Cu}^{2+}$  doped system at different time intervals a weak and broad absorption band with a peak around 800 nm was observed which clearly indicates the presence of the  $\text{Cu}^{2+}$  ions. It is well known that the diluted  $\text{Cu}^{2+}$  ions both in aqueous solutions and inside glass matrix exhibit a broad optical absorption band centered at about 780 nm, attributed to the transition between the d levels of Cu atoms in a ligand field due to a Jahn-Teller splitting [138-143].

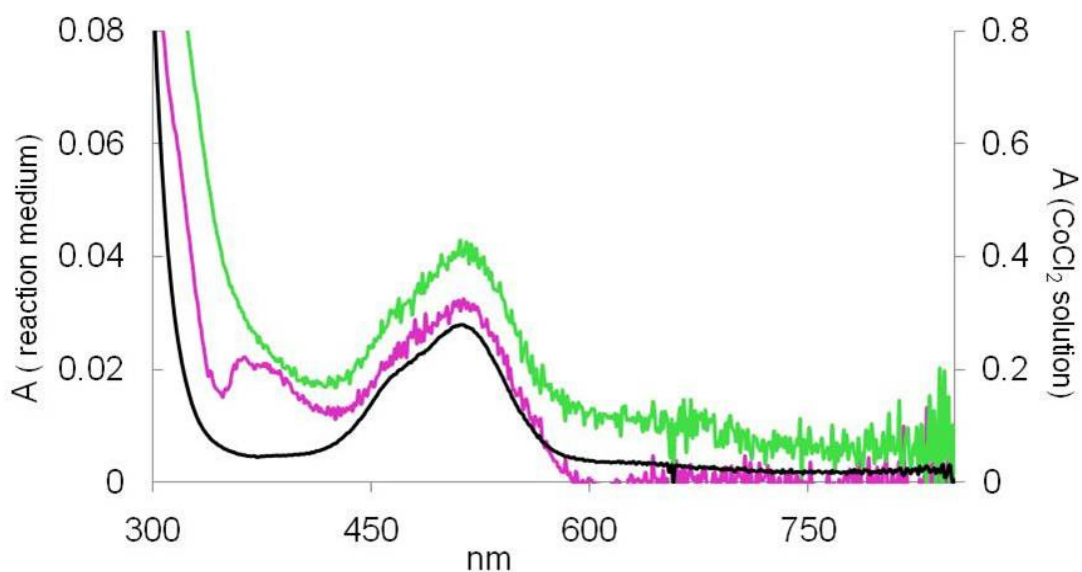
In Figure 3.38 the spectra registered at different times during the reaction are reported and compared to the solution containing  $\text{CuCl}_2$  0.05 M in HCl 0.01 M. The increase of absorbance intensity was observed in the  $\text{Cu}^{2+}$  doped system already 24 hours after the reaction beginning, and did not vary significantly at the later stage. The same behavior was reported during silica polymerization in the Cu-doped  $\text{SiO}_2$  coatings and powders employing  $\text{Cu}(\text{NO}_3)_2$  as the metal precursor [143]. Moreover, the increase of the intensity of the  $d-d$  transition with the increase of the metal concentration, accompanied by a broadening of the absorption band and by a shifting of the maximum, was observed in similar systems [132,144]. However, in our system the spectra were registered at early reaction times, i.e., during the hydrolysis step, so the band increase due to the polymerizing silica can be ruled out. Also, the metal concentration was constant and therefore unable to influence the band intensity. Hence we assigned the absorbance increase to the decreasing water content due to its consumption for TEOS hydrolysis and to apparent increase of  $\text{Cl}^-$  concentration where the change is consistent with the successive replacement of water ligands by chloride ligands, as already reported in literature for aqueous solution of  $\text{CuCl}_2$  [145-147]. The spectrum registered at a later stage of the reaction was close to the one obtained from Cu doped mesoporous silica nanospheres where copper is located at the internal surface, mainly as mononuclear oxide species very well dispersed [148].



**Figure 3.38** Absorption spectrum of the solution  $\text{CuCl}_2$  0.05 M in HCl 0.01 M (black) and of the  $\text{Cu}^{2+}$  doped system 2.75 h (purple) and 24 h (green) after the reaction beginning.

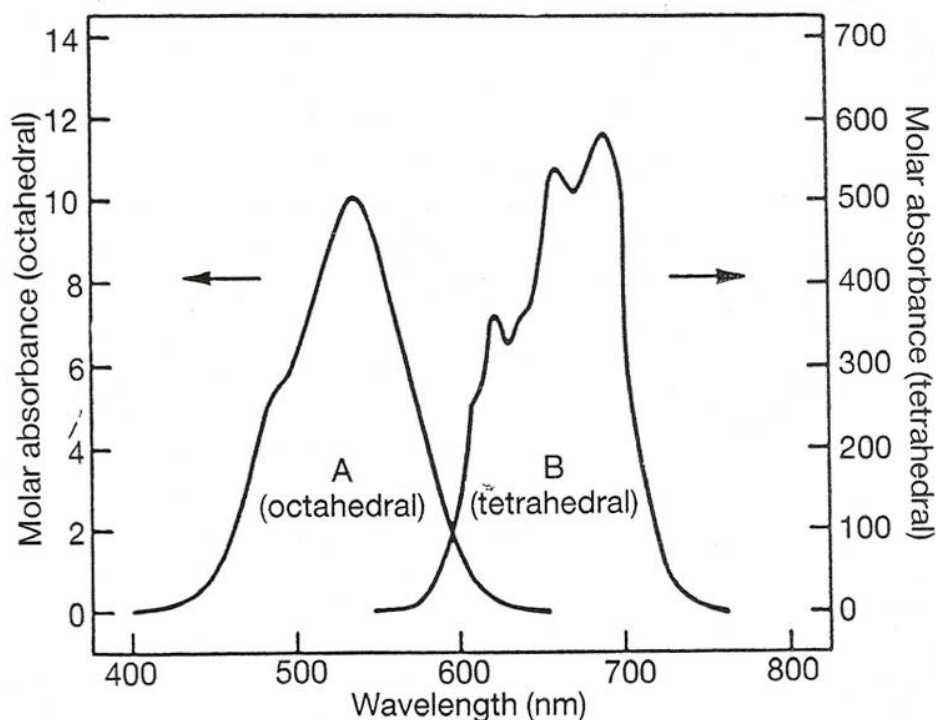
The absorption in the blue part of the spectrum, i.e. below 350 nm, shifted to longer wavelengths during the reaction. It was associated to a charge transfer band between the metal and the ligands of the glass matrix in the previous studies of Cu doped xerogels [133,146]. Unfortunately, this spectral region was affected by the strong absorption of the aromatic ring of the surfactant. Nevertheless, no changes were observed during the reaction in undoped systems.

From the spectra recorded for the  $\text{Co}^{2+}$  doped system with chloride as the counterion an absorption band centered at 510 nm was observed, with two distinct shoulders at about 460 nm and 630 nm, respectively (Figure 3.39). The  $\text{Co}^{2+}$  ions with nitrate as the counterion, either in aqueous solution or in the solid state, exhibit one main band at  $\sim 524$  nm and two well-defined shoulders at 456 and 625 nm [149]. These bands are assigned to d-d transitions of  $\text{Co}^{2+}$  coordinated by six O atoms by most authors [149-153].



**Figure 3.39** Absorption spectrum of the solution  $\text{CoCl}_2$  0.05 M in HCl 0.01 M (black) and of the  $\text{Co}^{2+}$  doped system 2.75 h (purple) and 24 h (green) after the reaction beginning.

The optical appearance of a glass containing  $\text{Co}^{2+}$  depends on the coordination sites where it is placed. Three bands in the visible range are characteristic for the glasses of a pink color that have  $\text{Co}^{2+}$  in an octahedral environment whereas a more intense absorption spectra with the bands shifted to longer wavelengths are characteristic for a light blue color glasses containing four-coordinated  $\text{Co}^{2+}$  [154]. Moreover the shape of the main band is much different for the two coordinations (Figure 3.40) [155] and the shape of the band observed in our system clearly indicates the presence of octahedral Co coordinated with six water molecules. However, the band at 630 nm might be also assigned, besides to d-d transitions, to the small amounts anhydrous salt containing Co in tetrahedral coordination,  $[\text{CoCl}_4]^{2-}$  [155].



**Figure 3.40** The visible spectra of A)  $[\text{Co}(\text{H}_2\text{O})_6]^{2+}$  and B)  $[\text{CoCl}_4]^{2-}$  [155].

From Figure 3.39, where the spectra registered at different times during the reaction are reported and compared to the solution containing  $\text{CoCl}_2$  0.05 M in  $\text{HCl}$  0.01 M, it was observed that the two shoulders are more evident in the absorbance band of the solution. Moreover, the increase of absorbance observed in the  $\text{Cu}^{2+}$  doped system was observed at the same reaction times for the  $\text{Co}^{2+}$  doped system, although was less pronounced. The band below 350 nm was attributed to charge transfer from 2p of an oxygen atom to 3d of a Co atom [137], and no shifts were observed during the reaction advancement, however it was the edge of the registered absorption.

### 3.4.5 Characterization of the Products

The  $\text{Co}^{2+}$  and  $\text{Cu}^{2+}$  doped  $\text{SiO}_2$  nanoparticles were isolated from the reaction medium where the colors of solutions were pink and blue-green, respectively while the final products were blue and yellow powder, respectively. Further characterization was accomplished by FTIR and Raman spectroscopy, and TEM.

#### *IR Spectra*

The IR spectra of doped and undoped nanoparticles did not differ significantly due to the low concentration of dopant ions in the doped  $\text{SiO}_2$  nanoparticles.

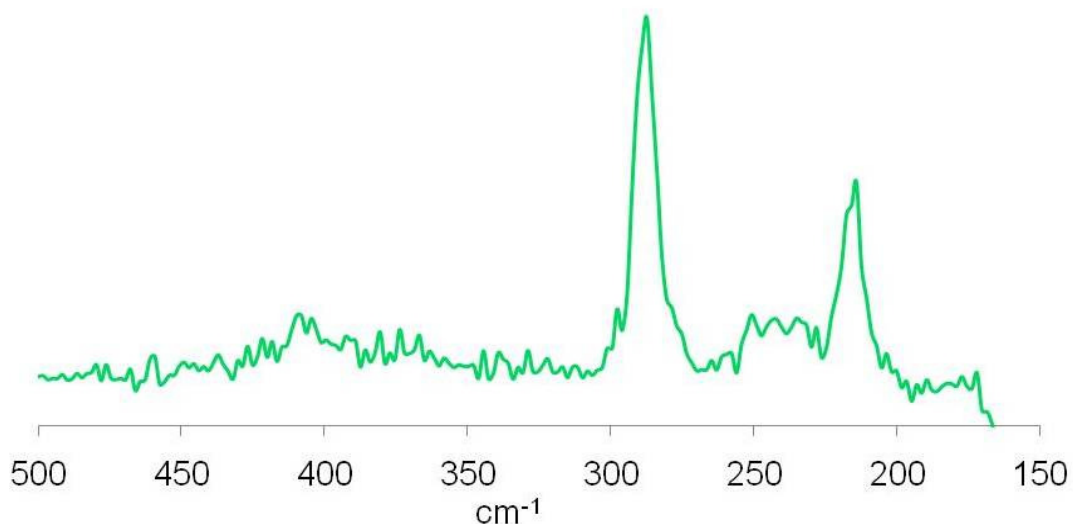
#### *Raman Spectra*

Doped nanoparticles were analyzed by Raman spectroscopy and compared to the chloride salts of the metal precursors used for the synthesis. The spectra of both  $\text{Co}^{2+}$  and  $\text{Cu}^{2+}$  doped systems were registered from 150 to 1800  $\text{cm}^{-1}$  with the near-infrared laser (785 nm diodes). Moreover, the  $\text{Co}^{2+}$  doped system was analyzed with HeNe laser (633 nm) in the range between 100 and 750  $\text{cm}^{-1}$  and the  $\text{Cu}^{2+}$  doped system with the  $\text{Ar}^+$  laser (514 nm) in the range between 150 and 1800  $\text{cm}^{-1}$ .

The spectra of  $\text{Cu}^{2+}$  doped system were not too useful since only the bands assignable to residual Igepal were observed after the excitation with 785 nm NIR laser, since it was removed only partially in order to provide steric stabilization of nanoparticles. The spectra recorded with 514 nm Argon laser showed no signals due to the baseline distortions.

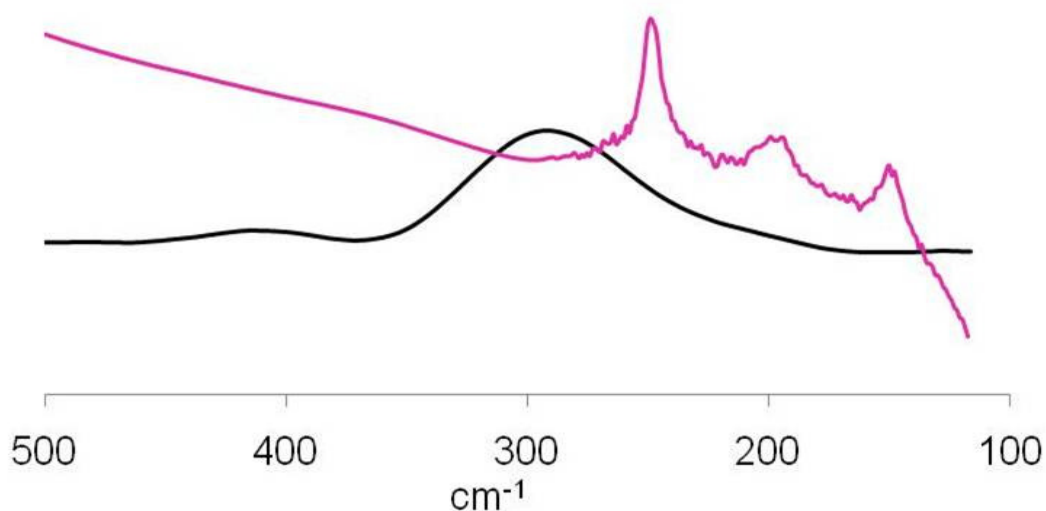
However, the  $\text{Ar}^+$  laser proved very efficient in the analysis of the sample  $\text{CuCl}_2 \cdot n\text{H}_2\text{O}$  dehydrated by heating in oven at 120 °C. The coexistence of anhydrous and hydrated salt was revealed. From Figure 3.41 it can be seen that the band at 287  $\text{cm}^{-1}$  dominates the spectrum and covers typically reported range for the Raman active  $\text{Cu-Cl}_{\text{eq(short)}}$  symmetric stretching vibrations of anhydrous  $\text{CuCl}_2$ . There is

another intense band at  $214\text{ cm}^{-1}$  and it was assigned to Raman active  $\text{Cu-Cl}_{\text{ax(long)}}$  symmetric stretching vibrations of  $\text{CuCl}_2 \cdot 2\text{H}_2\text{O}$  [156].



**Figure 3.41** Raman spectrum ( $500 - 150\text{ cm}^{-1}$ ) of  $\text{CuCl}_2$  salt.

The Figure 3.42 reports the spectra of the  $\text{Co}^{2+}$  doped sample together with the one of the pure  $\text{CoCl}_2$  analyzed with HeNe laser and it can be seen that at the low wavenumber region there are only bands of the vibrations involving  $\text{Co}^{2+}$ . Anhydrous  $\text{CoCl}_2$  is very sensitive to humidity, thus it initially presented three bands, at  $150$ ,  $200$  and  $250\text{ cm}^{-1}$ . Their intensity varied in time due to the hydration of the metal ions while the color was changing from light blue to violet intense. The band at  $250\text{ cm}^{-1}$  was the most intense and together with the band at  $150\text{ cm}^{-1}$  was assigned to anhydrous  $\text{CoCl}_2$ . The band at  $200\text{ cm}^{-1}$  was assigned to hydrated salt and it was the only band remaining over the time due to the formation of aqueous complex. In the  $\text{Co}^{2+}$  doped sample the band of the vibrations involving  $\text{Co}^{2+}$  broadened significantly and it appeared at  $286\text{ cm}^{-1}$ .

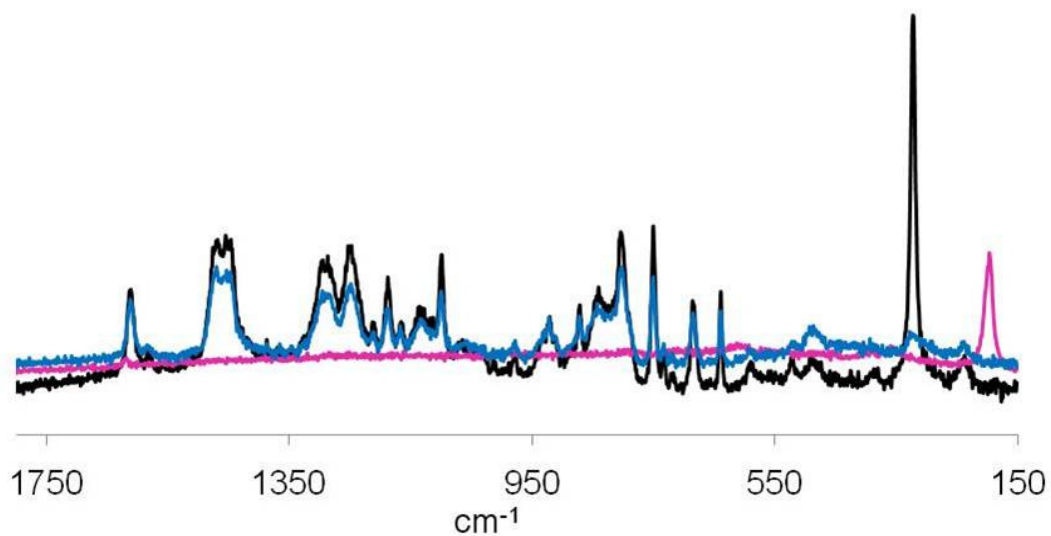


**Figure 3.42** Raman spectra (500 - 100 cm<sup>-1</sup>) of Co<sup>2+</sup> doped SiO<sub>2</sub> nanoparticles (black) and CoCl<sub>2</sub> salt (purple).

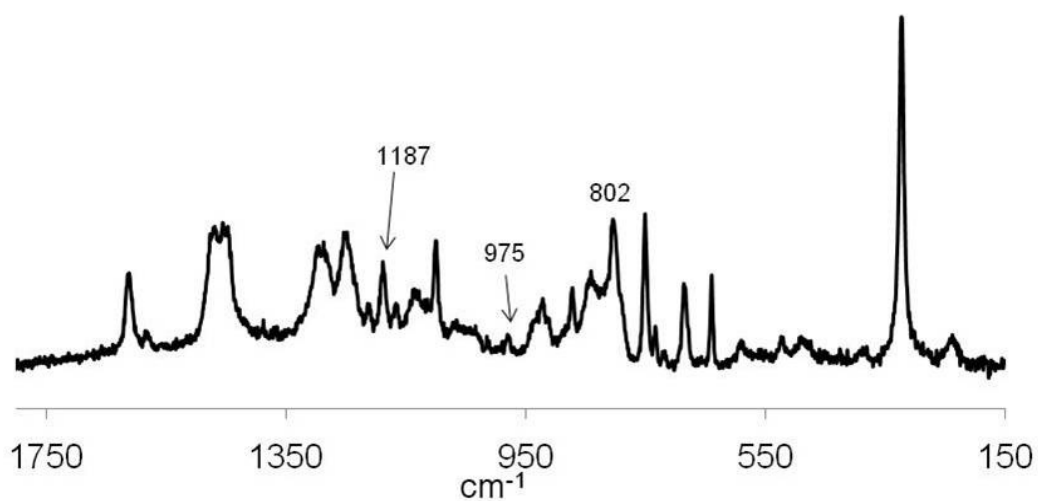
The spectra of Co<sup>2+</sup> doped sample were compared to the undoped silica and to the CoCl<sub>2</sub> salt, all recorded after the excitation at 785 nm with NIR laser. It is evident from Figure 3.43 the presence of bands of organic molecules which can be assigned to the residues of surfactant in both undoped and doped samples.

Silica attributable bands are in the range between 100 and 1100 cm<sup>-1</sup> [157] and because of the structural disorder of amorphous silica the interpretation of the experimental data is not straightforward. Unfortunately, the presence of Igepal hampers the observation and the assignment of the weak SiO<sub>2</sub> Raman signals. The typical SiO<sub>2</sub> Raman bands reported in literature at ~1185 cm<sup>-1</sup>, longitudinal Si-O-Si asymmetric stretching mode, at ~800 cm<sup>-1</sup>, Si-O-Si network symmetric bond stretching vibration, at 975 cm<sup>-1</sup>, stretching of terminal Si-OH groups, were observed (Figure 3.44) [23, 118]. The bands at ~1070 cm<sup>-1</sup>, transversal asymmetric Si-O-Si stretching, and the one at ~430 cm<sup>-1</sup>, Si-O-Si network bending, were not detected [23, 118].





**Figure 3.43** Raman spectra ( $1800 - 150 \text{ cm}^{-1}$ ) of  $\text{Co}^{2+}$  doped  $\text{SiO}_2$  nanoparticles (black), undoped  $\text{SiO}_2$  nanoparticles (blue) and  $\text{CoCl}_2 \cdot n\text{H}_2\text{O}$  salt (purple).

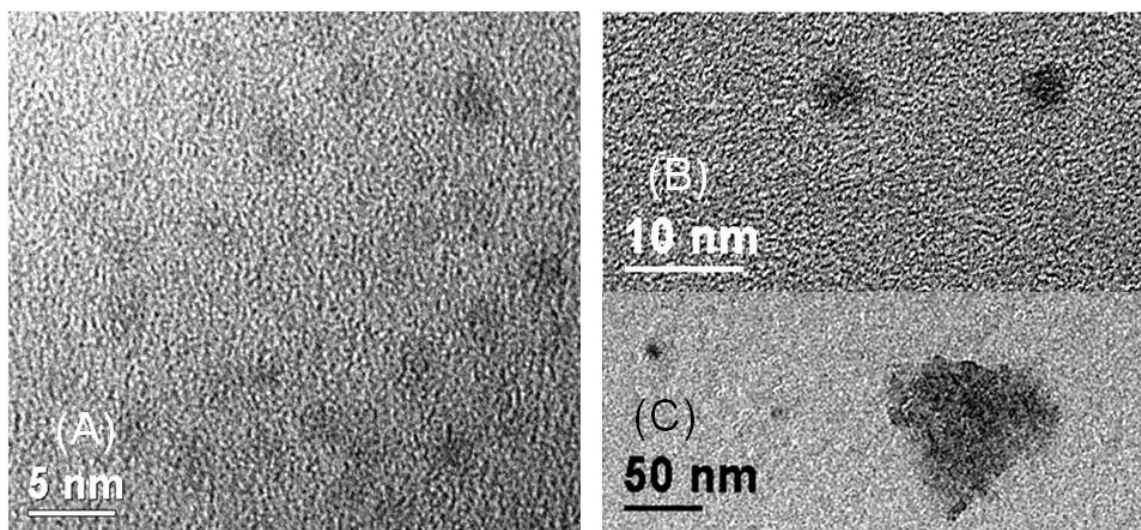


**Figure 3.44** Raman spectrum of  $\text{Co}^{2+}$  doped  $\text{SiO}_2$  nanoparticles. Numbers are indicating characteristic  $\text{SiO}_2$  bands.

After the excitation with 785 nm NIR laser the band which may be attributed to vibrations involving  $\text{Co}^{2+}$  in the doped sample appeared at  $320\text{ cm}^{-1}$  (Figure 3.43) while in the same sample after the excitation with 633 nm HeNe laser it was centered at  $286\text{ cm}^{-1}$  (Figure 3.42) and it was much broader. Since the band position differs from those reported previously for pure salts, both anhydrous and hydrated, it may be assigned to  $\text{Co}^{2+}$  embedded in the silica matrix. Further investigations are required to ascertain the localization of cobalt ion. Nevertheless, the presence of cobalt oxide can be ruled out since the signals  $\text{Co}_3\text{O}_4$  reported in literature ( $695\text{ (s)}$ ,  $528\text{ (w)}$ ,  $489\text{ (w)}$   $\text{cm}^{-1}$ ) were not detected [158].

### TEM Analysis

Size and morphology of the doped silica nanoparticles were measured using a transmission electron microscope (TEM). It was demonstrated that inverse micelles can be used to produce  $\text{Co}^{2+}$  and  $\text{Cu}^{2+}$  doped  $\text{SiO}_2$  nanoparticles with diameter of about 3 and 4 nm, respectively. Spherical particles smaller than the micellar size (Figure 3.45 A and B) and, in the case of  $\text{Cu}^{2+}$  doped system, larger, irregularly shaped aggregates with diameter up to  $1\text{ }\mu\text{m}$  (Figure 3.45 C) were observed.

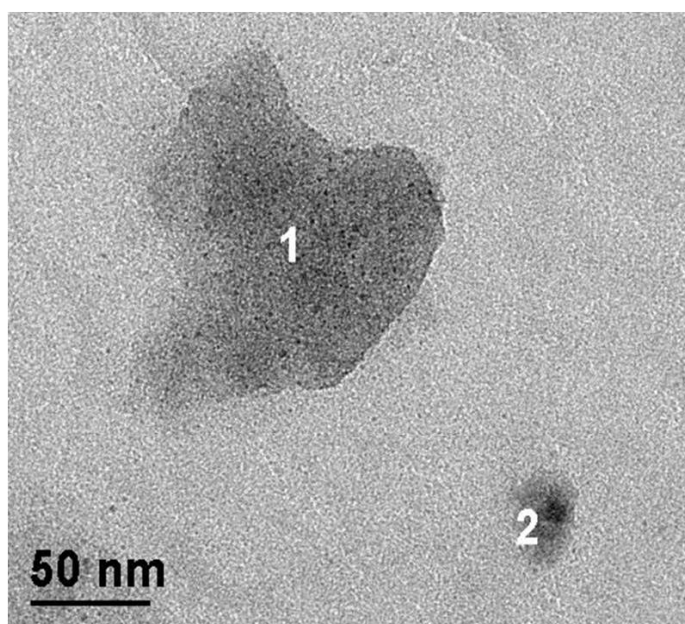


**Figure 3.45** TEM micrographs of solid silica isolated from the  $\text{Co}^{2+}$  doped system (A) and  $\text{Cu}^{2+}$  doped system (B and C).

Furthermore, the energy dispersive X-ray spectroscopy (EDS) was used in order to map the presence of Cu and Co atoms in the samples. The principle is to use a detector to analyze the energy distribution of electrons/photons emitted from the sample to determine the elemental composition. It is more accurate for heavy elements because heavier nuclei have a larger cross section to interact with the primary beam.

The TEM EDS spectra of Cu doped silica nanoparticles suggested that not all particles and aggregates contained copper, because Cu signals were weak, nonetheless significant. The small amount of copper in the particles is in line with the lack of signals attributable to vibrations involving Cu in the Raman spectra.

Lots of darker zones were observed in the TEM images of some larger particles and aggregates containing Cu (Figure 3.46). This dark spots can be assigned to Cu metal particles encapsulated in silica matrix [137], however they are too small to be further analyzed individually.



**Figure 3.46** TEM micrographs of solid silica isolated from the Cu<sup>2+</sup> doped system showing aggregate (1) and larger particle (2) containing Cu metal particles.

The TEM EDS spectra of Co doped silica nanoparticles indicated the contemporaneous presence of Si and Co signals in every particle thus it was concluded that cobalt was successfully doped in silica nanoparticles and it was dispersed uniformly.

## 4 CONCLUSIONS

- $^1\text{H}$  confirmed to be the most efficient nucleus to follow TEOS hydrolysis with the increasing signal of the byproduct EtOH exploitable as a control, except in the systems doped with paramagnetic metal ions.
- $^1\text{H}$  and  $^{13}\text{C}$  provided information at molecular detail on soluble species in order to obtain a thorough picture of the system.
- The diffusion coefficient measurements demonstrated that  $\text{NH}_3$  diffuses through the bulk oil and confirmed that the latter constitutes the preferential environment for EtOH, at an even higher degree in the acidic system.
- The PGSTE NMR allowed identifying the oligomeric species of commercial Igepal CA520 and determination of their partition degree between oil and inverse micelles.
- The  $^1\text{H}$ ,  $^{13}\text{C}$ , and PGSTE NMR results confirmed that the microemulsions do not undergo drastic changes during the reaction.
- The hydrolysis rate is first order with respect to TEOS concentration.
- The concentration of  $\text{H}_2\text{O}$  in the inner pools is very important and must be high enough to have sufficient core water available for hydrolysis reaction.
- An equal TEOS hydrolysis rate was obtained in both acidic and basic microemulsions whereas the condensation remained slower in the former.
- The condensation was accelerated by the presence of NaF.
- In base-catalyzed system the  $\text{SiO}_2$  nanoparticles outgrew the micellar size due to the depolymerization process and their size depended on  $R$ .
- In acidic medium the condensation was predominantly intramicellar and nanoparticles size was limited by the micellar size.

- The nonionic inverse microemulsion is a successful mean for limiting the growth of silica particles from sol-gel process under strong acid catalysis.
- Silica produced by acid catalysis had a more open, randomly branched structure whereas product from base-catalyzed systems had a higher density of cross-linking.
- The SiO<sub>2</sub> nanoparticles formed in acidic microemulsion gave photoluminescence. The relevant band was narrow, indicating monodispersity.
- The SiO<sub>2</sub> nanoparticles were obtained also in the presence of Cu<sup>2+</sup> and Co<sup>2+</sup> metal ions.
- Cobalt was successfully doped in silica nanoparticles while copper doping seemed less satisfactory.

The achievement of doped silica nanoparticles is of great importance in view of the wide palette of potential applications. The synthesis in confined system with acid-catalysis is an innovative way of production and the present results are encouraging starting point for further developments. Acid catalysis is compulsory because the transition metal ions precipitate as oxide in basic medium. Among the most important, up to date, applications of very small amorphous SiO<sub>2</sub> [159] and metal doped SiO<sub>2</sub> nanoparticles [160] is the chemical vapor deposition catalysis for the production of single walled nanotubes. Another important application of doped nanoparticles is as efficient phosphors in a new generation of light sources and in television displays [24,26].

## 5 BIBLIOGRAPHY

- [1] Feynman P.R. *Plenty of Room at the Bottom* **1959**.
- [2] Feldmann C., Goesmann H. *Angew. Chem. Int. Ed.* **2010**, *49*, 2–36.
- [3] Hench L.L., West J.K. *Chem. Rev.* **1990**, *90*, 33–72.
- [4] Ganguli A.K., Ganguly A., Vaidya S. *Chem. Soc. Rev.* **2010**, *39*, 474–485.
- [5] Burns A., Ow H., Wiesner U. *Chem. Soc. Rev.* **2006**, *35*, 1028–1042.
- [6] Ye Z., Tan M., Wang G., Yuan J. *J. Mater. Chem.* **2004**, *14*, 851–856.
- [7] Bringley J.F., Penner T.L., Wang R., Harder J.F., Harrison W.J., Buonemani L. *J. Colloid Interface Sci.* **2008**, *320*, 132–139.
- [8] Finnie S.K., Barlett J.R., Barbé C.J.A., Kong L. *Langmuir* **2007**, *23*, 3017–3024.
- [9] Barbé C.J.A., Bartlett J., Kong L., Finnie K., Lin H.Q., Larkin M., Calleja S., Bush A., Calleja G. *Adv. Mater.* **2004**, *16*, 1959–1966.
- [10] Luo D., Saltzman W.M. *Gene Ther.* **2006**, *13*, 585–586.
- [11] Colvin V. L., Schlamp M.C., Alivisatos A.P. *Nature* **1994**, *370*, 354–357.
- [12] Dabbousi B.O., Bawendi M.G., Onitsuka O., Rubner M.F. *Appl. Phys. Lett.* **1995**, *66*, 1316–1318.
- [13] Huynh W.U., Peng X., Alivisatos A.P. *Adv. Mater.* **1999**, *11*, 923–927.
- [14] Huynh W.U., Dittmer J.J., Alivisatos A.P. *Science* **2002**, *295*, 2425–2427.
- [15] Alberto G., Miletto I., Viscardi G., Caputo G., Latterini L., Coluccia S., Martra G.J. *Phys. Chem. C* **2009**, *113*, 21048–21053.
- [16] Jung J.H., Ono Y., Shinkai S. *Langmuir* **2000**, *16*, 1643–1649.
- [17] Gautier C., Lopez P.J., Hemadi M., Livage J., Coradin T. *Langmuir* **2006**, *22*, 9092–9095.

- [18] Yao N., Xiong G., Yeung K.L., Sheng S., He M., Yang W., Liu X., Bao X. *Langmuir* **2002**, *18*, 4111–4117.
- [19] Hu J.Q., Jiang Y., Meng X.M., Lee C.S., Lee S.T. *Chem. Phys. Lett.* **2003**, *367*, 339–347.
- [20] Shang N.G., Vetter U., Gerhards I., Hofsäss H., Ronning C., Seibt M. *Nanotechnology* **2006**, *17*, 3215–3218.
- [21] Dubois M., Cabane B. *Macromolecules* **1989**, *22*, 2526–2533.
- [22] Barbé C.J.A., Kong L., Finnie K.S., Calleja S., Hanna J.V., Drabarek E., Cassidy D.T., Blackford M.G. *J. Sol-Gel Sci. Technol.* **2008**, *46*, 393–409.
- [23] Brinker, C J., Scherrer G.W. *Sol-Gel Science. The Physics and Chemistry of Sol-Gel Processing*, Academic Press, Boston, USA, **1990**, Chapter III.
- [24] Green W.H., Le K.P., Grey J., Au T.T., Sailor M.J. *Science* **1997**, *276*, 1826–1828.
- [25] Martyanov I.N., Uma S., Rodrigues S., Klabunde K.J. *Langmuir* **2005**, *21*, 2273–2280.
- [26] Godlewski M., Yatsunencko S., Nadolska A., Opalińska A., Łojkowski W., Drozdowicz-Tomsia K., Goldys E.M. *Opt. Mater.* **2009**, *31*, 490–495.
- [27] Ebelmen, M. *Ann. Chim. Phys.* **1846**, *16*, 129–166.
- [28] Geffcken W., Berger E. *German Patent 736,411*, May, **1939**.
- [29] Flory P.J. *Principles of Polymer Chemistry*, Cornell University Press, Ithaca, NY, USA, **1953**.
- [30] Iler R.K. *The Chemistry of Silica*, Wiley, New York, USA, **1979**.
- [31] Stöber W., Fink A., Bohn E. *J. Colloid Interface Sci.* **1968**, *26*, 62–69.
- [32] Green D.L., Jayasundara S., Lam Y.-F., Harris M.T. *J. Non-Cryst. Solids* **2003**, *315*, 166–179.
- [33] Green D.L., Lin J.S., Lam Y.-F., Hu M.Z.-C., Schaefer D.W., Harris M.T. *J. Colloid Interface Sci.* **2003**, *266*, 346–358.



- [34] Matsoukas T., Gulari E. *J. Colloid Interface Sci.* **1988**, *124*, 252–261.
- [35] Matsoukas T., Gulari E. *J. Colloid Interface Sci.* **1989**, *132*, 13–21.
- [36] Bogush G.H., Zukoski C.F. *J. Colloid Interface Sci.* **1991**, *142*, 1–18.
- [37] Bogush G.H., Zukoski C.F. *J. Colloid Interface Sci.* **1991**, *142*, 19–34.
- [38] Harris M.T., Brunson R.R., Byers C.H. *J. Non-Cryst. Solids* **1990**, *121*, 397–403.
- [39] van Blaaderen A., van Geest J., Vrij A. *J. Colloid Interface Sci.* **1992**, *154*, 481–501.
- [40] Lee K., Look J.-L., Harris M.T., McCormick A.V. *J. Colloid Interface Sci.* **1997**, *194*, 78–88.
- [41] Corriu R.J.P., LeClerq D., Vioux A., Pauthe M., Phalippou J. *Ultrastructure Processing of Advanced Ceramics*, Wiley, New York, USA, **1988**.
- [42] Rabinovich E., Wood D. *Mater. Res. Soc. Symp. Proc.* **1996**, *73*, 251–259.
- [43] Lide D.R. *CRC Handbook of Chemistry and Physics*, CRC Press, Boca Raton, FL, USA, **1994**, p. 8–43.
- [44] Bernardis T.N.M., van Bommel M.J., Jansen J.A.J. *J. Sol-Gel Sci. Technol.* **1998**, *13*, 749–752.
- [45] Griffin W.C. *J. Soc. Cosmet. Chem.* **1949**, *1*, 311–326.
- [46] Huibers P.D.T., Shah D.O. *Langmuir* **1997**, *13*, 5762–5765.
- [47] Hamley I.W. *Introduction to Soft Matter*, Wiley, UK, **2000**.
- [48] Hoar T.P., Schulman J.H. *Nature* **1943**, *152*, 102–103.
- [49] Langevin D. *Acc. Chem. Res.* **1988**, *21*, 255–260.
- [50] Winsor P.A. *Solvent Properties of Amphiphilic Compounds*, Butterworth, UK, **1954**.
- [51] Nagy J.B., Derouane E.G., Gourgue A., Lufimpadio N., Ravet I., Verfaillie J.P. *Surfactants in Solution*, Plenum Press, New York, USA, **1989**.
- [52] Monnoyer P., Fonseca A., Nagy J.B. *Colloids Surf., A.* **1995**, *100*, 233–243.

- [53] Chang C.-L., Fogler H.S. *AIChE J.* **1996**, *42*, 3153–3163.
- [54] Chang C.-L., Fogler H.S. *Langmuir* **1997**, *13*, 3295–3307.
- [55] Jin Y., Lohstreter S., Pierce D.T., Parisien J., Wu M., Hall C.III, Zhao J.X. *Chem. Mater.* **2008**, *20*, 4411–4419.
- [56] Pileni M.P. *Langmuir* **1997**, *13*, 3266–3276.
- [57] Arriagada F.J., Osseo-Asare K. *Colloids Surf.* **1990**, *50*, 321–339.
- [58] Arriagada F.J., Osseo-Asare K. *Colloids Surf., A* **1999**, *154*, 311–326.
- [59] Arriagada F.J., Osseo-Asare K. *J. Colloid Interface Sci.* **1999**, *211*, 210–220.
- [60] Thiele B., Günther K., Schwuger M.J. *Chem. Rev.* **1997**, *97*, 3247–3272.
- [61] Lee M.S., Park S.S., Lee G.-D., Ju C.-S., Hong S.-S. *Catal. Today* **2005**, *101*, 283–290.
- [62] Flory P.J. *J. Am. Chem. Soc.* **1940**, *62*, 1561–1565.
- [63] Eastoe J., Martin H.J., Hudson L. *Adv. Colloid Interface Sci.* **2006**, *128–130*, 5–15.
- [64] Fleischer G., Grätz K., Kärger J., Meyer H.W., Quitzsch K. *J. Colloid Interface Sci.* **1997**, *190*, 9–16.
- [65] Grätz K., Helmstedt M., Meyer H.W., Quitzsch K. *Colloid Polym. Sci.* **1998**, *276*, 131–137.
- [66] Kahweit M., Strey R., Busse G. *J. Phys. Chem.* **1990**, *94*, 3881–3894.
- [67] Kabalnov A., Olsson U., Wennerstrom H. *J. Phys. Chem.* **1995**, *99*, 6220–6230.
- [68] Karmakar B., De G., Ganguli D. *J. Non-Cryst. Solids* **2000**, *272*, 119–126.
- [69] De, G.; Karmakar, B.; Ganguli, D. *J. Mater. Chem.* **2000**, *10*, 2289–2293.
- [70] Liu J., Jiang X., Ashley C., Brinker C.J. *J. Am. Chem. Soc.* **2009**, *131*, 7567–7569.
- [71] Gan L. M., Zhang K., Chew C.H. *Colloids Surf. A* **1996**, *110*, 199–206.
- [72] Wang Z., Ma G., Liu X.Y. *J. Phys. Chem. B* **2009**, *113*, 16393–16399.

- [73] Furó I. *J. Mol. Liq.* **2005**, *117*, 117–137.
- [74] Stejskal E.O., Tanner J.E. *J. Chem. Phys.* **1965**, *42*, 288–292.
- [75] Antalek, B. *Concepts in Magnetic Resonance* **2002**, *4*, 225–258.
- [76] Burl M., Young I. R. *Encyclopedia of Nuclear Magnetic Resonance*, Vol. 3, Wiley, New York, **1996**, p. 1841.
- [77] Pelta M.D., Barjat H., Morris G.A., Davis A.L., Hammond S.J., *Magn. Reson Chem.* **1998**, *36*, 706–714.
- [78] Jerschow A., Müller N., *J. Magn. Reson.* **1997**, *125*, 372–375.
- [79] *NMR Spectroscopy, User Guide for Varian NMR Systems with VnmrJ Software* Pub. No. 01-999343-00, Rev. A 0607.
- [80] Morris G. A., Freeman R. *J. Am. Chem. Soc.* **1979**, *101*, 760–762.
- [81] Doddrell D. M., Pegg D.T., Brooks W., Bendall M.R. *J. Am. Chem. Soc.* **1981**, *103*, 727–728.
- [82] Winter R., Chan J.-B., Frattini R., Jonas J. *J. Non-Cryst. Solids* **1988**, *105*, 214–222.
- [83] Morris K. F., Johnson C.S. Jr *J. Am. Chem. Soc.* **1993**, *115*, 4291–4299.
- [84] M. Nilsson, *J. Magn. Reson.* **2009**, *200*, 296–302.
- [85] Riello P., Mattiazzi M., Pedersen J. S., Benedetti A. *Langmuir* **2008**, *24*, 5225–5228.
- [86] Podo F., Ray A., Nemethy G. *J. Am. Chem. Soc.* **1973**, *95*, 6164–6171.
- [87] Hoffmann M.M., Bennett M.E., Fox J.D., Wyman D.P. *J. Colloid Interface Sci.* **2005**, *287*, 712–716.
- [88] Yuan H., Miao X., Zhao S., Shen L., Yu J., Du Y. *Magn. Reson. Chem.* **2001**, *39*, 33–37.
- [89] Siegel M.M., Tsao R., Oppenheimer S., Chang T.T. *Anal. Chem.* **1990**, *62*, 322–327.

- [90] Breen J., van Duijn D., de Bleijser J., Leyte J.C. *Ber. Bunsen Ges.* **1986**, *90*, 1112–1122.
- [91] Hey M.J., Ilett S.M., Davidson G. *J. Chem. Soc., Faraday Trans.* **1995**, *91*, 3897–3900.
- [92] Karlström G. *J. Phys. Chem.* **1985**, *89*, 4962–4964.
- [93] Goutev N., Nickolov Z.S., Georgiev G., Matsuura H. *J. Chem. Soc., Faraday Trans.* **1997**, *93*, 3167–3171.
- [94] Connor T.M., McLauchlan K.A. *J. Phys. Chem.* **1965**, *69*, 1888–1893.
- [95] Derkaoui N., Said S., Grohens Y., Olier R., Privat M. *J. Colloid Interface Sci.* **2007**, *305*, 330–338.
- [96] Yuan H.-Z., Cheng G.-Z., Zhao S., Miao X.-J., Yu J.-Y., Shen, L.-F., Du Y.-R. *Langmuir* **2000**, *16*, 3030–3035.
- [97] Lindman B., Stilbs P. *Microemulsions “Structure and Dynamics”*; CRC Press: Boca Raton, FL, USA, **1987**.
- [98] Walderhaug H., Johannessen E. *J. Solution Chem.* **2006**, *35*, 979–989.
- [99] Ng L.V., McCormick S.V. *J. Phys. Chem.* **1996**, *100*, 12517–12531.
- [100] Asaro F., Benedetti A., Savko N., Pellizer G. *Langmuir* **2009**, *25*, 3224–3231.
- [101] Aelion R., Loebel A., Eirich F. *J. Am. Chem. Soc.* **1950**, *72*, 5705–5712.
- [102] Asaro F., Savko N. *Magn. Reson. Chem.* DOI 10.1002/mrc.2732.
- [103] Asaro F., Benedetti A., Freris I., Riello P., Savko N. *Langmuir* **2010**, *26*, 12917–12925.
- [104] Evans R., Haiber S., Nilsson M., Morris G.A. *Anal. Chem.* **2009**, *81*, 4548–4550.
- [105] Zielinski M.E., Morris K.F. *Magn. Reson. Chem.* **2009**, *47*, 53–56.
- [106] Tormena C.F., Evans R., Haiber S., Nilsson M., Morris G.A. *Magn. Reson. Chem.* **2010**, *48*, 550–553.

- [107] Pages G., Delaurent C., Caldarelli S. *Angew. Chem., Int. Ed.* **2006**, *45*, 5950–5953.
- [108] Lemyre J.-L., Rirtcey A.M. *Langmuir* **2010**, *26*, 6250–6255.
- [109] Lemyre J.-L., Lamarre S., Beaupré A., Rirtcey A.M. *Langmuir* **2010**, *26*, 10524–10531.
- [110] Schrier M.Y., Bullock O.A., Schrier E.E. *J. Phys. Chem.* **1980**, *84*, 350–354.
- [111] Salager J.-L., Marquez N., Graciaa A., Lachaise J. *Langmuir* **2000**, *16*, 5534–5539.
- [112] Coltrain B.K., Melpoder S.M., Salva J.M. *Proceedings of the IVth International Conference on Ultrastructure Processing of Ceramics, Glasses, and Composites* Feb 19-24 **1989**, Tucson, AZ, USA.
- [113] Leontidis E. *Curr. Opin. Colloid Interface Sci.* **2002**, *7*, 81–91.
- [114] Oh S.H., Ryoo R., Jhon M.S. *Macromolecules* **1990**, *23*, 1671–1675.
- [115] Zhang Y., Furyk S., Bergbreiter D.E., Cremer P.S. *J. Am. Chem. Soc.* **2005**, *127*, 14505–14510.
- [116] Zhao D., Huo Q., Feng J., Chmelka B.F., Stucky G.D. *J. Am. Chem. Soc.* **1998**, *120*, 6024–6036.
- [117] Muroya M. *Colloids Surf., A* **1999**, *157*, 147–155.
- [118] Bertoluzza A., Fagnano C., Morelli M.A. *J. Non-Cryst. Solids* **1982**, *48*, 117–128.
- [119] Martínez J.R., Ruiz F., Vorobiev Y.V., Pérez-Robles F., González- Hernández J. *J. Chem. Phys.* **1998**, *109*, 7511–7514.
- [120] Monsivais-Gámez E., Ruiz F., Martínez J.R. *J. Sol-Gel Sci. Technol.* **2007**, *43*, 65–72.
- [121] Vaccaro L., Cannas M., Boscaino R. *J. Luminescence* **2008**, *128*, 1132–1136.
- [122] Vaccaro L., Cannas M., Radzig V. *J. Non-Cryst. Solids* **2009**, *355*, 1020–1023.

- [123] Chizhik A.M., Chizhik A.I., Gutbrod R., Meixner A.J., Schmidt T., Sommerfeld J., Huisken F. *Nano Letters* **2009**, *9*, 3239-3244.
- [124] Cannas M., Vaccaro L., Boizot B. *J. Non-Cryst. Solids* **2006**, *352*, 203–208.
- [125] Skuja L., Tanimura K., Itoh N. *J. Appl. Phys.* **1996**, *80*, 3518–3525.
- [126] Skuja L. *J. Non-Cryst. Solids* **1994**, *179*, 51–69.
- [127] Skuja L., Suzuki T., Tanimura K. *Phys. Rev. B* **1995**, *52*, 15208–15216.
- [128] Sakurai Y. *J. Appl. Phys.* **2000**, *87*, 755–759.
- [129] Musso F., Ugliengo P., Solans-Monfort X., Sodupe M. *J. Phys. Chem. C* **2010**, *114*, 16430–16438.
- [130] Villegas M.A., García M.A., Lopis J., Fernández J.M.N. *J. Sol-Gel Sci. Technol.* **1998**, *11*, 251–265.
- [131] Zhang K., Gan L.M., Chew C.H., Gan L.H. *Mater. Chem. Phys.* **1997**, *47*, 164–170.
- [132] de Sales N.F., Costa V.C., Vasconcelos W.L. *Mater. Sci. Eng. A* **2005**, *408*, 121–124.
- [133] Paulose P.I., Jose G., Thomas V., Jose G., Unnikrishnan N.V., Warriar M.K.R. *Bull. Mater. Sci.* **2002**, *25*, 69–74.
- [134] Duval E., Bovier C., Roux H., Serughetti J., Tuel A., Wicker G. *J. Non-Cryst. Solids* **1995**, *189*, 101–106.
- [135] Yang P., Kai Lü M., Feng Song C., Xu D., Rong Yuan D. *Phys. Stat. Sol. B* **2002**, *231*, 106–111.
- [136] Lenzi G.G., Lenzi M.K., Baesso M.L., Bento A.C., Jorge L.M.M., Santos O.A.A. *J. Non-Crystal. Solids* **2008**, *354*, 4811–4815.
- [137] Takenaka S., Orita Y., Matsune H., Tanabe E., Kishida M. *J. Phys. Chem. C* **2007**, *111*, 7748–7756.
- [138] Orgaz F., Rawson H. *J. Non-Crystal. Solids* **1986**, *82*, 378–390.

- [139] Schaläfer H.L., Glieman G. *Basic Principles of Ligand Field Theory*, Wiley, New York, **1969**, Chap. 3, 321–386.
- [140] Abrita T., Cella N., Vargas H. *Chem. Phys. Lett.* **1989**, *161*, 12–15.
- [141] Nogami M., Abe Y., Nakamura A. *J. Mater. Res.* **1995**, *10*, 2648–2652.
- [142] Paul A. *Chemistry of Glasses 2*, Chapman and Hall, London, **1990**, p. 315.
- [143] Pérez-Robles J.F., Garcíá-Rodríguez F.J., Yáñez-Limón J.M., Espinoza-Beltrán F.J., Vorobiev Y.V., González-Hernández J. *J. Phys. Chem. Solids* **1999**, *60*, 1729–1736.
- [144] Leofanti G., Padovan M., Garilli M., Carmello D., Zecchina A. *Journal of Catalysis* **2000**, *189*, 91–104.
- [145] Brugger J., McPhail D.C., Black J., Spiccia L. *Geochim. Cosmochim. Acta* **2001**, *65*, 2691–2708.
- [146] Khan M.A., Schwing-Weill M.J. *Inorg. Chem.* **1976**, *15*, 2202–2205.
- [147] Voigt W., Hettrich K., Zeng D. *Thermodynamic Properties of Complex Fluid Mixtures* **2004**, 241–267.
- [148] Derrien G., Charnay C., Zajac J., Jones D.J., Rozière J. *Chem. Commun.* **2008**, *27*, 3118–3120.
- [149] Vakros J., Bourikas K., Perlepes S., Kordulis C., Lycourghiotis A. *Langmuir* **2004**, *20*, 10542-10550.
- [150] Nicholls D. *Complexes and First-Row Transition Elements*, MacMillan Press Ltd., London, U.K., **1974**.
- [151] Lever A.B.P. *Inorganic Electronic Spectroscopy*, 2nd ed., Elsevier, Amsterdam, The Netherlands, **1984**.
- [152] Sutton D. *Electronic Spectra of Transition Metal Complexes*; McGraw-Hill, London, New York, **1968**.
- [153] Kettle S.F.A. *Physical Inorganic Chemistry-A Coordination Chemistry Approach*, Oxford University Press, Oxford, U.K., **1996**.

- [154] Ramos-Mendoza A., Tototzintle-Huitle H., Mendoza-Galván A., González-Hernández J., Chao B.S. *J. Vac. Sci. Technol. A* **2001**, *19*, 1600–1605.
- [155] Cotton F.A., Goodgame D.M.L., Goodgame M. *J. Am. Chem. Soc.* **1961**, *83*, 4690–4699.
- [156] Stepakova L.V., Skripkin M.Y., Chernykh L.V., Starova G.L., Hajba L., Mink J., Sandström M. *J. Raman Spectrosc.*, **2008**, *39*, 16–31.
- [157] Murray C.A., Greytak T.J. *Phys. Rev. B* **1979**, *20*, 3368–3387.
- [158] Jeziorowski H., Knözinger H., Grange P., Gajardo P. *J. Phys. Chem.* **1980**, *84*, 1825–1829.
- [159] Liu B., Tang D.M., Sun C., Liu C., Ren W., Li F., Yu W.J., Yin L.C., Zhang L., Jiang C., Cheng H.M. *J. Am. Chem. Soc.* **2011**, *133*, 197–199.
- [160] Hofmann S., Sharma R., Ducati C., Du G., Mattevi C., Cepek C., Cantoro M., Pisana S., Parvez A., Cervantes-Sodi F., Ferrari A.C., Dunin-Borkowski R., Lizzit S., Petaccia L., Goldoni A., Robertson J. *Nano Lett.* **2007**, *7*, 602–608.



# ACKNOWLEDGMENTS

First and foremost I wish to thank my supervisor Dr. Fioretta Asaro.

I appreciate all her contributions of time, ideas, and funding to make my Ph.D. experience productive and stimulating. This thesis would not have been possible without her leadership, support, attention to detail, and hard work.

I am grateful to Professor Giorgio Pellizer as he provided sound advice, good teaching and lots of good ideas.

It is a pleasure to thank Professor Enzo Alessio, Director of the Ph.D. School in Chemical and Pharmaceutical Sciences and Technologies of the University of Trieste for his guidance and enormous effort.

My thanks go to the members of Department of Chemistry of the University of Trieste who have contributed immensely to my personal and professional time.

They have been a true source of friendships as well as good advice and collaboration.

The research presented was carried out in collaboration with group of Professor Alvise Benedetti from INSTM and Ca' Foscari University of Venice.

I want to thank them for providing SAXS, TEM, TGA and DSC analysis and relevant discussions.

I would like to thank to Professor Valter Sergo and Dr. Alois Bonifacio from University of Trieste for the Raman measurements.

Last but not least, I wish to thank my family who have always supported me and believed in me, Darko for enjoying life together with me, and my friends for their true friendship. Completing a PhD is truly a marathon event, and I would not have been able to complete this journey without you.

Nina Šavko